Chair of Materials Physics

Doctoral Thesis

Structural and Mechanical Property Investigation of Metallic Glasses

Dipl.-Ing. Amir Rezvan

August 2023

MONTANUNIVERSITÄT LEOBEN
www.unileoben.ac.at

AFFIDAVIT

I declare on oath that I wrote this thesis independently, did not use other than the specified sources and aids, and did not otherwise use any unauthorized aids.

I declare that I have read, understood, and complied with the guidelines of the senate of the Montanuniversität Leoben for "Good Scientific Practice".

Furthermore, I declare that the electronic and printed version of the submitted thesis are identical, both, formally and with regard to content.

Date 01.08.2023

Signature Author
Amir Rezvan

Acknowledgements

Foremost, I would like to express my deepest gratitude and regards to my supervisor Professor Jürgen Eckert, Head of the Erich-Schmid-Institute of Materials Science of the Austrian Academy of Sciences and the Chair of Materials Physics of Montanuniversität Leoben, for giving me the opportunity to write my doctoral thesis at his group and for his strong support during the whole course of this study.

I would like to express my sincerest appreciation and regards to Dr. Baran Sarac, who helped me throughout my thesis.

I am also highly obliged to Dr. Viktor Soprunyuk, Dr. Elham Sharifikolouei, and all the other colleagues.

Special thanks to my family and friends for their love and support.

Abstract

The structure-mechanical property relationships of bulk metallic glass (BMG) systems are assessed at various testing domains. By applying a series of materials science concepts, extensive characterization is achieved conveying information about thermo-mechanically driven structural relaxation and crystallization behavior in specific groups of advanced glassy multicomponent systems. In detail, the following studies of selected groups of alloys were carried out:

- The influence of severe plastic deformation (SPD) prompted by high-pressure torsion (HPT) and isothermal heat treatment (HT) below the glass transition on the structure-property relationships of $Cu_{46}Zr_{46}Al_8$ BMG is investigated separately and alternately in reference to the as-cast state. Controlled crystallization is attained through HT, and HPT was employed afterwards to disperse crystals throughout the glassy matrix. The dispersion of the second phase enhances the thermomechanical stability around the super cooled liquid region.

- The viscoelastic behavior of four different bulk metallic glass BMG systems, i.e., $Cu_{46}Zr_{46}Al_8$, $Cu_{44}Zr_{44}Al_8Co_4$, $Cu_{44}Zr_{44}Al_8Hf_4$, and $Cu_{44}Zr_{44}Al_8Co_2Hf_2$, was investigated concerning its deformation-mode dependence via dynamic mechanical analysis (DMA) in 3-point bending (TPB), tension, and torsion modes. Crystallization decreases the viscoelastic contribution, whereas plastic deformation leads to an increase in atomic mobility. Compared to $Cu_{46}Zr_{46}Al_8$, 4 at. % Co addition in the $Cu_{46-x/2}Zr_{46-x/2}Al_8Co_x$ amorphous alloy leads to a glass showing relatively higher thermomechanical stability around its glass transition.

- $Ti_{40}Zr_{10}Cu_{36}Pd_{14}$ BMG is envisioned as an oral implant material and its performance was evaluated in comparison with the gold standard Ti–6Al–4V implant material. DMA showed that these materials can be thermomechanically shaped into implants. High-resolution transmission microscopy and X-ray photoelectron spectroscopy revealed the formation of a 15 nm thin copper oxide layer on $Ti_{40}Zr_{10}Cu_{36}Pd_{14}$ BMG. Unlike titanium oxide formed on Ti–6Al–4V, copper oxide is hydrophobic, and its formation reduces the surface wettability. A lower surface colonization of bacteria is confirmed by field emission scanning electron microscopy and fluorescent images.

- The prospects of $Ti_{40}Zr_{10}Cu_{36}Pd_{14}$ BMG as oral implant material are advanced in the aspects of processing and structure-dependent mechanical performance. Insights into possible processing routes are provided, where high-temperature compression molding via an optimized process was adopted to both evaluate the thermoplastic net-shaping kinetics and tune the specific properties of the alloy. Processed BMGs and BMG composites of the same composition exhibit improved thermomechanical stability, from which high strength retention at temperatures, compared to the cast glass, by above 100 K higher is registered via dynamic mechanical analysis.

Kurzfassung

Die strukturmechanischen Eigenschaftsbeziehungen von metallischen Massivgläsern (engl.: bulk metallic glasses (BMGs)) werden in verschiedenen Testdomänen bewertet. Durch die Anwendung einer Reihe von materialwissenschaftlichen Konzepten wird eine umfassende Charakterisierung erreicht, die Informationen über thermomechanisch getriebene Strukturrelaxation und Kristallisationsverhalten in bestimmten Gruppen fortschrittlicher glasartiger Mehrkomponentensysteme liefert. Im Einzelnen werden folgende Untersuchungen an gewählten Legierungsgruppen durchgeführt:

- Der Einfluss von starker plastischer Verformung (SPD) ausgelöst durch Hochdrucktorsion (HPT) und isotherme Wärmebehandlung (HT) unterhalb des Glasübergangs auf die Struktur-Eigenschafts-Beziehungen vom $Cu_{46}Zr_{46}Al_8$ BMG wurde separat und abwechselnd untersucht in Bezug auf den Gusszustand. Kontrollierte Kristallisation wurde durch HT erreicht, und HPT wurde anschließend verwendet, um Kristalle in der gesamten Glasmatrix zu dispergieren. Die Dispersion der zweiten Phase verbesserte die thermomechanische Stabilität im Bereich der unterkühlten Flüssigkeit.

- Das viskoelastische Verhalten von vier verschiedenen BMG-Systemen, d. h. $Cu_{46}Zr_{46}Al_8$, $Cu_{44}Zr_{44}Al_8Co_4$, $Cu_{44}Zr_{44}Al_8Hf_4$ und $Cu_{44}Zr_{44}Al_8Co_2Hf_2$, wurde hinsichtlich seiner Verformungsmodusabhängigkeit mittels dynamisch-mechanischer Analyse (DMA) in 3-Punkt-Biegung (TPB) untersucht, Spannungs- und Torsionsmodi. Die Kristallisation verringert den viskoelastischen Beitrag, während die plastische Verformung zu einer Erhöhung der atomaren Mobilität führt. Im Vergleich zu $Cu_{46}Zr_{46}Al_8$, führt 4 at. % Co-Zugabe in der amorphen $Cu_{46-x/2}Zr_{46-x/2}Al_8Co_x$-Legierung zu

einem Glas, das eine relativ höhere thermomechanische Stabilität um seinen Glasübergang herum aufweist.

- $Ti_{40}Zr_{10}Cu_{36}Pd_{14}$-BMG ist als Material für orale Implantate vorgesehen, und seine Eigenschaften wurden im Vergleich mit dem Goldstandard-Implantatmaterial Ti–6Al–4V bewertet. DMA zeigte, dass diese Materialien thermomechanisch zu Implantaten geformt werden können. Hochauflösende Transmissionselektronenmikroskopie und Röntgenphotoelektronenspektroskopie zeigen die Bildung einer 15 nm dünnen Kupferoxidschicht auf $Ti_{40}Zr_{10}Cu_{36}Pd_{14}$ BMG. Im Gegensatz zu Titanoxid, das auf Ti–6Al–4V gebildet wird, ist Kupferoxid hydrophob und seine Bildung verringert die Oberflächenbenetzbarkeit. Eine geringere Besiedlung der Oberfläche mit Bakterien wurde durch Feldemissions-Rasterelektronenmikroskopie und Fluoreszenzbilder bestätigt.

- Die Aussichten von $Ti_{40}Zr_{10}Cu_{36}Pd_{14}$ BMG als orales Implantatmaterial werden hinsichtlich der Verarbeitung und der strukturabhängigen mechanischen Eigenschaften weiterentwickelt. Es werden Einblicke in die möglichen Verarbeitungswege gegeben, wobei Hochtemperatur-Formpressen über einen optimierten Prozess eingesetzt wurde, um sowohl die Kinetik der thermoplastischen Verformung zu bewerten als auch die bestimmten Eigenschaften der Legierung abzustimmen. Verarbeitete BMGs und BMG-Verbundwerkstoffe derselben Zusammensetzung weisen eine verbesserte thermomechanische Stabilität auf, wodurch mittels dynamisch-mechanischer Analyse eine hohe Festigkeitserhaltung bei um über 100 K höheren Temperaturen im Vergleich zum Guss-Zustand festgestellt wurde.

Contents

1 Introduction

1.1 Structure of metallic glasses

Metals are in general crystalline, but by cooling a molten metal at extreme cooling rates one can avoid the crystallization and achieve an amorphous metal, also called a metallic glass (MG). There are two types of glasses depending on their base material, i.e., metal-metalloid glasses and metal-metal glasses. MGs are multicomponent alloys with a composition close to a deep eutectic. X-ray diffraction (XRD) is often used to signify the amorphous state, which can be confirmed by transmission scanning microscopy (TEM). XRD of a MG is expected to show two broad maxima, on which no sharp (crystalline) peaks are superimposed (Figure 1a). TEM of a MG is expected to show mazelike patterns (Figure 1b) and halo rings in selected area electron diffraction without any spot distribution (Figure 1c).

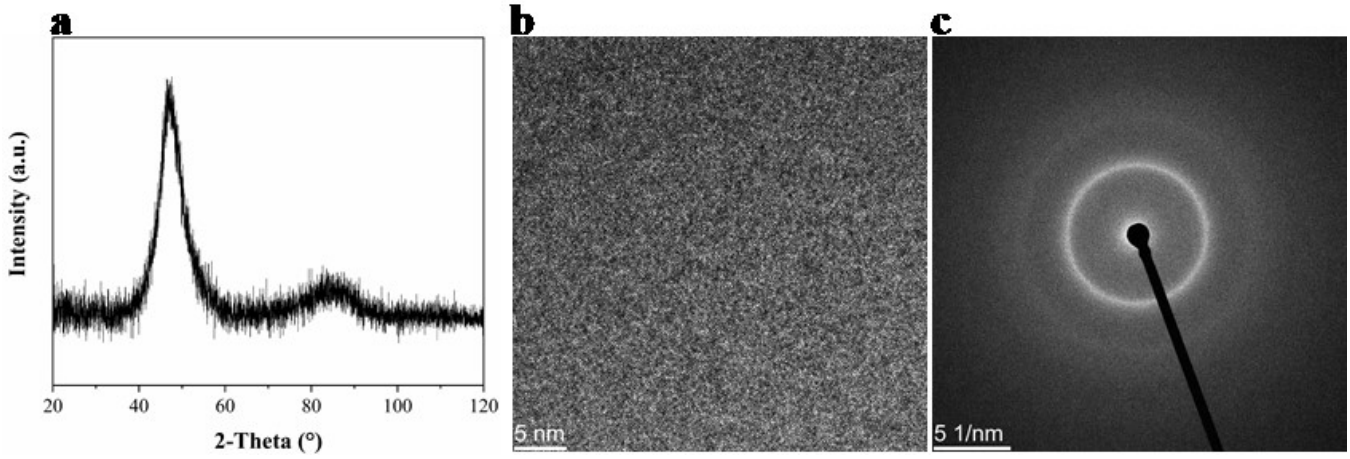

Figure 1. (a) XRD data, (b) high-resolution TEM, and (c) the corresponding selected area diffraction pattern of the as-cast $Ti_{40}Zr_{10}Cu_{36}Pd_{14}$ BMG.

1.2 Glass-forming ability

Certain empirical rules have been laid down to elaborate whether an alloy can be obtained in a glassy state [1]: The alloy needs to have three or more constituent elements, large atomic radii mismatch between the constituents (above 12%), and large negative mixing enthalpies of the constituents. The interior of bulkier

specimens cools down slower. So the critical cooling rate required to generate a glass determines the critical casting thickness – the maximum thickness, to which the sample can be glass throughout. The glass-forming ability (GFA) of the material is often referred to as being either proportional to its critical casting thickness or inversely proportional to its critical cooling rate. By convention, a bulk metallic glass (BMG) is a metal with a critical casting thickness of at least 1 mm. The GFA depends on a chemistry makeup. Hence, a dense atomic packing is a most clear trait observed in the best glass-forming BMGs [2]. From the thermodynamic viewpoint, the crystallization driving force is defined as the difference between the Gibbs free energies of the crystalline solid (X) and supercooled liquid (L) phases, $\Delta G = (H_L - TS_L) - (H_X - TS_X)$. H is the enthalpy, T is the absolute temperature, and S is the entropy. In the supercooled liquid region ($SCLR = T_x - T_g$), ΔG is always positive; of which, the higher values are indicative of the stronger inclination of the liquid towards crystallization and possession of lower GFA [3]. From a rheological viewpoint, the GFA is linked to the viscosity η. The rearrangement of atoms in order to crystallize takes place slower in viscous fluids. Supercooled liquids show an increase in viscosity as being cooled down towards the glass transition. Strong configurations show a high degree of restraint over its entire temperature range, whereas fragile configurations become unrestrained at high temperature. Strong liquids have in general higher GFA than fragile ones [4-6]. Thermodynamic and rheology are connected, an example is the Adams-Gibbs relationship, $\eta = Aexp\{B/[TS_C(T)]\}$. A and B are constants and S_C is the configurational entropy. Moreover, the feature of lower ΔG values and higher viscosity both have roots in the densely packed atomic structure in the supercooled liquid. Dense packing in liquids is attained via short-range order, with nearest-neighbor atoms organizing into crystalline shells that can expand up to nanometers across [7]; in metal-metal alloys, the shells are mainly icosahedral [8]. Such supercooled liquids are much alike crystalline solids at atomic scales, though they are disordered in structure at the

scales above. The Gibbs free energies of the liquid and solid phase are not of a large difference. Besides, atoms in a tightly packed structure have more difficulties moving past each other, the ordered arrangements result in increased viscosity. In both respects, dense packing improves GFA [9].

1.3 Fabrication of bulk metallic glasses

Suction casting is one of the main techniques to fabricate BMGs. Fig. 1 shows a 2D demonstration of an arc melter with an *in-situ* suction facility. In this PhD project, master alloys of $Cu_{46}Zr_{46}Al_8$, $Cu_{44}Zr_{44}Al_8Co_4$, $Cu_{44}Zr_{44}Al_8Hf_4$, $Cu_{44}Zr_{44}Al_8Co_2Hf_2$, and $Ti_{40}Zr_{10}Cu_{36}Pd_{14}$ were prepared in a Buehler AM0.5 arc melting system in a Ti-gettered argon atmosphere. The industrial-grade alloy constituents of 99.8% purity were weighed with an accuracy of ±0.001 g. Rotary and diffusion pumps were utilized to evacuate the system down to 10^{-6} mbar. Upon melting, the current was raised to a maximum of 150 A. To homogenize the ingots thoroughly, the melting was repeated four times. Using copper molds, the CuZr-based alloys were cast afterwards into rectangular plates of 10 mm in width, 75 mm in length, and 2 mm in thickness and the Ti-based alloys into rods of 3 mm in diameter and 60 mm in length. The pressure gradient between the mold cavity and the working chamber required for the suction was attained by purging argon into the chamber. It is important to consider that the fabrication of BMGs is limited to certain dimensions. Unfortunately, the reported critical casting thicknesses vary slightly due to impurity of alloys and non-ideal casting conditions.

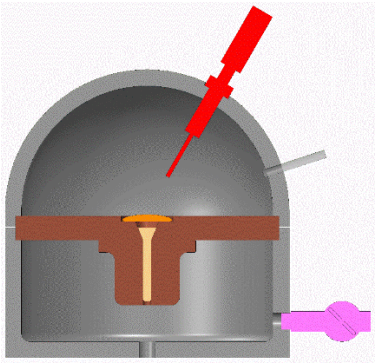

Figure 2. A demonstration of an arc melter suction casting device

1.4 Glass transition

The glass transition event is a prominent transformation in MGs. It is first-order phase transformations [10]. The glass transition temperature (T_g) is a cooling rate dependent parameter. It shifts to lower temperatures by imposing lower cooling rates. And higher cooling rates shift the glass transition to higher temperatures and thereby more free volume would be trapped in the glass. T_g can be identified upon changes in volume, enthalpy, or entropy as a function of temperature. The volume of a liquid decreases by being cooled continuously until the melting point, at which the liquid either crystallizes or vitrifies. Crystallization sets in at a certain undercooled state, in which rearrangement of mobile species form nuclei. There, the volume of the liquid decreases abruptly. However, crystallization can be bypassed via fast cooling in certain groups of compositions. Via supercooling, the atomic movements become slower and finally stop without finding an equilibrium. It means, the liquid turns to glass [11]. T_g is associated with a fixed viscosity of 10^{12} Pa s [11,12]. From a thermodynamic aspect, the glass transition event is necessary. Otherwise at the so-called Kauzmann temperature (T_k), the volume, the enthalpy, and the configurational entropy of the glassy state would become lower than those of the ordered crystalline state, which is not possible [13]. The free volume concept is an approach to elucidates the decline in mobility at the glass transition. Hence, the cooling driven relaxation of the glass to the SCLR annihilates the free volume and thus retards the diffusion of the atoms.

This increase the viscosity of the supercooled liquid [14]. Vitrification of the supercooled liquid is associated with the relaxation. The flow behavior of glasses is influenced by structural relaxation of the system. Relaxation time and viscosity are directly proportional. The viscosity of of 10^{12} Pa s at T_g implies a long relaxation time of around 1000s [12], which means the system cannot establish an equilibrium within an experimental time window. This emphasize the kinetic nature of glass transition.

1.5 Crystallization

The crystallization event is the second prominent transformation in MGs. Crystallization proceeds with nucleation by the formation of a solid-liquid interface and advances with the growth of the formed crystalline interface. Nucleation arises by thermal fluctuations of the liquid prompting the transient appearance of clusters of a new phase within a parent phase. Clusters form and decay continuously and spontaneously. The cluster regions are called nuclei after reaching a critical size. Smaller clusters are called undercritical nuclei or embryos that decay, as their interface-to-volume ratio is large. Larger clusters are called supercritical nuclei and they grow and lower the energy. Via undercooling, the formation of critical nuclei dominates over decay [15]. The driving force of crystallization is the difference between the free energy of the liquid and crystalline state. Below the melting temperature (T_m), the melt is not stable and tends to transform to the crystalline state. The activation energy (AE) of crystallization can be calculated from the shift of the crystallization peak stemmed from the variation of the heating rate [16].

1.6 Fragility concept

The viscosity of strong liquids shows an Arrhenius behavior [17]:

$$\eta = \eta_0 exp\left\{-\frac{E_a}{RT}\right\}, \tag{1.1}$$

where η is the viscosity, the pre-exponential constant (η_0) is the viscosity at infinite temperature, E_a is the activation energy, R is the universal gas constant and T is the temperature. However, the viscosity of fragile liquids shows non-Arrhenius behavior and the viscosity data can be estimated by the empirical Vogel-Fulcher-Tammann (VFT) equation [18]:

$$\eta = \eta_0 exp\left\{\frac{B}{T - T_0}\right\}, \tag{1.2}$$

where B is a constant with the dimensions of temperature, and T_0 the Vogel-Fulcher-temperature. When $T \to T_0$, $\eta \to \infty$ and the structure will freeze in. T_0 is a kinetic instability point [19]. Fragility is defined as the temperature dependence of the viscosity for a liquid. This temperature dependency of the viscosity can be quantified by the slope of the Angell plot close to T_g [20], which yields the steepness index (m) defined as fragility.

$$m = \left.\frac{dlog\eta}{d\left(\frac{T_g}{T}\right)}\right|_{T=T_g}, \tag{1.3}$$

Larger m values are indicative of a more fragile behavior of the iquid. This means the dependency of viscosity on the temperature close to T_g along with the deviation from Arrhenius behavior is more pronounced. Fragile liquids show a rapid breakdown of shear resistance in the course of heating. BMGs possess the

steepness index between 30 and 40 [21]. A modified expression of the steepness index is laid down by Brüning and Samwer [22]:

$$m = \frac{T_g B}{ln\ 10\left(T_g - T_0\right)^2}, \tag{1.4}$$

from which the heating rate and T_g can be correlated:

$$\varphi = Aexp\left\{\frac{B}{\left(T_g^0 - T_g(\varphi)\right)}\right\}, \tag{1.5}$$

where φ is the heating rate, A is a pre-exponential factor, B is the activation energy, T_g^0 is the asymptotic value of T_g in the limit of infinitely slow cooling and heating, and $T_g(\varphi)$ is the heating rate-dependent T_g. Furthermore, the fragility of a liquid is intimately linked to Poisson's ration (ϑ) as an important parameter that controls the fragility of liquids [23]. Hence, fragility as an extent of non-Arrhenius viscosity can be determined by the short-time relaxation processes in liquids [24] considering that liquids behave like solids as being looked into within a time window much shorter than a usual relaxation time. It has been suggested, that this is correct if ϑ is normalized with respect to molar volume [25]. It has been reported that the critical casting thickness of a glass-forming liquid is correlated to ϑ, as a densely packed atomic structure prevents atomic rearrangements, of which the bonding configurations stay intact [26]. Furthermore, T_g and T_x are reported to be in linear correlation with elastic modulus (E), shear modulus (G), and bulk modulus (B) [27,28]. BMGs possessing higher ϑ are more inclined to shear without fracture and those possessing lower ϑ are less ductile. It is important to consider that relative ductile BMGs are cast despite lower GFA.

1.7 Structural relaxation and rejuvenation

MGs urge to convert to the metastable state if the driving force is present. Hence, temperature rise can recover the ceased atomic mobility, thereby relaxing the glass into the metastable equilibrium. Relaxation involves atomic rearrangements causing a more ordered atomic distribution without the long-range diffusion of atoms. Glasses are inclined to change their out-of-equilibrium configuration via relaxation to become more stable. The primary relaxation corresponding to glass transition is called α and the secondary corresponding to stiffening β. It can be expected that glasses showing pronounced β relaxations at lower temperatures are relative ductile. One can deviate the system from equilibrium and bring it to a higher energy state, defined as a rejuvenation process. Relaxation annihilates the free volume in the structure and leads thereby to the embrittlement of MGs, whereas rejuvenation causes dilatation (i.e., generation of free volume) and enhances thereby the plasticity of BMGs. Relaxation and rejuvenation can be considered as processing routes to grant MGs certain functionalization. Relaxation of MGs can be achieved via a controlled sub-T_g heat treatment pursuing definite protocols and rejuvenation can be achieved via severe plastic deformation of definite parameters [29]. Dynamic mechanical analysis (DMA) is a technique to manifest the effects from the thermo-mechanically driven structural relaxation and rejuvenation in BMGs. Figure 3 shows the DMA data of the $Ti_{40}Zr_{10}Cu_{36}Pd_{14}$ BMG together with explanations.

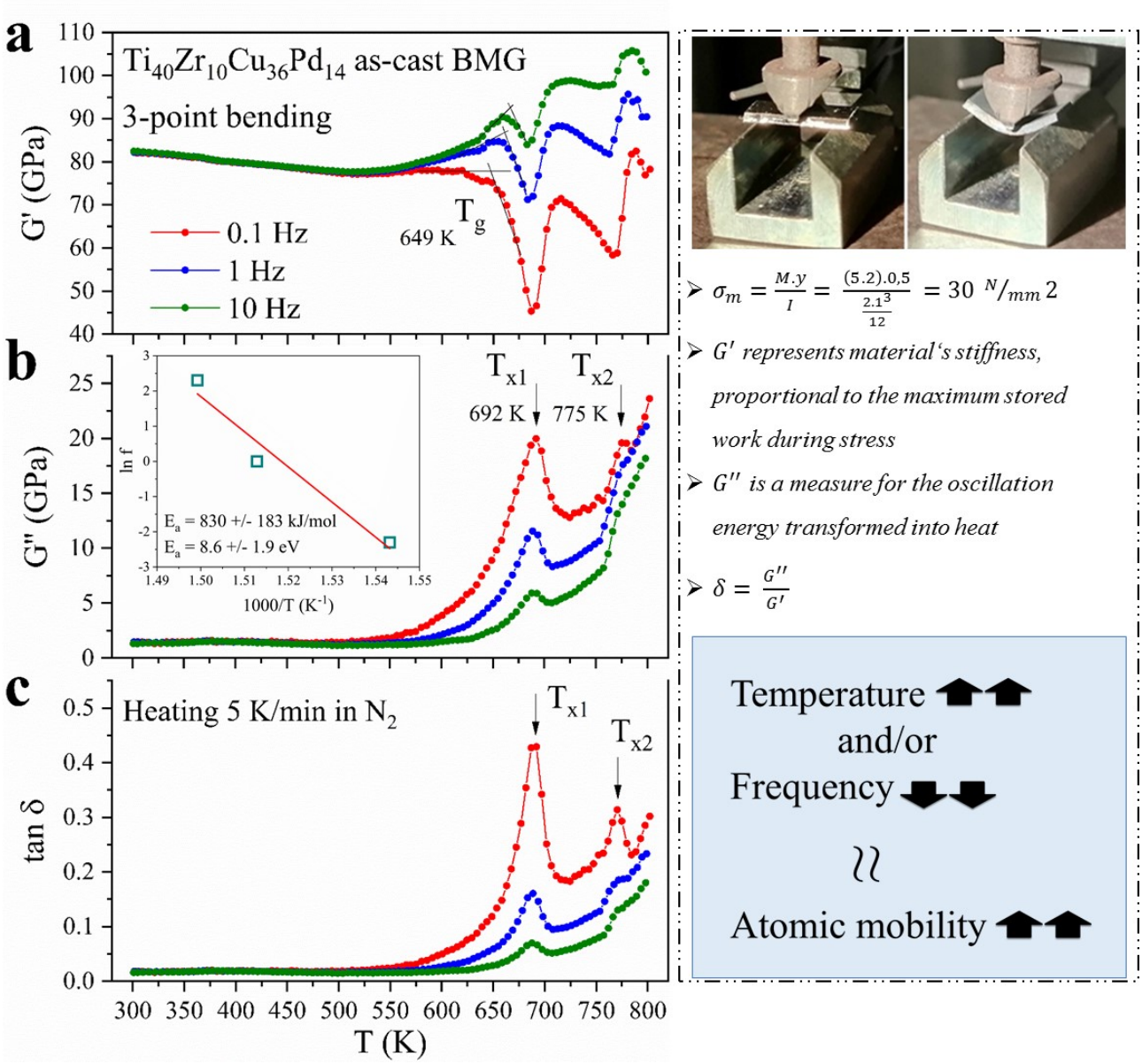

Figure 3. (a) Storage modulus (G'), (b) loss modulus (G"), and (c) loss factor (tan δ) of the $Ti_{40}Zr_{10}Cu_{36}Pd_{14}$ BMG as a function of temperature. The measurement frequencies were 0.1 to 1 to 10 Hz, and the heating rate was 15 K/min. The T_g measurements at different frequencies result in a linear Arrhenius behavior with a slope of 8.6 ± 1.9 eV obtained from the slope of the linear fit (inset). Explanations are added to clarify the data.

1.8 Deformation of metallic glasses

Metallic glasses undergo highly localized, heterogeneous deformation at room temperature. BMGs are elastically isotropic, however in some cases anisotropy can be induced either upon processing or as the result of external fields. The bulk and shear moduli (B and G) of an isotropic material represent the response to

hydrostatic and shear stresses. Compared to crystalline alloys, BMGs of the same compositions show ~6% lower bulk moduli [30] and the shear moduli in BMGs are ~30% of those in their corresponding crystals [31]. G can be defined mathematically as [32-34]:

$$\left.\frac{d^2\emptyset}{d\gamma^2}\right|_{\gamma=0} = G\,, \tag{1.6}$$

Where $\emptyset$ is the potential energy and γ is the shear strain coordinate. At $\gamma = 0$:

$$\emptyset_0 = \left(\frac{8\gamma_c^2}{\pi^2}\right) G\,. \tag{1.7}$$

The plastic deformation starts at the critical shear strain (γ_c). Physically, the shear moduli of certain regions gradually become smaller, which allows the rearrangement of atoms. The total energy barrier of the flow can be defined as the product of the amplitude of the sinusoidal function (φ_0) and the shearing volume (Ω) [32]:

$$W = \varphi_0\Omega = \left(\frac{8\gamma_c^2}{\pi^2}\right) G\Omega\,. \tag{1.8}$$

Two conclusion can be drawn: Larger shear moduli lead to larger energy barrier plus the rearrangement of the large number of atoms require a large energy input and is otherwise unlikely. G as a key parameter to determine the deformation behavior of BMGs can be looked at in two regions: Below T_g, G increases linearly as the temperature decrease. Above T_g, G drops exponentially as the temperature

increases. G of a supercooled liquid behaves like temperature-dependent viscosity of fragile liquids, which can be explained via [30]:

$$\frac{\eta}{\eta_0} = exp\left\{\frac{W_g}{K_B T} exp\left\{\frac{2}{n}\left(1 - \frac{T}{T_g}\right)\right\}\right\}, \tag{1.9}$$

where η_0 is the viscosity at infinite temperature, W is the energy barrier between two inherent states of the system, K_B is the Boltzmann constant, and n is a fitting parameter. The equation is reported to match with experimental data [33]. Moreover, the viscosity of the glass-forming melts can be explained slightly different via [35-37]:

$$\frac{\eta}{\eta_0} = exp\left\{\frac{G_g V_c}{K_B T} exp\left\{\gamma\left(1 - \frac{T}{T_g}\right)\right\}\right\}, \tag{1.10}$$

where V_c is a characteristic volume and γ is a constant. Melting is the softening of G meaning that the lower viscosity in the liquid state stems from the reduced resistance against shear. Hence, G acts as a thermodynamic state variable governing the flow.

1.8.1 Free volume and entropy models

Another framework to explain deformation of BMGs is laid out using the "free volume" model [38]. The model can be explained via [39]:

$$\eta = \eta_0 exp\left\{\frac{C}{\vartheta_f}\right\}, \tag{1.11}$$

where C is a constant and ϑ_f is the free volume. This model consider deformation as a series of discrete atomic jumps in the glass, these jumps are triggered near

the sites of higher free volume via a diffusion-like process. The activation energy (AE) of diffusion is 15 to 25 kT_g.

An alternative framework to explain deformation of BMGs is put forward using the "entropy volume" model [40]. The model can be explained via:

$$\eta = \eta_0 exp\left\{\frac{C}{TS_c(T)}\right\}, \tag{1.12}$$

where C is a constant, T is the temperature, and $S_c(T)$ is the configurational entropy defined as the non-vibrational fraction of the excess entropy, whereas excess entropy is the entropy difference between the glassy state and crystalline state.

1.8.2 Shear transformation zone theory

Deformation of metallic glasses is a local rearrangement of atoms that accommodate shear strain. A shear transformation zone (STZ) as a unit of plasticity in MGs is a local cluster of atoms undergoing an inelastic shear deformation [41]. Figure 3 shows a demonstration of a simple STZ composed of 9 close-packed atoms.

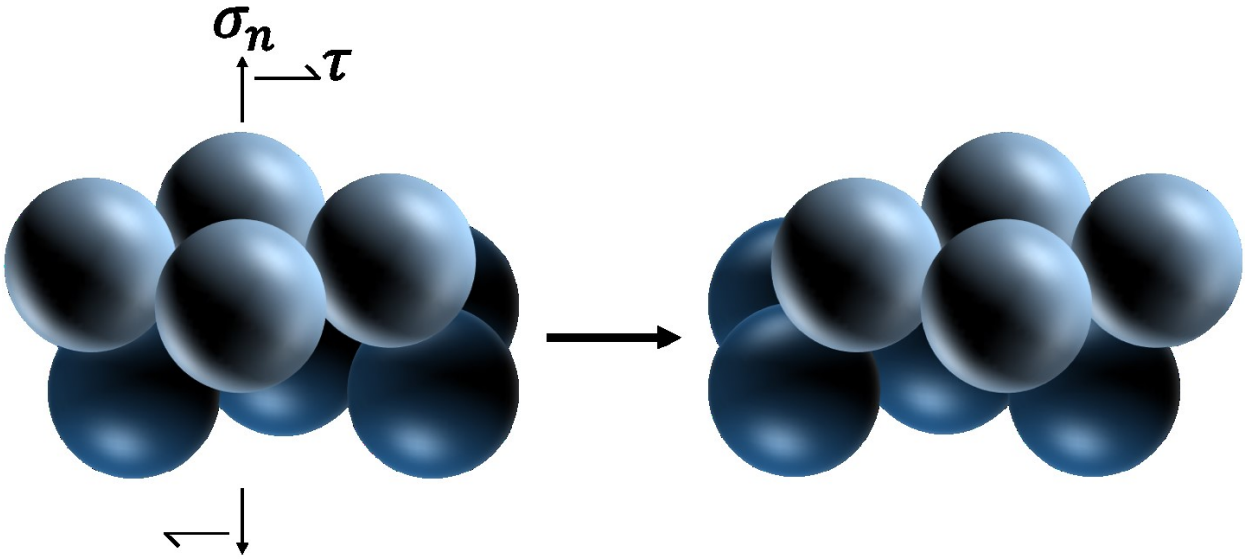

Figure 4. A demonstration of shear transformation zone showing the movement of the four upper atoms as a unit with respect to the five lower atoms [42].

The AE of a STZ can be quantified as:

$$\Delta F_0 = \left[\frac{7-5\vartheta}{30(1-\vartheta)} + \frac{2(1+\vartheta)}{9(1-\vartheta)}\beta^2 + \frac{1}{2\gamma_0}\cdot\frac{\tau_0}{G(T)}\right]\cdot G(T)\cdot {\gamma_0}^2\cdot\Omega_0\,, \quad (1.13)$$

where β is the ratio of free volume generation to shear strain, $G(T)$ is the temperature-dependent shear modulus, τ_0 is the critical non-thermal shear stress, γ_0 is a characteristic strain of an STZ with values of ~0.1 order [43], and Ω_0 is the characteristic volume of an STZ that encloses atoms up to ~100 [32,44]. An STZ has the size of ~1 nm [41]. Using typical values of transition metals, the energy of an STZ yields the approximate values of 1 to 5 eV / 20 to 120 kT_g. k is the Boltzmann constant. The lower values are close to AE values of diffusion in the "free volume" model, the AE of an STZ is in correspondence to a cooperative motion of a larger group of atoms in comparison. The pronounced β relaxations of a system suggest that the glass possesses abundant STZs, and plasticity is then expected to see when the high density STZs are activated to reach the percolation

limit upon external stresses. Via deformation, the strain is accommodated in narrow regions in MGs, the so-called shear bands (SB) initiated from shear transformations. The plastic deformation of BMGs via shear-banding is associated with the biased accumulation of local strains introduced by the operation of STZs and the redistribution of free volume. SBs possess lower viscosities compared to the matrix and form along planes that closely approximate those of maximum shear stress and they are ~20 nm thin. Their fracture surfaces exhibit vein-like patterns corroborating the fracture of a pure shear mode [41]. SB engineering is possible to tune the specific properties of MGs.

1.9 Thermoplastic net-shaping

BMGs in many applications require a net-shape manufacturing as direct casting is limited to simple shapes such as rods and plates. The synthesis of BMGs possessing thin sections with high aspect ratios via direct mold casting is very much challenging. The driving force to fill the mold cavity is a bias of pressure gradient. The work material is supposed to undergo deformation and not the mold. Therefore, the mold material has to possess a higher strength than the work material at the molding temperature. As an estimate, an order of magnitude higher strength of the mold material can be a guideline. If the flow stress of a liquid as the product of viscosity and strain rate multiplied together is low in its SCLR, the molding is facilitated. Thermoplastic net-shaping (TPN) of BMGs is a two-stage process, by which casting and forming are separated. Therewith, the cast glasses undergo deformation at sub-T_x temperatures, at which they exhibit their highest plasticity. Also, micro-patterned and hierarchically modulated surfaces can be generated via TPN [45]. However, the marginal GFA and the high inclination of some alloys towards oxidation can cause limited formability, it means the resistance against flow can restrict the patterning to micro-features with specific heights and rounded corners [46]. MGs show sluggish crystallization kinetics in

their SCLR, which grants a net-shape processing route of a convenient time scale. Herewith, the material can be processed within a much longer time window. Metallic glasses have advantageous from the processing viewpoint. The difficulty with crystalline metals is that they are in the course of heating either too hard (strength values of above 100 MPa) or too soft (strength values below 10^{-7} MPa), they somehow jump over at where we actually want them to be with a phase transition going from a solid to a liquid. Whereas, BMGs can be present in an ideal region, where they show plastic-like processability with the strength of below 10^{-7} MPa and the viscosity of 10^3 – 10^8 Pa s. GFA defines critical casting diameter of a material from the liquid state, though it is not a good indicative of the formability of a material. Whereas, the S parameter, obtained by dividing the width of the SCLR ($T_x - T_g$) to the undercooled liquid region ($T_l - T_g$), can be a good indicative. This parameter is solely extracted from the thermophysical data. It is independent of a time and/or temperature dependent rheological analysis and thereby renders unified data evaluation and significant experimental advantage [47].

1.10 CuZr-based glassy alloys and glass composites

CuZr-based melts are reported to vitrify into glasses at higher cooling rates [48-50]. MGs including CuZr-based ones have many current and potential applications such as in recreational items because of the bouncing effect coming from ultra-high resilience of BMGs [51]. MGs show low friction and wear and are suitable for use as corrosion and wear-resistant coatings in heavy machinery and they are beneficial in space robotics since they do not become brittle in cold and show low friction and wear [52,53]. MGs are exploited in precision tooling and high-end products [54], a MG blade can be sharpened to an exceptional edge, as no above-atomic length scale would limit that [55]. And they are widely used in electronics due to magnetic properties of MGs [56]. Special selection of the alloy compositions and cooling rates can render the formation of bulk metallic

glass composites (BMGCs). For example, in the binary $Cu_{50}Zr_{50}$, the high temperature B2 CuZr phase can precipitate from the melt upon cooling, The B2 is a shape memory alloy [57]. The shape memory effect arises from the stress/strain-induced transformation of the B2 (Pm3m) to two monoclinic phases, B19′ ($P2_1/m$) [58] and B33 (Cmcm) [57,59]. B33 is the superlattice of B19′ [60]. Via further cooling, the high energy B2 decomposes to the equilibrium phases, $Cu_{10}Zr_7$ and $CuZr_2$. BMG composites with shape memory B2 CuZr crystals embedded in the amorphous matrix show excellent strength and plasticity without significant trade-off but exhibit work hardening [61]. The mechanical performance of a metallic glass depends on its size, hence glasses with an effective thickness exceeding 1 mm are usually brittle. This can be though overcome by incorporating a second phase into the glass to stimulate shear band proliferation [41]. The second phase can be dispersed crystals in the glassy matrix to enhance the plasticity of the BMGs. Regarding the deformation of the BMGCs in the elastic-plastic regime, elastic deformation of the glassy matrix makes the plastic deformation of the crystalline phases more homogeneous, leading to the work-hardening. The coordinated plastic deformation occurs between the glassy matrix and the crystalline phase in the plastic-plastic region, the shear bands nucleate and traverse along with the interface, and then split into multiple shear bands. Deformation of the B2 phase is hindered by the glassy matrix, which triggers the stress/strain-induced transformation in the B2 crystals, also causing work hardening. When multiple shear bands branch and de-bond at the interface between crystal and glass, the work-hardening effect of the crystalline matrix weakens and softening of the glassy matrix overwhelms the deformation of the BMGCs, which can lead to softening and necking. Moreover, diffusion-controlled crystallization is also beneficial to enhance the strength retention at temperatures around T_g. [29]. Al addition can enhance the GFA of the plain alloy [62,63]. Alloying additions has been advanced in a broad range to develop new MGs with improved properties. This PhD project is believed to provide insight

into the impact of the microalloying by Co and/or Hf additions on the mechanical performance of CuZrAl-based BMGs at elevated temperatures.

1.11 $Ti_{40}Zr_{10}Cu_{36}Pd_{14}$ Bulk metallic glass

Among advanced glassy multicomponent systems, Ti-based BMGs are exploited as biomedical materials primarily due to the bioactivity of the Ti element. $Ti_{40}Zr_{10}Cu_{36}Pd_{14}$ bulk metallic glass is free of toxic elements, such as Al, Ni and Be. Compared to Ti-6Al-4V as the current gold standard implant alloy, it has lower Young's modulus and thereby mitigated stress shielding effect [64] and also higher strength and oxidation resistance. The antibacterial properties rely on the prohibition of bacterial attachment. The formation of CuO on $Ti_{40}Zr_{10}Cu_{36}Pd_{14}$, compared to TiO2 on Ti–6Al–4V, provides higher water contact angles decreasing the chance of bacterial attachment. Moreover, CuO reduces the bacterial metabolic activity of the oral pathogen Aggregatibacter actinomycetemcomitans while increasing the cytocompatibility of the fibroblasts, which prevents the formation of harmful oral biofilm [65]. It has been shown in this PhD project that high-temperature compression molding with an optimized process can introduce various structural modifications into the $Ti_{40}Zr_{10}Cu_{36}Pd_{14}$ BMG during the replication. Hence, crystallization on different length-scales can be generated depending on the processing conditions. The processed $Ti_{40}Zr_{10}Cu_{36}Pd_{14}$ glass composites show extraordinary strength retention at temperatures, compared to the cast glass, by above 100 K higher [65]. The observed crystals in the glassy matrix are of B2-TiZr, $CuTi_2$, $CuTi_3$, and Cu_3Ti_2 phases. Looking into the structure discloses that spherulites enclosed by semi-crystalline outer shells appear in the $Ti_{40}Zr_{10}Cu_{36}Pd_{14}$ BMG. The shells serve as a synergy between order and disorder in the matrix. Larger needle-shaped Cu_3Ti_2 crystalls form centric in the spherulites. To these crystalline phases finer needles of tetragonal CuTi attach at 90°. Rather at the center of spherulites, $CuTi_3$ phases of a few percent might precipitate throughout solidification upon eutectic

reactions since the cooling rate is set at its threshold in casting in order to produce the largest possible bulk glass. The B2 phase is observed primarily in mature spherulites. It nucleates around the tetragonal CuTi crystals and grows in all directions to the shell. This gives the spherical shape to the spherulites [66].

1.12 Bioactivity

The design and selection of a biomaterial depend on its intended medical application. Synthesis of a new biomaterial is a collaborative effort in interdisciplinary fields. It needs to possess certain attributes to serve in the body without rejection. More specific, an implant material needs to be non-toxic and not cause any inflammatory or allergic reaction in the body. The success of an implant primarily depends on the reaction of the body, and this is referred to as the biocompatibility of a material made up of host response and the degradation of the material in the body. A class of materials called bioactive are considered as highly biocompatible since they promote the integration with surrounding bone. A not biocompatible implant can cause the blood to coagulate to the implant surface called thrombosis. Another complication can be fibrous encapsulation of an implant. An implant material of low wear and corrosion resistance of material releases harmful metal ions in the body. The abrasion of an implant makes it become loose and shortens its service period. Hence, the wear/corrosion debris are not desired. Soluble debris goes to the blood. And particulate debris accumulates in the human tissue. This accumulation can cause inflammation, damage of cell tissue, hypersensitivity, chromosomal aberrations, toxicity and carcinogenicity. Therefore, the application of a biomaterial with high wear and corrosion resistance is of prime importance. The application of an implant cannot succeed if it is not well osseointegrated. Osseointegration refers to the integration of an implant with the adjacent bone and other tissues. The failure of this integration leads to the formation of a fibrous tissue and loosening of the implant. Surface chemistry and surface topography primarily determine how good the

osseointegration would be. Among advanced glassy multicomponent systems, Ti-based BMGs are heavily made use of in biomedical applications primarily because of the bioactivity of the Ti element. Their unique softening and tunability of flow stress in the SCLR allow the generation of hierarchically modulated surfaces which can act as topographic cues for cell attachment and differentiation. This facilitates a strong cell-material interaction. The micropatterend structures are exploited for guided tissue generation in implantology to facilitate the process of osseointegration and biomechanical fixation [67,68]. Such topography can promote the cellular response from initial attachment and migration to differentiation and growth of new tissue without the need of having exogenous growth factors. $Ti_{40}Zr_{10}Cu_{36}Pd_{14}$ BMG is free of toxic elements, such as Al, Ni and Be. It possesses low Young's modulus (82 GPa) and thereby minimizes the stress-shielding effect. Implant materials stiffer than bone, prevent the stress to transfer to the adjacent bone, which causes bone resorption and implant loosening. This biomechanical incompatibility is called stress-shielding effect and ceases the bone cells [64]. It is believed that $Ti_{40}Zr_{10}Cu_{36}Pd_{14}$ as an oral implant material does not cause anti-biofouling, but promotes the selective growth of dental pulp stem and epithelial cells.

2 Summary of the results

Tuned $Cu_{46}Zr_{46}Al_8$ with modifications in the structure via sub-T_g HT and HPT treatments leads to a glass of an improved performance. Casting a 40 mm diameter and 2 mm thick plate of this composition produces a fully glass. HPT process does not induce crystallization but slightly increases T_g. At the early stage of sub-T_g HT, the B2 phase in nano/micro-scale precipitates. The multi-axial stress upon HPT can cause the intersections of the SBs confirmed by SEM, this serves as nucleation sites in the glassy matrix and promotes the nucleation of HT-induced crystals over the matrix. A uniform dispersion of the crystals can be obtained by taking an alternate order of the treatments, i.e., first HT followed by

HPT. The HT + HPT BMG shows an even hardness profile with a relatively higher Vickers hardness in comparison to the as-cast, and it is thermomechanically more stable based on dynamic mechanical analysis (DMA). These findings highlight the fact, that a combination of annealing and plastic deformation treatments is a promising approach to produce BMGs with specifically tuned properties. To broaden the concept, the viscoelastic behavior of four different BMG systems, i.e., $Cu_{46}Zr_{46}Al_8$, $Cu_{44}Zr_{44}Al_8Co_4$, $Cu_{44}Zr_{44}Al_8Hf_4$, and $Cu_{44}Zr_{44}Al_8Co_2Hf_2$, is manifested on the deformation-mode dependence via DMA in 3-point bending (TPB), tension and torsion modes. At temperatures below the T_g, they deform mainly elastic, and the materials respond independent of the driving frequency, however, in the SCLR, the visco-elastic component takes over. Crystal nucleation and growth mitigate the visco-elastic contribution, whereas plastic deformation raises the atomic mobility. The material of the plain composition explored under the TPB mode exhibits an increase in the storage modulus G' from 89 ± 1 GPa to 105 ± 1 GPa showing an obvious relaxation. The high value of the AE is indicative of a collective movement of atoms evolved in the relaxation. Upon TPB, the oscillation of the individual atoms evolves, through percolation process with the same phase, into a collective oscillation of a larger groups of atoms. This leads to ordering of atoms and thereby to elastic stiffening of the system. Unlike TPB mode, tension and torsion generated free volume in the structure does not promote the relaxation of the system. In this case, each atom practically oscillates around its position within its phase. Therewith, atomic rearrangements in the long-range order are barely conducive as the interatomic distances are larger than the range of the damped oscillation. Therefore, a cooperative structural relaxation is hence not possible. With the tension- and torsion-mode types, no relaxation of the glasses is determined. In the tension, the glass transition event takes place at higher temperatures. It means, a larger thermo-mechanical driving force is required to visualize the modifications in tension compared to TPB and torsion, this can be

regarded as a disadvantage of the tensile testing. By imposing 10 N, the stress in tension is 10 N/mm2 over the sample, however in TPB, the maximum stress reaches 120 N/mm2. Hence, the stress in the TPB mode can induce the stress/strain-induced transformation and thereby crystallization occurs at lower temperatures. Besides, a clear second glass transition peak (T_{g2}) in loss modulus is identified via TPB. These findings highlight that, TPB at 1 Hz frequency can induce a complex stress state and thus trigger two different relaxation modes stage-by-stage until reaching T_x. XRD and TEM confirm the amorphous state of the plain composition and structural modifications when heated to 743 K [69]. Compared to $Cu_{46}Zr_{46}Al_8$, by introducing 4 at. % Co addition in the $Cu_{46-x/2}Zr_{46-x/2}Al_8Co_x$, amorphous phase separation sets in between softer Cu-rich and harder Co-rich regions in the structure of $Cu_{44}Zr_{44}Al_8Co_4$ because of the positive heat of mixing of Cu-Co (6 kJ/mol) [69]. This suggests the strength retention around the SCLR. To develop concepts in the framework of biomedical materials, the biological safety investigation of alloys is a matter of utmost importance to avoid any adverse reaction [65]. The intrinsic nature of $Ti_{40}Zr_{10}Cu_{36}Pd_{14}$ BMG as an oral implant material is decoded to evaluate its use as an oral implant. The viscoelastic of $Ti_{40}Zr_{10}Cu_{36}Pd_{14}$-BMG demonstrated upon compression. A driving frequency of 1 Hz visualizes the supercooled liquid region. The formation of CuO on $Ti_{40}Zr_{10}Cu_{36}Pd_{14}$, compared to TiO_2 on Ti–6Al–4V, yields higher water contact angles and thereby reduce the bacterial attachment. Furthermore, CuO decreases the bacterial metabolic activity of the oral pathogen A. actinomycetemcomitans while increasing the cytocompatibility of the fibroblasts, this inhibits the formation of harmful oral biofilm on an implant. To advance the envision of $Ti_{40}Zr_{10}Cu_{36}Pd_{14}$ BMG as oral implant material, the effect of TPN, the process required to reach the final desired shape of the implants, is investigated on the microstructure and cytocompatibility of the glassy alloy. DMA confirms that optimized thermoplastic processing leads to BMGs and BMG composites showing a more stabilized G' up to ~700 K, revealing an increase in

the thermomechanical stability by above 100 K in comparison to the as-cast glass. Cytocompatibility tests are performed via seeding human gingival fibroblast cells (HGF) directly onto the $Ti_{40}Zr_{10}Cu_{36}Pd_{14}$ BMGs after TPN, using the as-cast $Ti_{40}Zr_{10}Cu_{36}Pd_{14}$ BMG as control. The results demonstrate that TPN does not adversely affect the cytocompatibility. On the other hand, the formation of ~100 nm thin surface layers consisting of Ti, Cu, and Zr oxides improves cells attachment. The attributing factor for this improvement is related to the presence of titanium oxide on the surface that significantly improves the surface wettability.

3 Conclusion and outlook

In an attempt to improve the structure-dependent mechanical performance of selected multicomponent alloys, optimized processing routes are pursued to design advanced alloys with tailored adjustments. Certain two-stage treatment of annealing and plastic deformation on the $Cu_{46}Zr_{46}Al_8$ BMG generates a $Cu_{46}Zr_{46}Al_8$ composite showing a higher thermomechanical stability. Along this line, 4 atomic percent Co addition in the $Cu_{46\_x/2}Zr_{46\_x/2}Al_8Co_x$ glass leads to a glass showing higher dynamic mechanical stability at elevated temperatures. 3-point bending at 1 Hz is conducive to register the SCLR and visualize the structural relaxation and crystallization kinetics of CuZr-based BMGs. The viscoelastic behavior of $Ti_{40}Zr_{10}Cu_{36}Pd_{14}$ BMG reveals a promising thermoplastic processing routes. The processed $Ti_{40}Zr_{10}Cu_{36}Pd_{14}$ BMGs and BMG composites show superior strength retention at temperatures in comparison to the cast glass.
The study of the structure-property relationships in MGs is rather lean as there is no long-range atomic order in the structure. Besides, it is difficult to lay down the thermomechanical stress state of BMGs at extreme temperatures and high loading domains due to the temperature and pressure-dependent crystallization events around SCLR. In this regard, investigation of the relaxation and crystallization behavior of BMGs exposed to thermomechanical driving forces under controlled laboratory domains is an approach to estimate how the material's response would

be in harsh and real environments. Concepts are developed to evaluate the $Ti_{40}Zr_{10}Cu_{36}Pd_{14}$ glass and glass composite envisioned as an oral implant material. The formation of copper oxide on $Ti_{40}Zr_{10}Cu_{36}Pd_{14}$ BMG, compared to titanium oxide on Ti–6Al–4V as the current gold standard implant alloy, reduces the bacterial viability. Hence, the formation of bacterial biofilm is hampered. TPN as a processing route required to reach the final desired shape of the implants, leads to glassy and composite $Ti_{40}Zr_{10}Cu_{36}Pd_{14}$ showing extraordinary thermomechanical stability. The formation of ~100 nm thin surface layers consisting of Ti, Cu, and Zr oxides improves cells attachment. As the demand to have biomedical materials of utmost functionalities are getting higher, the need of interdisciplinary frameworks to evaluate the performance of biomaterials is higher than ever.

References

[1] Takeuchi, A. & Inoue, A. (2005) Classification of bulk metallic glasses by atomic size difference, heat of mixing and period of constituent elements and its application to characterization of the main alloying element. Materials Transactions. 46. 2817-2829. 10.2320/matertrans.46.2817.

[2] Schroers, J. (2013) Bulk metallic glasses. Physics Today. 66. 32-. 10.1063/PT.3.1885.

[3] Busch, R. & Schroers, J. (2007) Thermodynamics and kinetics of bulk metallic glass. MRS Bulletin. 32. 10.1557/mrs2007.122.

[4] Park, E. S. & Na, J. H. & Kim, D. H. (2007) Correlation between fragility and glass-forming ability/plasticity in metallic glass-forming alloys. Applied Physics Letters. 91. 031907 - 031907. 10.1063/1.2759266.

[5] Tanaka, H. (2005) Relationship among glass-forming ability, fragility, and short-range bond ordering of liquids. Journal of Non-Crystalline Solids. 351. 678-690. 10.1016/j.jnoncrysol.2005.01.070.

[6] Shadowspeaker, L. & Busch, R. (2004) On the fragility of Nb-Ni-based and Zr-based bulk metallic glasses. Applied Physics Letters. 85. 2508-2510. 10.1063/1.1796523.

[7] Laws, K. J. & Miracle, D. B. & Ferry, M. (2015) A predictive structural model for bulk metallic glasses. Nature Communications. 6. 8123. 10.1038/ncomms9123.

[8] Wanderka, N. & Macht, M. P. & Seidel, M. & Mechler, S. & Ståhl, K. & Jiang, J. Z. (2001) Formation of quasicrystals in Zr46.8Ti8.2Cu7.5Ni10Be27.5 bulk glass. Applied Physics Letters. 77. 3935 - 3937. 10.1063/1.1329636.

[9] Cheng, Y. Q. & Ma, E. (2011) Atomic-level structure and structure–property relationship in metallic glasses. Progress in Materials Science. 56. 379–473. 10.1016/j.pmatsci.2010.12.002.

[10] Turnbull, D. (1969) Under what conditions can a glass be formed?. Contemporary Physics. 10. 473-488. 10.1080/00107516908204405.

[11] Ediger, M. D. (2000) Spatially heterogeneous dynamics in supercooled liquids. Annual Review of Physical Chemistry. 51, 99-128. 51. 99-128. 10.1146/annurev.physchem.51.1.99.

[12] Dyre, J. C. (2006) Colloquium: The glass transition and elastic models of glass-Forming liquids. Reviews of Modern Physics. 78. 953-972. 10.1103/revmodphys.78.953.

[13] Kauzmann, W. (1948) The nature of the glassy state and the behavior of liquids at low temperature. Chemical Reviews. 43. 10.1021/cr60135a002.

[14] Cohen, M. H. & Turnbull, D. (1959) Molecular transport in liquids and glasses. The Journal of Chemical Physics. 31. 1164-1169. 10.1063/1.1730566.

[15] Cahn, J. W. & Hillig, W. B. & Sears, G. W. (1964) The molecular mechanism of solidification. Acta Metallurgica. 12. 1421-1439. 10.1016/0001-6160(64)90130-0.

[16] Kissinger, H. E. (1957) Reaction kinetics in differential thermal analysis. Analytical Chemistry. 29. 10.1021/ac60131a045.

[17] Angell, C. A. (1988) Perspective on the glass transition. Journal of Physics and Chemistry of Solids. 49. 863–871. 10.1016/0022-3697(88)90002-9.

[18] Angell, C. A. & Ngai, K. L. & Mckenna, G. B. & McMillan, P. F. & Martin, S. W. (2000) Relaxation in glass forming liquids and amorphous solids. Journal of Applied Physics. 88. 3113-3157. 10.1063/1.1286035.

[19] Tanaka, H. (2003) Relation between thermodynamics and kinetics of glass-forming Liquids. Physical Review Letters. 90. 055701. 10.1103/physrevlett.90.055701.

[20] Böhmer, R. & Ngai, K. L. & Angell, C. A. & Plazek, D. J. (1993) Non-exponential relaxations in strong and fragile glass-formers. The Journal of Chemical Physics. 99. 4201-4209. 10.1063/1.466117.

[21] Perera, D. N. (1999) Compilation of the fragility parameters for several glass-forming metallic alloys. Journal of Physics: Condensed Matter. 11. 3807. 10.1088/0953-8984/11/19/303.

[22] Brüning, R. & Samwer, K. (1992) Glass transition on long time scales. Physical Review B, Condensed Matter. 46. 11318-11322. 10.1103/physrevb.46.11318.

[23] Novikov, V. N. & Sokolov, A. P. (2004) Poisson's ratio and the fragility of glass-forming liquids. Nature. 431. 961-3. 10.1038/nature02947.

[24] Dyre, J. C. (2006) Colloquium: The glass transition and elastic models of glass-forming liquids. Reviews of Modern Physics. 78. 953-972. 10.1103/revmodphys.78.953.

[25] Jiang, M. & Dai, L. (2007) Intrinsic correlation between fragility and bulk modulus in metallic glasses. Physical Review B. 76. 10.1103/physrevb.76.054204.

[26] Wang, W. H. & Wang, R. J. & Li, F. Y. & Zhao, D. Q. & Pan, M. X. (1999) Elastic constants and their pressure dependence of Zr41Ti14Cu12.5Ni9Be22.5C1 bulk metallic glass. Applied Physics Letters. 74. 1803 - 1805. 10.1063/1.123091.

[27] Wang, W. H. (2005) Elastic moduli and behaviors of metallic glasses. Journal of Non-crystalline Solids. 351. 1481-1485. 10.1016/j.jnoncrysol.2005.03.024.

[28] Wang, W. H. (2006) Correlations between elastic moduli and properties in bulk metallic glasses. Journal of Applied Physics. 99. 093506-093506. 10.1063/1.2193060.

[29] Rezvan, A. & Sarac, B. & Soprunyuk, V & Kim, J. T. & Song, K. K. & Li, C. J. & Schranz, W. & Eckert, J. (2020) Influence of combinatorial annealing and plastic deformation treatments on the intrinsic properties of Cu46Zr46Al8 bulk metallic glass. Intermetallics 127, 106986.

[30] Kunzi, H. U. Top Appl Phys 1983;53:169.

[31] Wang, W. H. & Bai, H. Y. & Luo, J. L. & Wang, R. J. & Jin, D. (2000) Supersoftening of transverse phonons in Zr41Ti14Cu12.5Ni10Be22.5 bulk metallic glass. Physical Review B. 62. 25-28. 10.1103/physrevb.62.25.

[32] Johnson, W. L. & Samwer, K. (2005) A universal criterion for plastic yielding of metallic glasses with a (T/Tg)2/3 temperature dependence. Physical Review Letters. 95. 195501. 10.1103/physrevlett.95.195501.

[33] Johnson, W. L. & Demetriou, M. D. & Harmon, J. S. & Lind, M. L. & Samwer, K. (2007) Rheology and ultrasonic properties of metallic glass-forming liquids: A potential energy landscape perspective. MRS Bulletin. 32. 10.1557/mrs2007.127.

[34] Demetriou, M. D. & Harmon, J. S. & Tao, M. & Duan, G. & Samwer, K. & Johnson, W. L. (2006) Cooperative shear model for the rheology of glass-forming metallic liquids. Physical Review Letters. 97. 065502. 10.1103/physrevlett.97.065502.

[35] Dyre, J. C. & Olsen, N. B. & Christensen, T. (1996) Local expansion model for viscous-flow activation energies of glass-forming molecular liquids. Physical Review. B, Condensed Matter. 53. 2171-2174. 10.1103/physrevb.53.2171.

[36] Granato, A. V. (1992) Interstitialcy model for condensed matter states of face-centered-cubic metals. Physical Review Letters. 68. 974-977. 10.1103/physrevlett.68.974.

[37] Granato, A. V. (1994) Self-interstitials as basic structural units of liquids and glasses. Journal of Physics and Chemistry of Solids. 55. 931-939. 10.1016/0022-3697(94)90112-0.

[38] Polk, D. E. & Turnbull, D. (1972) Flow of melt and glass forms of metallic alloys. Acta Metallurgica. 20. 493-498. 10.1016/0001-6160(72)90004-1.

[39] Doolittle, A. K. (1952) Studies in newtonian flow. II. The dependence of the viscosity of liquids on free-space. Journal of Applied Physics. 22. 1471 - 1475. 10.1063/1.1699894.

[40] Adam, G. & Gibbs, J. H. (1965) On temperature dependence of cooperative relaxation properties in glass-forming liquids. Chemical Physics. 43. 139-146. 10.1063/1.1696442.

[41] Greer, A. & Cheng, Y. Q. & Ma, E. (2013) Shear bands in metallic glasses. Materials Science and Engineering: R: Reports. 74. 71-132. 10.1016/j.mser.2013.04.001.

[42] Schuh, C. A. & Lund, A. C. (2003) Atomistic basis for the plastic yield criterion of metallic glass. Nature materials. 2. 449-52. 10.1038/nmat918.

[43] Argon, A. S. & Kuo, H. Y. (1979) Plastic flow in a disordered bubble raft (an analog of a metallic glass). Materials Science and Engineering. 39. 101-109. 10.1016/0025-5416(79)90174-5.

[44] Heilmaier, M. & Eckert, J. (2005) Elevated temperature deformation behavior of Zr-based bulk metallic glasses. Advanced Engineering Materials. 7. 833 - 841. 10.1002/adem.200500080.

[45] Sarac, B. & Bera, S. & Balakin, S. & Stoica, M. & Calin, M. & Eckert, J. (2017) Hierarchical surface patterning of Ni- and Be-free Ti- and Zr-based bulk metallic glasses by thermoplastic net-shaping, Materials Science and Engineering, C 73 398–405.

[46] Sarac, B. & Bera, S. & Spieckermann, F. & Balakin, S. & Stoica, M. & Calin, M. & Eckert, J. (2017) Micropatterning kinetics of different glass-forming systems investigated by thermoplastic net-shaping, Scripta Materialia. 137 127–131.

[47] Bera, S. & Sarac, B. & Balakin, S. & Ramasamy, P. & Stoica, M. & Calin, M. & Eckert, J. (2017). Micro-patterning by thermoplastic forming of Ni-free Ti-based bulk metallic glasses. Materials & Design. 120. 10.1016/j.matdes.2017.01.080.

[48] Altounian, Z. & Guo-hua, T. & Strom-Olsen, J. O. (1982) Crystallization characteristics of Cu-Zr metallic glasses from Cu70Zr30 to Cu25Zr75. Journal of Applied Physics. 53. 4755 - 4760. 10.1063/1.331304.

[49] Buschow, K. H. J. (1981) Thermal stability of amorphous Zr-Cu alloys. Journal of Applied Physics. 52. 3319 - 3323. 10.1063/1.329152.

[50] Inoue, A. & Zhang, W. & Saida, J. (2004) Synthesis and fundamental properties of Cu-based bulk glassy alloys in binary and multi-component systems. Materials Transactions. 45. 10.2320/matertrans.45.1153.

[51] Greer, A. L. (2009) Metallic glasses on the threshold. Materials Today. 12. 14-22. 10.1016/S1369-7021(09)70037-9.

[52] Zhou, H. & Zhang, C. & Wang, W. & Yasir, M. & Liu, L. (2014) Microstructure and mechanical properties of Fe-based amorphous composite coatings reinforced by stainless steel powders. Journal of Materials Science & Technology. 31. 10.1016/j.jmst.2014.09.008.

[53] Nishiyama, N. & Amiya, K. & Inoue, A. (2007) Novel applications of bulk metallic glass for industrial products. Journal of Non-Crystalline Solids. 353. 3615-3621. 10.1016/j.jnoncrysol.2007.05.170.

[54] Zhang, L. & Huang, H. (2019) Micro machining of bulk metallic glasses: A Review. International Journal of Advanced Manufacturing Technology. 100. 637-661. 10.1007/s00170-018-2726-y.

[55] Krejcie, A. J. & Kapoor, S. G. & DeVor, R. E. (2012) A hybrid process for manufacturing surgical-grade knife blade cutting edges from bulk metallic glass. Journal of Manufacturing Processes. 14. 10.1016/j.jmapro.2011.09.001.

[56] Ashby, M. F. & Greer, A. L. (2006) Metallic glasses as structural materials. Scripta Materialia. 54. 321-326. 10.1016/j.scriptamat.2005.09.051.

[57] Koval, Y. N. & Firstov, G. S. & Kotko, A. V. (1992) Martensitic transformation and shape memory effect in ZrCu intermetallic compound. Scripta Metallurgica et Materialia. 27. 1611-1616. 10.1016/0956-716x(92)90153-6.

[58] Carvalho, E. M. & Harris, I. R. (1980) Constitutional and structural studies of the intermetallic phase, ZrCu. Journal of Materials Science. 15. 1224-1230. 10.1007/bf00551811.

[59] Zhalko-Titarenko, A. V. & Yevlashina, M. L. & Antonov, V. N. & Yavorskii, B. Y. & Koval, Y. N. & Firstov, G. S. (1994) Electronic and crystal structure of the ZrCu intermetallic compound close to the point of structural

transformation. Physica Status Solidi (b). 184. 121 - 127. 10.1002/pssb.2221840108.

[60] Zhou, S. H. & Napolitano, R. E. (2008) Identification of the B33 martensite phase in Cu–Zr using first-principles and X-ray diffraction. Scripta Materialia. 59. 1143-1146. 10.1016/j.scriptamat.2008.07.040.

[61] Das, J. & Tang, M. B. & Kim, K. B. & Theissmann, R. & Baier, F & Eckert, J. (2005) "Work-hardenable" ductile bulk metallic glass. Physical review letters. 94. 205501. 10.1103/physrevlett.94.205501.

[62] Xing, L. Q. & Ochin, P. & Bigot, J. (1996) Effects of Al on the glass-forming ability of Zr-Cu based alloys. Journal of Non-Crystalline Solids. s 205–207. 637–640. 10.1016/S0022-3093(96)00382-1.

[63] Wang, D. & Tan, H. & Li, Y. (2005) Multiple maxima of GFA in three adjacent eutectics in Zr–Cu–Al alloy system – A metallographic way to pinpoint the best glass forming alloys. Acta Materialia. 53. 2969-2979. 10.1016/j.actamat.2005.03.012.

[64] Manivasagam, G. & Singh, A. K. & Rajamanickam, A. & Gogia, A. (2009) Ti based biomaterials, the ultimate choice for orthopaedic implants–A review. Progress in Materials Science. 54. 397-425. 10.1016/j.pmatsci.2008.06.004.

[65] Rezvan, A & Sharifikolouei, E. & Lassnig, A. & Soprunyuk, A. & Gammer, C. & Spieckermann, F. & Schranz, W. & Najmi, Z. & Cochis, A. & Scalia, A. C. & Rimondini, L. & Manfredi, M. & Eckert, J. & Sarac, B. (2022) Antibacterial activity, cytocompatibility, and thermomechanical stability of Ti40Zr10Cu36Pd14 bulk metallic glass. Materials Today Bio 16 100378.

[66] Gautier, L. & Cazottes, S. & Véron, M. & Fabrègue, D. & Chevalier, J. (2022) Spherulitic growth process in Ti-based metallic glass: Microstructure, phase identification, and growth mechanism. Materials Characterization. 192. 112170. 10.1016/j.matchar.2022.112170.

[67] Civantos, A. & Martínez-Campos, E. & Ramos, V. & Elvira, C. & Gallardo, A. & Abarrategi, A. (2017) Titanium coatings and surface modifications: Toward

clinically sseful bioactive implants. ACS Biomaterials Science & Engineering. 3. 10.1021/acsbiomaterials.6b00604.

[68] Pelaez-Vargas, A. & Gallego-Perez, D. & Magallanes-Perdomo, M. & Fernandes, M. H. & Hansford, D. J. & De Aza, A. H. & Pena, P. & Pedtp & Monteiro, F. J. (2011) Isotropic micropatterned silica coatings on zirconia induce guided cell growth for dental implants. Dental materials: official publication of the Academy of Dental Materials. 27. 581-9. 10.1016/j.dental.2011.02.014.

[69] Rezvan, A. & Sarac, B. & Soprunyuk, V. & Spieckermann, F. & Gammer, C. & Sheng, H. & Sifferlinger, N. A. & Eckert, J. (2021) Deformation-mode-sensitive behavior of CuZr-based bulk metallic glasses under dynamic loading. Metallurgical and Materials Transactions A 52 (2021) 8-13.

Overview of publications

Paper A:

A. Rezvan, B. Sarac, V. Soprunyuk, J.T. Kim, K.K. Song, C.J. Li, W. Schranz, J. Eckert

Influence of Combinatorial Annealing and Plastic Deformation Treatments on the Intrinsic Properties of $Cu_{46}Zr_{46}Al_8$ Bulk Metallic Glass

Intermetallics, DOI: 10.1016/j.intermet.2020.106986 **(2020)**

Paper B:

A. Rezvan, B. Sarac, V. Soprunyuk, F. Spieckermann, C. Gammer, H. Sheng, N.A. Sifferlinger, J. Eckert

Deformation-Mode-Sensitive Behavior of CuZr-Based Bulk Metallic Glasses Under Dynamic Loading

Metallurgical and Materials Transactions A, DOI: 10.1007/s11661-020-06048-w **(2020)**

Paper C:

A. Rezvan, E. Sharifikolouei, A. Lassnig, V. Soprunyuk, C. Gammer, F. Spieckermann, W. Schranz, Z. Najmi, A. Cochis, A.C. Scalia, L. Rimondini, M. Manfredi, J. Eckert, B. Sarac

Antibacterial activity, Cytocompatibility, and Thermomechanical Stability of $Ti_{40}Zr_{10}Cu_{36}Pd_{14}$ Bulk Metallic Glass

Materials Today Bio, DOI: 10.1016/j.mtbio.2022.100378 **(2022)**

Paper D:

Amir Rezvan, Elham Sharifikolouei, Viktor Soprunyuk, Wilfried Schranz, Juraj Todt, Alice Lassnig, Christoph Gammer, Nikolaus August Sifferlinger, Atacan Asci, Ilya Okulov, Sandra Schlögl, Jozef Keckes, Ziba Najmi, Andrea Cochis, Alessandro Calogero Scalia, Lia Rimondini, Baran Sarac, Jürgen Eckert

$Ti_{40}Zr_{10}Cu_{36}Pd_{14}$ Bulk Metallic Glass as Oral Implant Material

(submitted), DOI: 10.2139/ssrn.4476004 **(2023)**

Influence of combinatorial annealing and plastic deformation treatments on the intrinsic properties of $Cu_{46}Zr_{46}Al_8$ bulk metallic glass

A. Rezvan [a,b], B. Sarac [a], V. Soprunyuk [a], J.T. Kim [a], K.K. Song [c], C.J. Li [d], W. Schranz [e], J. Eckert [a,b]

[a] *Erich Schmid Institute of Materials Science, Austrian Academy of Sciences (ÖAW), Jahnstraße 12, A-8700, Leoben, Austria*
[b] *Department of Materials Science, Chair of Materials Physics, Montanuniversität Leoben, Jahnstraße 12, A-8700, Leoben, Austria*
[c] *School of Mechanical, Electrical & Information Engineering, Shandong University (Weihai), Wenhua Xilu 180, 264209, Weihai, PR China*
[d] *Faculty of Materials Science and Engineering, Kunming University of Science and Technology, Kunming, 650093, PR China*
[e] *University of Vienna, Faculty of Physics, Physics of Functional Materials, Boltzmanngasse 5, A 1090, Wien, Austria*

ABSTRACT

In this paper, the effect of severe plastic deformation (SPD) induced by high-pressure torsion (HPT) and isothermal heat treatment (HT) below the glass transition on the structure-property relationships of $Cu_{46}Zr_{46}Al_8$ bulk metallic glass (BMG) is assessed separately and alternately in reference to the as-cast state. Pronounced modifications are confirmed by X-ray diffraction, differential scanning calorimetry, dynamic mechanical analysis (DMA), dilatometry analysis, and scanning electron microscopy. Diffusion-controlled crystallization is achieved via HT with optimized parameters, and HPT is used afterwards to disperse crystalline phases relatively homogenous throughout the matrix. The dispersion of the second phase improves the thermomechanical stability around the glass transition temperature, as confirmed by DMA. Compared to a single HT process, a sequential combination of HT + HPT leads to a glass showing a linear hardness profile with values higher than the as-cast state. This study provides insights into possible processing routes for enhancing the mechanical and/or

thermal properties of CuZr-based BMGs, which can also be used to tailor new design routes for other BMG systems.

1. Introduction

The defining characteristic of bulk metallic glasses (BMGs), which makes them different from conventional metallic materials, is the absence of crystallinity and the associated lack of microstructural features such as grain and phase boundaries [1]. BMGs accommodate plastic strain in highly localized shear bands owing to the absence of dislocations in their non-translational atomic order [2]. The properties of metallic glasses are size-dependent, where samples with an effective thickness exceeding 1 mm exhibit often brittle deformation [3–6]. The plasticity of metallic glasses can be enhanced by increasing the shear band density. Besides, the interaction between shear bands and second phases can stabilize the shear bands and thus impede crack formation [7–11]. Shear band confinement can change the deformation mode [9, 12,13] as long as the spacing of the second phase(s) matches the plastic zone size of the related BMG matrix [8,14]. More specifically, when the spacing of the second phase(s) is equal or smaller than the plastic zone size (RP) of the sample, shear bands will not immediately develop into cracks. But instead, the formation of multiple shear bands is triggered, and thus, energy dispersion due to stress distribution is favored [15–17]. Moreover, it has been confirmed in the literature that the plastic zone size of a variety of BMGs remains constant even at elevated temperatures (at temperatures below the glass transition temperature Tg) [18]. CuZr-based metallic glasses are known to have plastic zone sizes of approximately 50 μm [19] and, thus, uniformly dispersed nano-to micro-scale crystals should be beneficial for the enhancement of strength retention at temperatures close to the glass transition.

Unfortunately, metallic glasses in the bulk state are not in the ideal glass condition. In order to cast the largest possible BMG, the cooling rate is kept at its threshold during suction casting, which can result in inhomogeneity and

compositional segregation in the structure [20–22]. High pressure torsion (HPT) is an approach to homogenize the microstructure and thus achieve a reliable product [23–29]. This method has been considered as a suitable tool for inducing compositional homogenization in multicomponent advanced alloy systems [30]. The high extent of applied shear strain during HPT generates free volume in the structure and causes mechanical softening and structural rejuvenation [31].

For CuZrAl-BMG composites (BMGCs), through deformation, the B2- CuZr crystals embedded in the glassy matrix can transform into stress/ strain induced transformation, and thus, render the formation of multiple shear bands. This leads to superior mechanical properties of CuZr-based alloys. The desired B2 phase precipitates via a polymorphic crystallization during cooling from the melt [32]. However, the glass-forming ability (GFA) of the remaining melt often cannot then be kept high enough to form a glassy matrix with homogenously nucleated B2 crystals due to the solidification characteristics of CuZr-based alloy systems [33–35]. In this study, we used an alternative technique to fabricate BMGCs by diffusion-controlled crystallization of monolithic BMGs via sub-Tg heat treatment (HT). The adopted method consists of two steps: casting fully glassy BMGs, and subsequent HT. It has been confirmed in the literature that processing below Tg for some BMG types might lead to early fracture due to thermal embrittlement [11,36–38], which can succeed by nanocrystallization [33,39–43] or devitrification [44,45]. HT reduces the amount of free volume in the matrix and triggers structural relaxation [31]. Such treatment has been shown to generate temperature-dependent crystallization on different length-scales depending on the processing conditions [46]. We provide insight into how HPT and HT influence the (thermo)mechanical, thermal, and structural properties of $Cu_{46}Zr_{46}Al_8$ BMGs.

2. Experimental

2.1. Casting of CuZrAl-Bulk metallic glass (BMG)

In the first step, a $Cu_{46}Zr_{46}Al_8$ master alloy was synthesized using an Edmund Buehler AM0.5 arc melting system operated under a Ti-gettered argon atmosphere. The industrial-grade alloy constituents of 99.9% purity were weighed with an accuracy of ± 0.001 g. During melting, the melting current went up to a maximum of 150 A. To homogenize the ingot thoroughly, the melting was repeated four times. The alloy was cast afterwards into a copper mold with a circular plate geometry of 40 mm in diameter and 2 mm in thickness. Rotary and diffusion pumps were used to evacuate the system down to 10^{-6} mbar. The pressure difference required for suction between the designed mold cavity and the working chamber was controlled by purging argon.

2.2. High pressure torsion (HPT)

From the 40 mm diameter cast plate 8 mm diameter discs were cut using a custom-built electro-discharge machine. This method has been proven to not influence the amorphous state of the CuZr-based BMGs. The discs were ground down in equal thicknesses from both sides to a thickness of 1.00 ± 0.02 mm and then deformed separately between two anvils after sandblasting. The top anvil was fixed to hydrostatic compressive stress, while the bottom one was rotated to impose torsion onto the discs. The anvils had a cylindrical cavity which allowed central positioning of the samples and the pressure to be hydrostatic. The HPT tests were conducted with a load of 7.8 GPa and a rotation speed of 0.6 min^{-1}. Anvils with cylindrical cavities of 8 mm and a depth of 0.15 mm were used. The applied shear strain at the center of the disc is nearly zero and increases along the radius towards the edge. In order to find an optimized number of turns, a series of HPT tests were performed with a different number of rotations to check how the number of rotations may affect the hardness. The HPTed samples were embedded and polished for hardness testing. Microindentation tests were

conducted along the diameter of the discs. Observing no considerable changes in the hardness with an increasing number of turns beyond 30 indicated that hardness saturation was attained. Comparing the results with the hardness values for CuZr-based glasses in the literature led us set 30 turns for the series of HPT tests [30], by which saturation of HPT-induced dilatation (i.e., creation of free volume) was reached. Despite the already known local temperature rise effect during HPT, the induced modifications in the structure of the glass after HPT are mainly ascribed to a high extent of applied shear strain that overcomes thermal effects.

2.3. Heat treatment (HT)

The annealing temperature was optimized on the HT + HPT samples. Four samples were annealed isothermally for 15 min at four different temperatures: 623, 653, 683, and 713 K. In the furnace, the heating rate of 50 K/min was employed to reach the destination temperatures. Temperature stabilization was achieved by 10 min of waiting time prior to sample insertion. Uniform heating is present within the furnace, where the same temperature in multiple positions on the sample was confirmed by the thermocouple readings. The accuracy of the heating unit of the furnace was within ± 1K. The specimens were immediately water quenched afterwards to room temperature to avoid post-crystallization effects. The heat-treated samples were subsequently HPTed, as described in the previous subsection. The samples were ground and polished in equal thicknesses from both sides down to 0.3 mm. The samples were investigated by X-ray diffraction (XRD) using a Bruker D2Phaser diffractometer with Co Kα radiation ($\lambda = 1.7902$ Å) using a step size of 0.02. Differential scanning calorimetry (DSC) tests were conducted with a Mettler Toledo DSC 3+ under an argon atmosphere at a constant heating rate of 10 K/min. Pieces at larger radius were cut from the discs using a wire saw. The weight of the specimens was 10 ± 0.5 g. The samples were heated twice in the DSC, and normalization was done by subtracting the

baseline from the original heating curve. The cooling rate between two heating periods was selected as 50 K/min to minimize the influence of the time spent for cooling on the overall DSC data. All the DSC tests were repeated 3 times, an error of ± 2K for the glass transition and crystallization temperatures and an error of 10% were determined for the crystallization enthalpy values.

2.4. Post-characterization methods

Five final samples are investigated in this paper (i.e., as-cast, just HPTed, just HTed, HPT + HT, and HT + HPT). Microhardness testing was performed using a Buehler Micromet 5104. Hardness values were obtained at each distance from the center along two perpendicular diagonals of the embedded discs. The Vickers hardness was calculated by the applied force divided by the surface area of the indent. Thereby, the hardness was measured by the diagonal indents from 4 different points and averaged. All the tests were repeated 4 times, and an error of 3% was determined for the hardness measurements. Dynamic mechanical analysis (DMA) was conducted employing a constant heating rate of 10 K/ min using a Discovery HR-3 device (TA Instruments). The viscosity was subsequently calculated via Stefan's equation [47,48]. The chamber was purged with N2 gas continuously upon heating and cooling. 10 N force was applied (25% static, 75% dynamic load), and a single frequency of one cycle per second (1 Hz) was used. The samples were heated from room temperature to 850 K. The experiments were performed in displacement-control mode with 5 μm displacement at each sinusoidal loading interval. Thermal expansion/contraction was measured using a dilatometer (parallel plate rheometer) under a constant load of 50 mN. The samples were heated from 300 K to 850 K at a heating rate of 10 K/min. The evolution of structural modifications of the differently treated samples was investigated in a field emission gun scanning electron microscope (FEGSEM – Zeiss LEO1525) with a Schottky emitter. The acceleration voltage was selected as 20 kV. The system vacuum was 10^{-4} mbar. A four-quadrant

backscatter detector was utilized to determine the phase contrast of the crystals. SEM was performed on the cross-section of the samples.

3. Results and Discussion

3.1. Selection of process parameters

According to preliminary studies of the corresponding samples by XRD and DSC (Fig. 1), modifications first appear for samples annealed at 683 K, where crystalline diffraction peaks corresponding to the cubic primitive B2-CuZr (Pm-3m) phase are superimposed on the broad amorphous maxima. The crystalline peaks on top of the broad diffuse maxima of the 713 K sample are sharper in comparison and can be allocated to the same crystalline structure consisting of B2-CuZr [34]. The onset of remarkable crystallization was also confirmed by DSC. Based on the findings, the annealing temperature was set as 683 K. Samples annealed at 713 K were crystallized beyond the diffusion-controlled crystallization aimed for in this study. The double peak of crystallization visible in the DSC scan (cf. inset in Fig. 1(b)) is due to compositional segregation [49,50].

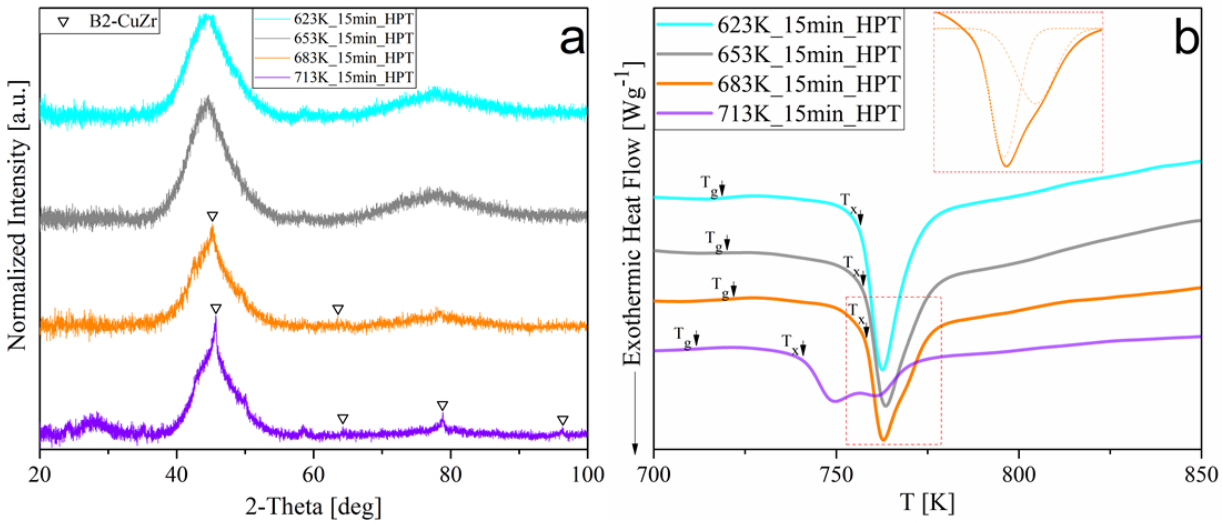

Fig. 1. (a) XRD patterns of the HPT deformed samples with different pre-annealing protocols. (b) DSC data (heating rate 10 K/min) of the HPTed samples with different pre-annealing treatments; the crystallization event of the 683K-15min-HT + HPT samples deconvoluted into two main peaks is presented in the inset.

3.2. Structural and thermal characterization

Based on the X-ray diffraction (XRD) results (Fig. 2), the as-cast and HPT samples are fully amorphous. For the HT sample, crystalline diffraction peaks corresponding to B2-CuZr crystals are superimposed on the broad amorphous maxima. Crystalline peaks emerge on the broad diffraction patterns of the two-stage treated samples, and these peaks indicate similar precipitation of the B2-CuZr phase.

The differential scanning calorimetry (DSC) results are shown in Fig. 3. The width of the supercooled liquid region (SCLR) $\Delta T_x = T_x - T_g$, determined by the difference between crystallization temperature and glass transition temperature, decreases marginally from 38 K for the as-cast sample to 35 K for the HPT sample due to the slight shift of Tg to a higher temperature, in line with findings in the literature [31]. The width of the SCLR is a parameter to reflect the formability of BMGs of similar chemical composition [51]. T_x drops slightly after HT from 757 K to 753 K. For HPT + HT, ΔT_x becomes marginally larger (39 K) with a shift of T_g to a lower temperature compared to the HPT sample, revealing that the effect of HPT is partially mitigated by the post-annealing. For the HPT + HT and HT + HPT samples, T_x and T_g also show some minor changes. Most noticeable change is the broadening of the crystallization peak by the development of a shoulder. This goes along with a rise in crystallization enthalpy (ΔH_x). The exothermic peaks in the continuous DSC curves of CuZr-based metallic glasses, regardless of the Al content, correspond to the transformation of the glass to B2-CuZr [52,53].

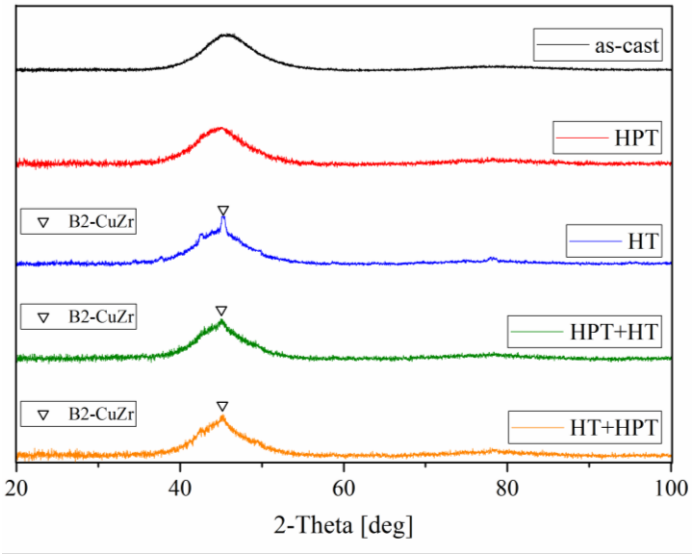

Fig. 2. XRD measurements of the five final samples (i.e., as-cast, only HPTed, only HTed, HPT + HT, and HT + HPT). The diffraction patterns delineate the evolution of B2 upon HT, HPT + HT, and HT + HPT.

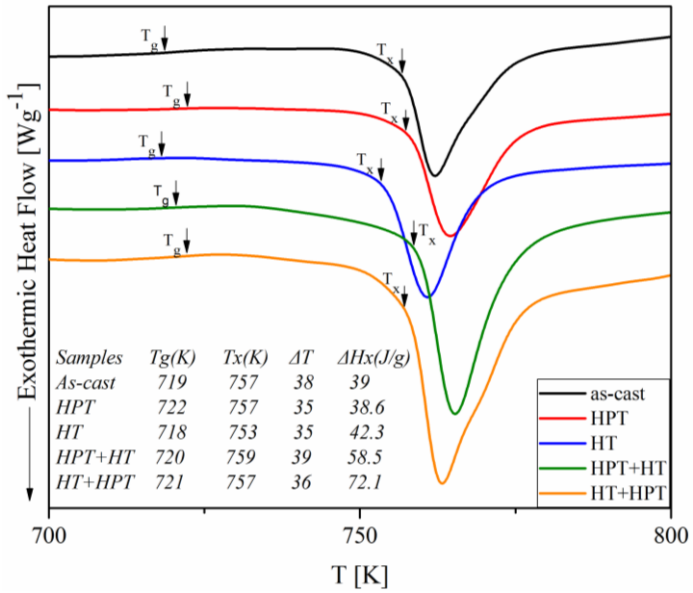

Fig. 3. DSC data (heating rate 10 K/min) of the different samples (i.e., as-cast, HPTed, HTed, HPT + HT, and HT + HPT) together with characteristic values.

3.3. Microhardness testing

Fig. 4 shows the microhardness profiles of the differently treated samples (i.e., as-cast, HPT, HT, HPT + HT, and HT + HPT). The variation in hardness acquired from the as-cast sample can probably be ascribed to accumulated residual stresses or locally different degrees of relaxation associated with the cooling rate gradient

during casting [54–59]. Tremendous softening due to volumetric dilatation is observed for the HPTed samples from the center to the edge of the disc, as the applied shear strain and plastic flow induced by HPT increase with the radius [25]. A substantial hardness increase is observed after heat treatment. Regarding the viscosity, CuZr-based alloy systems show a deviation from Arrhenius behavior at sub-Tg temperatures, and even short-time sub-Tg annealing can cause structural reordering or phase decomposition [40, 44]. Compared to the as-cast sample, HPT leads to an average hardness decrease by ~16 HV, whereas HT leads to an average hardness increase of ~24 HV (Table 1). For the HT sample, this increase in hardness can be linked to the structural relaxation of the glassy matrix. The average hardness value for the HPT + HT sample is lower than that of the HT + HPT sample. Furthermore, the HT + HPT sample exhibits an even hardness profile along the radius, revealing that the behavior of the HT + HPT sample is influenced by HT rather than HPT. In contrast, for the HPT + HT sample, the effect of HPT is stronger, i.e., the degree of softening increases continuously from the center towards the edge of the disc due to more pronounced straining.

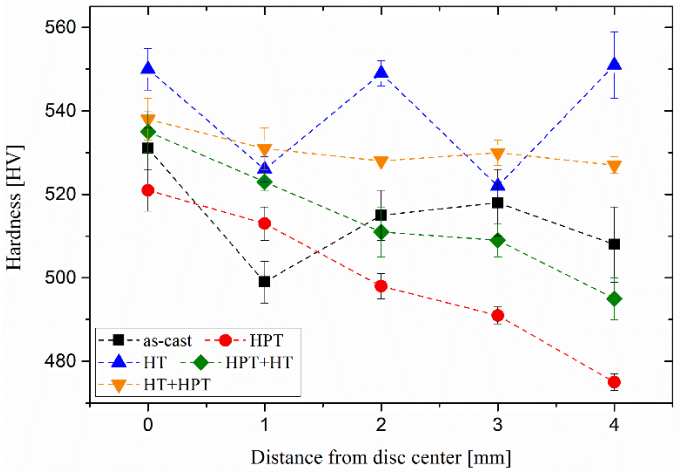

Fig. 4. Comparison of the microhardness profiles as a function of the distance from the disc center for the differently treated samples, where the Vickers hardness was measured with a load of 1000 g.

Table 1
Average Vickers hardness values together with the standard deviation of the measurements.

As-cast	HPT	HT	HPT+HT	HT+HPT
515 ± 14	499 ± 18	539 ± 16	514 ± 15	531 ± 4

3.4. Dynamic mechanical and Dilatometry analyses

Fig. 5 illustrates the dynamic mechanical analysis (DMA) results of the 5 differently treated samples investigated under 3-point bending (TPB). The as-cast sample shows an increase in storage modulus (E′) from 88 ± 1 GPa to 105 ± 1 GPa as the material enters the α relaxation region. The change in the slopes below Tg is accounted for the different relaxation modes of the differently treated samples. The HPT treatment leads to a significant drop in E′ (from 88 ± 1 GPa to 72 ± 1 GPa) within the α relaxation region, as expected due to rejuvenation. On the contrary, the heat treatment leads to a shift of the hump observed for the as-cast sample towards higher temperatures, indicating the annihilation of free volume. The most amount of relaxation occurs for the as-cast state, followed by the HT samples. On the other hand, the HPT and two-stage treated samples do not show any relaxation phenomenon upon heating. Stiffening owing to previous relaxation, i.e., an increase of the elastic modulus, is observed for the HT sample at the onset of the glass transition. The HPT + HT sample displays a similar behavior as the only-HPTed sample with a gradual decrease in E′ at temperatures above 600 K as it enters the structural relaxation region. The vice-versa treatment, i.e., HT + HPT, leads to a more stabilized E′ up to 700 K. Thus, the HT + HPT treatment causes an increase in the thermomechanical stability by ~100 K. Different from DMA tests performed under torsion or tension, the complex stress state generated by 3-point bending can be the reason for the minor hump in tanδ before the main crystallization takes place. The corresponding dilatometer measurements are illustrated in the inset of Fig. 5. The influence of HPT (red curve) on the structural relaxation region, observed by DMA, is also reflected in

these static measurements. A pronounced thermal contraction is observed for the HPT sample at temperatures up to 710 K owing to the change in viscosity. On the contrary, no stiffening effect is observed for the HT and as-cast samples, pointing out that the static mode type of measurement is less sensitive to structural changes around the glass transition. A slight increase in the slope due to the thermal expansion of the as-cast and HT samples is observed up to 700 K close to T_g. Compared to the as-cast state, heat treatment leads to a larger drop in viscosity in the supercooled liquid region, as confirmed by both measurements.

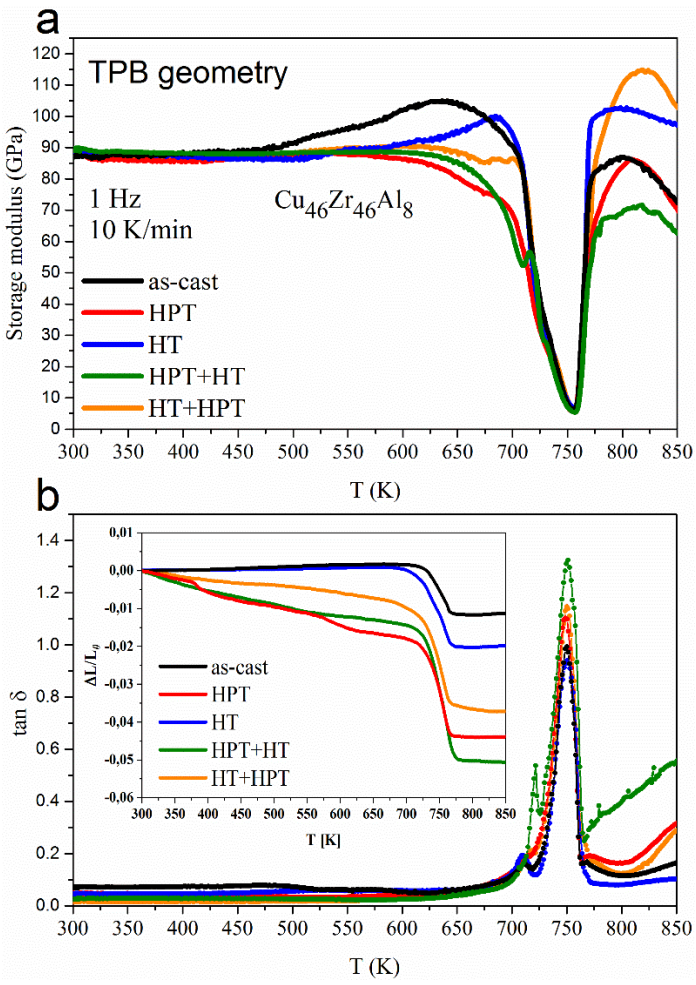

Fig. 5. DMA analysis (heating rate 10 K/min) of the different samples; (a) storage modulus E′ and (b) loss factor tanδ curves as a function of temperature. Thermal expansion data of the as-cast, HPT, HT, HPT + HT, and HT + HPT samples obtained at the same heating rate are shown in the b-inset.

3.4. Microstructural investigations

Characteristic scanning electron microscopy (SEM) images of the as-cast, HPT, HT, HPT + HT, and HT + HPT samples are shown in Fig. 6 a-e. Neither crystals nor any features (i.e., voids, shear bands, or dendritic second phases) are observed throughout the volume of the as-cast sample (Fig. 6 a), which corroborates the amorphous state of the as-cast BMG on the micro-scale. The HPT sample is also amorphous (Fig. 6 b). Besides, shear bands (indicated by red arrows) are developed due to the severe deformation during the HPT process; the spacing between them is ~1 μm or less. In the matrix of the HT sample, crystals (on the order of 1 μm and below) are formed during annealing (Fig. 6 c). On the other hand, the distribution of the second phase upon sole HT on the cast BMG might not be homogeneous, as regions might have a different inclination towards crystal nucleation and growth due to the heterogeneities. For the HPT + HT sample, the crystals are rather homogenously dispersed (Fig. 6 d). HPT can homogenize the microstructure, after which HT nuclei can form and immediately grow, different than the HT on the as-cast BMG, in which possible structural heterogeneities are hardly conducive to interdiffusion of atoms. By comparing the HPT + HT sample to the just-HT specimen, it can also be concluded that HPT again generates a large number of shear bands, where the nanocrystals generally form in the vicinity of these shear bands. In the HT + HPT sample, the crystals (on the order of 100 nm) are relatively homogenously dispersed (Fig. 6 e).

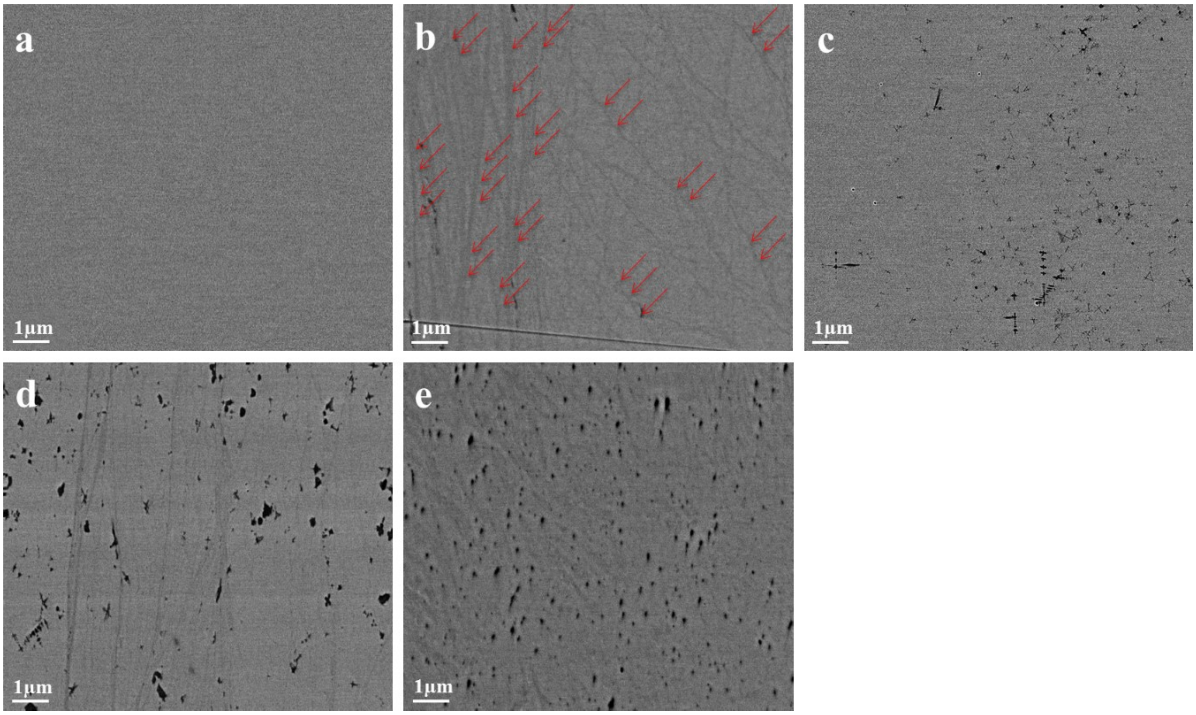

Fig. 6. SEM micrographs of the corresponding samples (a-e). (a) as-cast: amorphous, neither crystal nor any features; (b) HPT: amorphous, shear bands developed; (c) HT: irregular & round-form crystals; (d) HPT + HT:; (e) HT + HPT: round crystals dispersed relatively homogenously.

4. Conclusion

This paper elucidates the changes in the (thermo)mechanical, thermal and structural properties of the $Cu_{46}Zr_{46}Al_8$ bulk metallic glass (BMG) upon sub-Tg heat treatment (HT) and severe plastic deformation (SPD). Casting a 40 mm diameter and 2 mm thick plate of this composition generates a fully glassy BMG, as confirmed by X-ray diffraction. High pressure torsion (HPT) processing does not induce crystallization but changes the thermophysical properties slightly by increasing T_g. At the early stage of sub-T_g annealing, the metastable B2-CuZr phase in nano-to micrometer-scale precipitates. Due to the multi-axial stress state, HPT on its own can cause the intersection of shear bands, as confirmed by SEM, which probably creates nucleation sites in the amorphous matrix. This phenomenon eventually renders the formation of HT-induced nanocrystals over the glassy matrix. By taking an alternate order of the treatments, i.e., first HT followed by HPT, a uniform distribution of the crystals can be achieved.

Compared to the as-cast sample, an even hardness profile with a relatively higher Vickers hardness across the BMG specimen can be achieved by controlled HPT of the HTed sample. According to DMA analysis, the HT + HPT BMG is thermomechanically more stable, and pronounced high strength retention was registered. In conclusion, a combinatorial treatment of annealing and plastic deformation can be a promising approach to generate metallic glasses with specifically tuned properties.

CRediT authorship contribution statement

A. Rezvan: Methodology, Investigation, Writing - original draft. B. Sarac: Supervision, Conceptualization, Writing - review & editing. V. Soprunyuk: Investigation, Data curation, Writing - review & editing. J. T. Kim: Investigation, Data curation, Writing - review & editing. K.K. Song: Writing - review & editing. C.J. Li: Writing - review & editing. W. Schranz: Resources. J. Eckert: Supervision, Writing - review & editing, Funding acquisition.

Declaration of competing interest

The authors declare that they have no known competing financial interests or personal relationships that could have appeared to influence the work reported in this paper.

Acknowledgments

The authors would like to thank S. Ketov and V. Zadorozhnyy for fruitful discussions and F. Spieckermann for his assistance with the DSC experiments. This work was supported by the European Research Council under the Advanced Grant “INTELHYB – Next Generation of Complex Metallic Materials in Intelligent Hybrid Structures” (Grant No: ERC-2013-ADG-340025).

References

[1] M. Telford, The case for bulk metallic glass, Mater. Today 7 (2004) 36–43.

[2] A.L. Greer, Y.Q. Cheng, E. Ma, Shear bands in metallic glasses, Mater. Sci. Eng. R 74 (2013) 71–132.

[3] J. Schroers, W.L. Johnson, Ductile bulk metallic glass, Phys. Rev. Lett. 93 (2004) 255506.

[4] Y.H. Liu, G. Wang, R.J. Wang, D.Q. Zhao, M.X. Pan, W.H. Wang, Super plastic bulk metallic glasses at room temperature, Science 315 (2007) 1385–1388.

[5] W.M. Yang, H.S. Liu, Y.C. Zhao, A. Inoue, K.M. Jiang, J.T. Huo, H.B. Ling, Q. Li, B. L. Shen, Mechanical properties and structural features of novel Fe-based bulk metallic glasses with unprecedented plasticity, Sci. Rep. 4 (2014) 1–6.

[6] K.F. Yao, F. Ruan, Y.Q. Yang, N. Chen, Superductile bulk metallic glass, Appl. Phys. Lett. 88 (2006) 122106.

[7] T. Wada, A. Inoue, A.L. Greer, Enhancement of room-temperature plasticity in a bulk metallic glass by finely dispersed porosity, Appl. Phys. Lett. 86 (2005).

[8] D.C. Hofmann, J.Y. Suh, A. Wiest, G. Duan, M.L. Lind, M.D. Demetriou, W. L. Johnson, Designing metallic glass matrix composites with high toughness and tensile ductility, Nature 451 (2008) 1085–1090.

[9] C.A. Volkert, A. Donohue, F. Spaepen, Effect of sample size on deformation in amorphous metals, J. Appl. Phys. 103 (2008), 083539.

[10] B. Sarac, J. Schroers, Designing tensile ductility in metallic glasses, Nat. Commun. 4 (2013) 2158.

[11] B. Sarac, J. Ketkaew, D.O. Popnoe, J. Schroers, Honeycomb structures of bulk metallic glasses, Adv. Funct. Mater. 22 (2012) 3161–3169.

[12] C.A. Schuh, A.C. Lund, T.G. Nieh, New regime of homogeneous flow in the deformation map of metallic glasses: elevated temperature nanoindentation experiments and mechanistic modeling, Acta Mater. 52 (2004) 5879–5891.

[13] H. Guo, P.F. Yan, Y.B. Wang, J. Tan, Z.F. Zhang, M.L. Sui, E. Ma, Tensile ductility and necking of metallic glass, Nat. Mater. 6 (2007) 735–739.

[14] J.J. Lewandowski, W.H. Wang, A.L. Greer, Intrinsic plasticity or brittleness of metallic glasses, Phil. Mag. Lett. 85 (2005) 77–87.
[15] C.C. Hays, C.P. Kim, W.L. Johnson, Microstructure controlled shear band pattern formation and enhanced plasticity of bulk metallic glasses containing in situ formed ductile phase dendrite dispersions, Phys. Rev. Lett. 84 (2000) 2901–2904.
[16] G. He, J. Eckert, W. Löser, L. Schultz, Novel Ti-base nanostructure-dendrite composite with enhanced plasticity, Nat. Mater. 2 (2003) 33–37.
[17] G. He, J. Eckert, W. Löser, M. Hagiwara, Composition dependence of the microstructure and the mechanical properties of nano/ultrafine-structured Ti-Cu-Ni-Sn-Nb alloys, Acta Mater. 52 (2004) 3035–3046.
[18] K.E. Prasad, U. Ramamurty, Effect of temperature on the plastic zone size and the shear band density in a bulk metallic glass, Mater. Sci. Eng., A 535 (2012) 48–52.
[19] X.K. Xi, D.Q. Zhao, M.X. Pan, W.H. Wang, Y. Wu, J.J. Lewandowski, Fracture of brittle metallic glasses: brittleness or plasticity, Phys. Rev. Lett. 94 (2005) 125510.
[20] C.Y. Tang, Y.Y. Li, W.C. Pan, Y. Du, X. Xiong, Q. Zhou, J. Wang, H.Y. Zhou, Investigation of glass forming ability in Ce-Al-Ni alloys, J. Non-Cryst. Solids 358 (2012) 1368–1373.
[21] S. Matsumoto, T. Tokunaga, H. Ohtani, M. Hasebe, Thermodynamic analysis of the phase equilibria of the Nb-Ni-Ti system, Mater. Trans. 46 (2005) 2920–2930.
[22] T. Tokunaga, H. Ohtani, M. Hasebe, Thermodynamic evaluation of the phase equilibria and glass-forming ability of the Fe-Si-B system, Calphad 28 (2004) 354–362.
[23] C. Mangler, C. Rentenberger, I. Humer, L. Reichhart, H.P. Karnthaler, Disordering and reordering of bulk Fe-45at.%Al studied by TEM, Microsc, Microanal 13 (2007) 298–299.

[24] R. Pippan, S. Scheriau, A. Hohenwarter, M. Hafok, Advantages and limitations of HPT: a review, Mater. Sci. Forum 584–586 (2008) 16–21.
[25] W. Dmowski, Y. Yokoyama, A. Chuang, Y. Ren, M. Umemoto, K. Tsuchiya, A. Inoue, T. Egami, Structural rejuvenation in a bulk metallic glass induced by severe plastic deformation, Acta Mater. 58 (2010) 429–438.
[26] J. Qiang, K. Tsuchiya, Composition dependence of mechanically-induced structural rejuvenation in Zr-Cu-Al-Ni metallic glasses, J. Alloys Compd. 712 (2017) 250–255.
[27] A. Bachmaier, R. Pippan, High-pressure torsion deformation induced phase transformations and formations: new material combinations and advanced properties, Mater. Trans. 60 (2019) 1256–1269.
[28] A. Hohenwarter, Incremental high pressure torsion as a novel severe plastic deformation process: processing features and application to copper, Mater. Sci. Eng., A 626 (2015) 80–85.
[29] O. Renk, R. Pippan, Saturation of grain refinement during severe plastic deformation of single phase materials: reconsiderations, current status and open questions, Mater. Trans. 60 (2019) 1270–1282.
[30] L. Krämer, K.S. Kormout, D. Setman, Y. Champion, R. Pippan, Production of bulk metallic glasses by severe plastic deformation, Metals 5 (2015) 720–729.
[31] B. Sarac, F. Spieckermann, A. Rezvan, C. Gammer, L. Krämer, J.T. Kim, J. Keckes, R. Pippan, J. Eckert, Annealing-assisted high-pressure torsion in Zr55Cu30Al10Ni5 metallic glass, J. Alloys Compd. 784 (2019) 1323–1333.
[32] S. Pauly, G. Liu, G. Wang, U. Kühn, N. Mattern, J. Eckert, Microstructural heterogeneities governing the deformation of Cu47.5Zr47.5Al5 bulk metallic glass composites, Acta Mater. 57 (2009) 5445–5453.
[33] R. Wei, X.L. Wang, S. Yang, F. Jiang, L. He, Formation of CuZr-based bulk metallic glass composites containing nanometer-scale B2-CuZr phase through sub-Tg annealing, J. Alloys Compd. 617 (2014) 699–706.

[34] H. Kozachkov, J. Kolodziejska, W.L. Johnson, D.C. Hofmann, Effect of cooling rate on the volume fraction of B2 phases in a CuZrAlCo metallic glass matrix composite, Intermetallics 39 (2013) 89–93.
[35] R. Wei, S. Yang, Y. Chang, Y.F. Li, C.J. Zhang, L. He, Mechanical property degradation of a CuZr-based bulk metallic glass composite induced by sub-Tg annealing, Mater. Des. 56 (2014) 128–138.
[36] G. Kumar, D. Rector, R.D. Conner, J. Schroers, Embrittlement of Zr-based bulk metallic glasses, Acta Mater. 57 (2009) 3572–3583.
[37] K. Hajlaoui, T. Benameur, G. Vaughan, A.R. Yavari, Thermal expansion and indentation-induced free volume in Zr-based metallic glasses measured by real-time diffraction using synchrotron radiation, Scripta Mater. 51 (2004) 843–848.
[38] P. Murali, U. Ramamurty, Embrittlement of a bulk metallic glass due to sub-T-g annealing, Acta Mater. 53 (2005) 1467–1478.
[39] B. Sarac, A. Bernasconi, J. Wright, M. Stoica, F. Spieckermann, M. Mühlbacher, J. Keckes, X. Bian, G. Wang, J. Eckert, Structural modifications in sub-Tg annealed CuZr-based metallic glass Mater, Sci. Eng., A 707 (2017) 245–252.
[40] B. Sarac, L. Zhang, K. Kosiba, S. Pauly, M. Stoica, J. Eckert, Towards the better: intrinsic property amelioration in bulk metallic glasses, Sci. Rep. 6 (2016) 27271.
[41] M. Song, X.Z. Liao, Y.H. He, Effect of sub-T-g annealing on the mechanical properties of a ZrAlNiCuNb bulk metallic glass, Phil. Mag. Lett. 91 (2011) 713–723.
[42] S. Venkataraman, H. Hermann, D.J. Sordelet, J. Eckert, Influence of sub-T-g annealing on the crystallization kinetics of Cu47Ti33Zr11Ni8Si1 metallic glass, J. Appl. Phys. 104 (2008).

[43] J.H. Perepezko, R.J. Hebert, W.S. Tong, J. Hamann, H.R. Rösner, G. Wilde, Nanocrystallization reactions in amorphous aluminum alloys, Mater. Trans. 44 (2003) 1982–1992.
[44] N. Van Steenberge, A. Concustell, J. Sort, J. Das, N. Mattern, A. Gebert, S. Suriñach, J. Eckert, M.D. Baró, Microstructural inhomogeneities introduced in a Zr-based bulk metallic glass upon low-temperature annealing, Mater. Sci. Eng., A 491 (2008) 124–130.
[45] N. Chen, K.F. Yao, F. Ruan, Microstructural features of phase transformation in a binary Pd-Si metallic glass, Phil. Mag. Lett. 87 (2007) 677–686.
[46] J. Schroers, Y. Wu, R. Busch, W.L. Johnson, Transition from nucleation controlled to growth controlled crystallization in Pd43Ni10Cu27P20 melts, Acta Mater. 49 (2001) 2773–2781.
[47] M.J. Stefan, Sitzber. Akad. Wiss. Wien. (Abt. II Math. Phys.) (1874) 713–735.
[48] G.J. Diennes, H.F. Klemm, Theory and Application of the parallel plate plastometer, J. Appl. Phys. 17 (1946) 458–471.
[49] B. Sarac, C. Gammer, L. Deng, E. Park, Y. Yokoyama, M. Stoica, J. Eckert, Elastostatic reversibility in thermally formed bulk metallic glasses: nanobeam diffraction fluctuation electron microscopy, Nanoscale 10 (2018) 1081–1089.
[50] J.C. Qiao, J.M. Pelletier, Isochronal and isothermal crystallization in Zr55Cu30Ni5 Al-10 bulk metallic glass, Trans. Nonferrous Metals Soc. China 22 (2012) 577–584.
[51] J. Schroers, On the formability of bulk metallic glass in its supercooled liquid state, Acta Mater. 56 (2008) 471–478.
[52] S. Pauly, J. Das, N. Mattern, D.H. Kim, J. Eckert, Phase formation and thermal stability in Cu-Zr-Ti(Al) metallic glasses, Intermetallics 17 (2009) 453–462.

[53] I.V. Okulov, I.V. Soldatov, M.F. Sarmanova, I. Kaban, T. Gemming, K. Edström, J. Eckert, Flash Joule heating for ductilization of metallic glasses, Nat. Commun. 6 (2015).
[54] W.H. Fu, Y.J. Sun, W. Zhang, The effect of cooling rate on microstructure and mechanical properties of Zr-based bulk metallic glasses, Ann. Mater. Sci. Eng. 2013 (2013).
[55] L. Wang, H. Bei, Y.F. Gao, Z.P. Lu, T.G. Nieh, Effect of residual stresses on the hardness of bulk metallic glasses, Acta Mater. 59 (2011) 2858–2864.
[56] K.K. Song, S. Pauly, Y. Zhang, S. Scudino, P. Gargarella, K.B. Surreddi, U. Kühn, J. Eckert, Significant tensile ductility induced by cold rolling in Cu47.5Zr47.5Al5 bulk metallic glass, Intermetallics 19 (2011) 1394–1398.
[57] W.H. Wang, Dynamic relaxations and relaxation-property relationships in metallic glasses, Prog. Mater. Sci. 106 (2019).
[58] B. Sarac, Y.P. Ivanov, A. Chuvilin, T. Schöberl, M. Stoica, Z. Zhang, J. Eckert, Origin of large plasticity and multiscale effects in iron-based metallic glasses, Nat. Commun. 9 (2018) 1333.
[59] L. Krämer, V. Maier-Kiener, Y. Champion, B. Sarac, R. Pippan, Activation volume and energy of bulk metallic glasses determined by nanoindentation, Mater. Des. 155 (2018) 116–124.

Deformation-Mode-Sensitive Behavior of CuZr-Based Bulk Metallic Glasses Under Dynamic Loading

AMIR REZVAN, BARAN SARAC, VIKTOR SOPRUNYUK, FLORIAN SPIECKERMANN, CHRISTOPH GAMMER, HUAPING SHENG, NIKOLAUS AUGUST SIFFERLINGER, and JÜRGEN ECKERT

The viscoelastic behavior of four different bulk metallic glass (BMG) systems, i.e., $Cu_{46}Zr_{46}Al_8$, $Cu_{44}Zr_{44}Al_8Co_4$, $Cu_{44}Zr_{44}Al_8Hf_4$, and $Cu_{44}Zr_{44}Al_8Co_2Hf_2$, is investigated concerning its deformation-mode dependence via dynamic mechanical analysis (DMA) in 3-point bending (TPB), tension, and torsion modes. At temperatures below the glass transition, the considered BMGs deform primarily elastic, and the mechanical response is independent of the testing frequency, whereas, in the glass transition region, the viscoelastic component dominates. Crystallization decreases the viscoelastic contribution, whereas plastic deformation leads to an increase in atomic mobility for all three deformation modes. Compared to tension and torsion, TPB is found to be more sensitive to dynamic mechanical stress. TPB generates a complex stress state in the matrix and can thus introduce substantial variations in loss modulus. Structural analyses carried out by transmission electron microscopy and X-ray diffraction confirmed the amorphous nature of the base composition and structural changes when heated to the intermediate peak temperature observed at 743 K for the TPB mode. Compared to $Cu_{46}Zr_{46}Al_8$, 4 at. pct Co addition in the $Cu_{46\_x/2}Zr_{46\_x/2}Al_8Co_x$ amorphous alloy leads to a glass showing relatively higher thermomechanical stability around its glass transition. This study provides evidence for the enhancement of the mechanical properties of CuZr-based BMGs at elevated temperatures by microalloying.

AMIR REZVAN is with the Erich Schmid Institute of Materials Science, Austrian Academy of Sciences (ÖAW), Jahnstraße 12, A-8700 Leoben, Austria and also with the Department of Materials Science, Chair of Materials Physics, Montanuniversität Leoben, Jahnstraße 12, A-8700 Leoben, Austria. BARAN SARAC, CHRISTOPH GAMMER and HUAPING SHENG

are with the Erich Schmid Institute of Materials Science, Austrian Academy of Sciences (ÖAW). VIKTOR SOPRUNYUK is with the Erich Schmid Institute of Materials Science, Austrian Academy of Sciences (ÖAW) and also with the University of Vienna, Faculty of Physics, Physics of Functional Materials, Boltzmanngasse 5, A-1090 Wien, Austria. FLORIAN SPIECKERMANN is with the Department of Materials Science, Chair of Materials Physics, Montanuniversität Leoben. NIKOLAUS AUGUST SIFFERLINGER is with the Department of Mineral Resources Engineering, Chair of Mining Engineering and Mineral Economics, Montanuniversität Leoben, Franz-Josef-Straße 18 A-8700 Leoben, Austria. JÜRGEN ECKERT is with the Erich Schmid Institute of Materials Science, Austrian Academy of Sciences (ÖAW) and also with the Department of Materials Science, Chair of Materials Physics, Montanuniversität Leoben.

I. INTRODUCTION

The assessment of the structure–property relationships in glasses is rather limited due to their disordered atomic structure.[1–5] Besides, investigations of the thermomechanical stress state of bulk metallic glasses (BMGs) under high loading conditions are quite challenging because of the temperature- and pressure-dependent crystallization around the supercooled liquid region (SCLR).[6–15] The deformation of a material resulting from mechanical stress is in general made up of three components: an instantaneous and reversible elastic component, a reversible but time-delayed viscoelastic (or anelastic) component, and a time-dependent and irreversible viscoplastic component.[16,17] In this respect, dynamic mechanical analysis (DMA) is a reliable tool to investigate these different components by applying a small dynamic vibrational loading in the course of heating.[18–25] DMA can monitor the temperature and frequency dependence of both the storage and loss moduli of BMGs.[23,26,27] From a practical viewpoint, the elastic and viscoelastic properties of BMGs at different temperatures under dynamic loading conditions provide insight into the processability and mechanical performance of different BMGs. This paper reports thoroughly on the mode-dependent relaxation and crystallization behavior of CuZrAl-based BMGs with minor Co and/or Hf additions.

II. MATERIALS AND METHOD

Master alloys of $Cu_{46}Zr_{46}Al_8$, $Cu_{44}Zr_{44}Al_8Co_4$, $Cu_{44}Zr_{44}Al_8Hf_4$, and $Cu_{44}Zr_{44}Al_8Co_2Hf_2$ were prepared in a Buehler AM0.5 arc melting system under a Ti-gettered argon atmosphere. The purity of the industrial-grade alloy constituents was above 99.8 pct. Rotary and diffusion pumps were utilized to evacuate the system down to 10^{-6} mbar. Upon melting, the current was raised to a maximum of 150 A. To homogenize the ingots thoroughly, the melting was repeated four times. The alloys were cast afterwards into rectangular plates with dimensions of 10 mm in width and 75 mm in length, and a thickness of 2 mm using a copper mold. The pressure gradient between the mold cavity and the working chamber necessary for the suction was attained by purging argon into the upper chamber. From the cast plates, rectangular pieces with 10 mm length, 1 mm width, and 2 mm thickness were cut for further investigation using a custom-built wire saw. The specimens were ground and polished down in equal thicknesses from both sides to a thickness of 1.00 ± 0.05 mm. The samples were tested consecutively by dynamic mechanical analysis in three different modes of deformation configuration (each test repeated multiple times to determine the error) while purging with N_2 gas continuously upon heating and cooling. For all the samples and modes of deformation, a constant heating rate of 10 K/min was employed within a temperature range from 300 K to 850 K, mainly at a fixed frequency of 1 Hz. 3-point bending (TPB) and tension were conducted under 10 N force (a sequence of 60 pct static and 40 pct dynamic load) in a displacement-controlled condition with a displacement oscillation amplitude of 10 μm. Torsion was performed by imposing 5000 μN.m torque. As a comparison, another $Cu_{46}Zr_{46}Al_8$ sample was heated to 743 K at the same heating rate and cooling condition. Structural analysis was conducted by X-ray diffraction (XRD) employing a Bruker D2 Phaser diffractometer with Co K_α radiation (λ = 1.7902 Å) with a step size of 0.02 degrees. Detailed structural analysis of the base composition ($Cu_{46}Zr_{46}Al_8$) was carried out using transmission electron

microscopy (TEM). Sample preparation was performed by cutting thin slices from the BMG plate, grinding, and polishing using a dimple grinder. Final thinning to electron transparency was performed using ion milling (Gatan PIPS2). Ion milling was conducted at low energies using liquid nitrogen cooling to eliminate heating upon sample preparation. The TEM analyses were conducted using a JEOL 2100F equipped with an imaging spherical aberration corrector (CEOS) at 200 kV. Selected area diffraction (SAD) patterns and high-resolution TEM (HRTEM) images were recorded to verify the amorphous structure.

III. RESULTS AND DISCUSSION

A. Structural Analysis

Transmission electron microscopy (TEM) study of the base composition ($Cu_{46}Zr_{46}Al_8$) is shown in Figure 1. Neither crystals nor any features (i.e., defects, shear bands, or nanocrystals) are observed throughout the sample, which corroborates the amorphous state of the as-cast BMG.

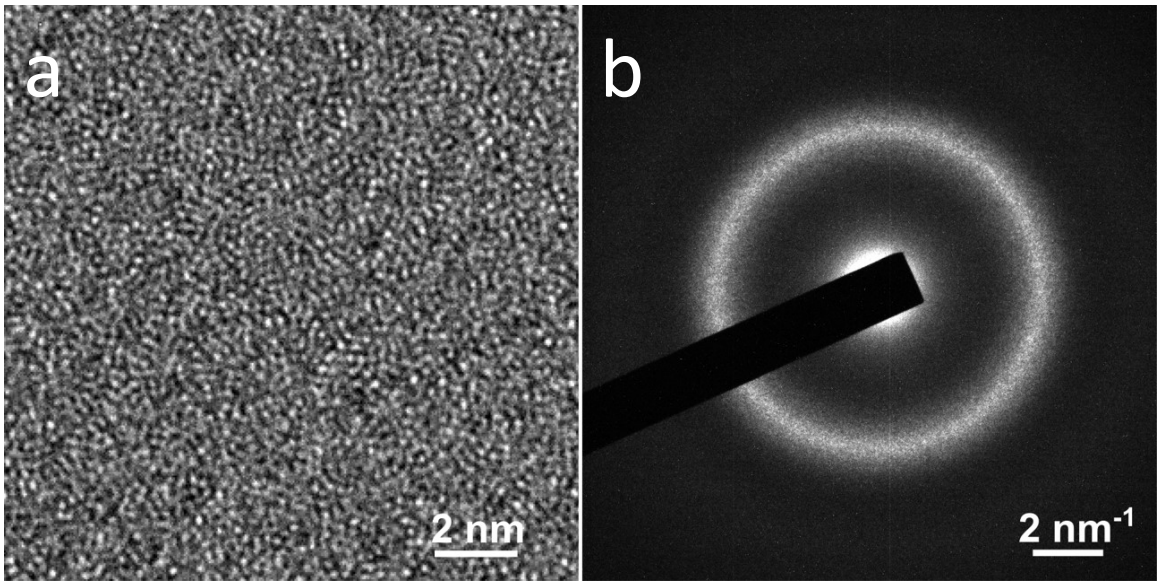

Fig. 1—(a) High-resolution TEM image, and (b) the corresponding selected area diffraction pattern confirming the amorphous state.

B. Influence of Deformation Modes

Figure 2 illustrates the dynamic mechanical analysis results of the $Cu_{46}Zr_{46}Al_8$ bulk metallic glass base composition tested under tension, torsion, and 3-point

bending (TPB). The glass transition temperature (T_g) is marked by the sudden change in the slope determined from the evolution of the loss modulus (G''). The onset of the increase in G' after the sharp drop corresponds to the onset of crystallization (T_x). Moreover, we observed an additional peak at 743 K in the loss modulus (G'') in the TPB mode. Similarly, the T_g and T_x values were registered from G'' in tension and torsion modes. The sample investigated under TPB shows an increase in the storage modulus (G') from 89 ± 1 GPa to 105 ± 1 GPa corresponding to β-relaxation. TPB can involve larger groups of atoms responding in a more cooperative oscillation manner compared to tension and torsion. No stiffening was observed for the samples upon tension and torsion, pointing out that the tension- and torsion-mode types of measurements are less sensitive to structural changes around the glass transition. G'' observed in TPB increases as the temperature approaches the glass transition temperature (T_g = 715 ± 1 K). G'' decreases afterwards with increasing the temperature to 729 K, followed by a second rise, as the temperature reaches 743 K. After 743 K, crystallization sets in, and thus G'' drops drastically to a minimum at 762 ± 1 K. At the tests domain, the stress in tension is 10 N/mm^2 over the sample, whereas upon TPB the maximum stress reaches 120 N/mm^2. The stress in TPB mode promotes the stress/strain induced transformation, by which crystallization sets in at lower temperatures. Excess wings observed in G'' are due to the β-relaxation of the amorphous matrix.[28–30]

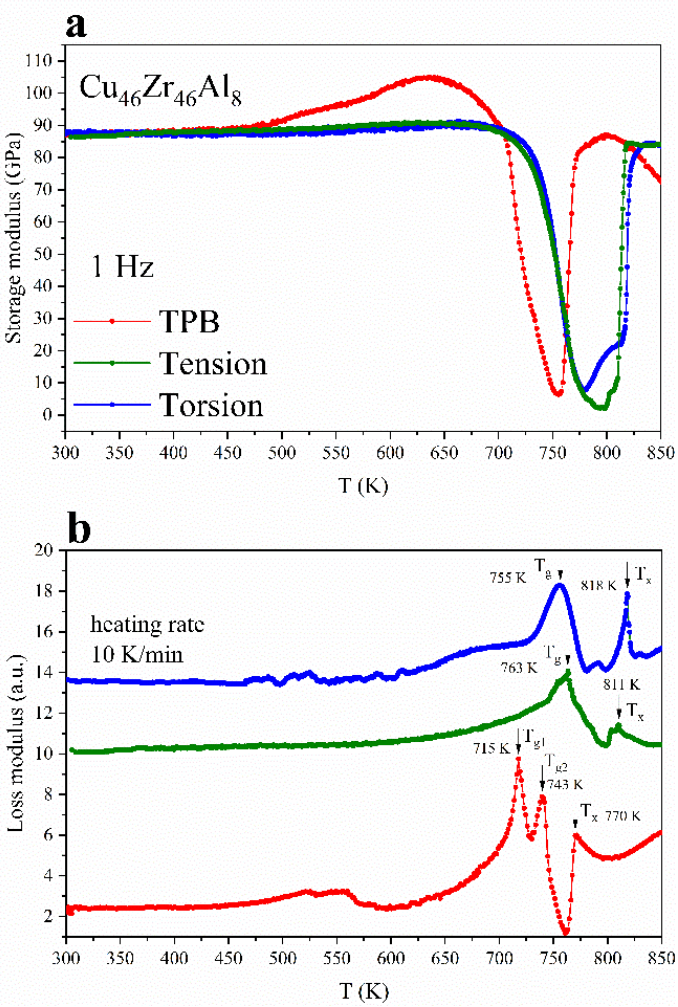

Fig. 2—(a) Storage modulus (G') and (b) loss modulus (G'') of Cu46Zr46Al8 BMG as a function of temperature. The frequency and heating rates are 1 Hz and 10 K/min, respectively.

To study the second glass transition (T_{g2}) event observed in G'' of TPB, the DMA test on the cast $Cu_{46}Zr_{46}Al_8$ sample of the stated dimensions was repeated in TPB in a temperature range of 300 K to 743 K. The sample was polished after DMA testing and compared to the as-cast $Cu_{46}Zr_{46}Al_8$ using X-ray diffraction (see Figure 3). After DMA, the second sharp diffraction peak broadens, indicating structural changes. Hence, it is concluded that the applied thermomechanical driving force can deviate the system from equilibrium, inducing structural heterogeneities.

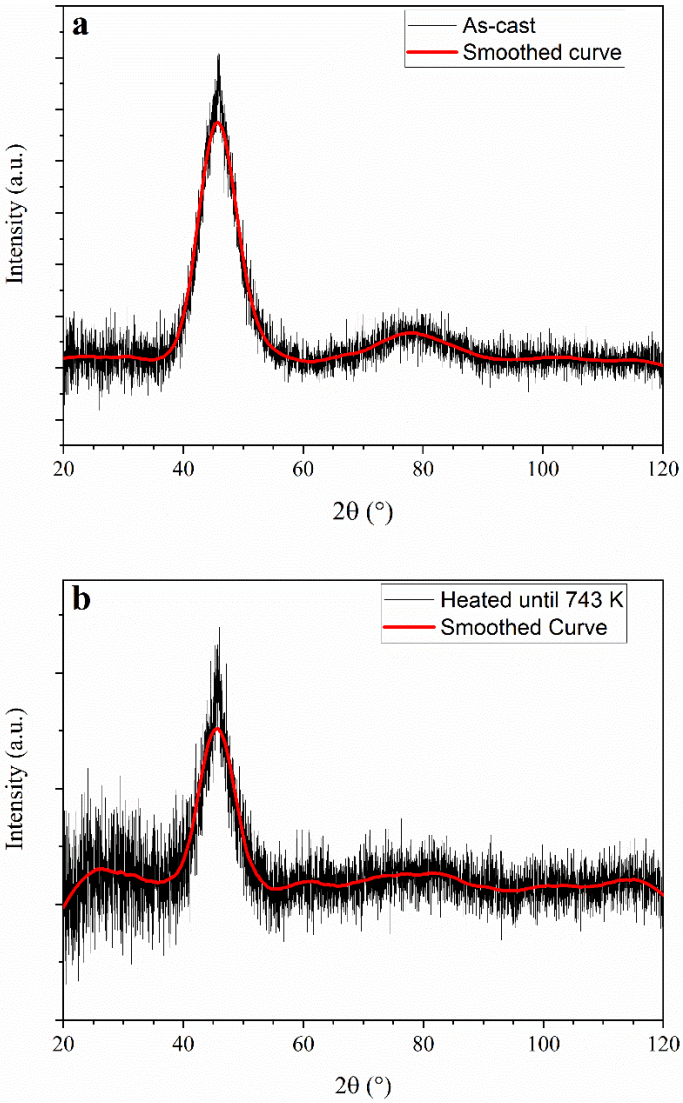

Fig. 3—XRD patterns of the Cu46Zr46Al8 (a) in the as-cast state and (b) after 743K in the DMA.

The storage modulus G' and the loss modulus G'' of CuZr-based BMGs are, in general, sensitive to the applied frequency. In order to assess the influence of frequency on the dynamic mechanical properties, specimens were tested in TPB configuration at a fixed heating rate of 10 K/min at various frequencies. Figure 4 presents the evolution of G' and G'' in $Cu_{46}Zr_{46}Al_8$ as a function of temperature at three different testing frequencies (0.1 to 1 to 10 Hz) employing the same heating rate. The position of the large decrease in G' after T_g and the large increase in the loss modulus G'' (corresponding to T_g) shifts towards higher temperatures when the frequency increases from 0.1 to 10 Hz. This variation was quantified by

recording the shift of the characteristic temperatures by changing the frequency. An Arrhenius plot of the frequency dependence of G' leads to an activation energy of E_a = 7.6 ± 0.1 eV (732 ± 10 kJ/mol), which is a typical value for cooperative relaxation processes.[19,20] This reasonably high value may be attributed to the collective motion of a large number of atoms in this BMG.[25,31,32] However, the frequency does not seem to have that much of an effect on the position of T_x as the frequency varies from 0.1 to 10 Hz. The variations in the G' and G'' peaks correspond simply to the increase in atomic mobility with increasing temperature or decreasing frequency. The extra peak in G'' at 1 Hz manifests the complex stress state of the TPB mode, which can trigger two different relaxation modes step by step until reaching T_x. However, this peak is smeared out at the frequencies of 0.1 and 10 Hz, which led us set the frequency to 1 Hz for the series of DMA tests to show more effects on the evolution of G''.

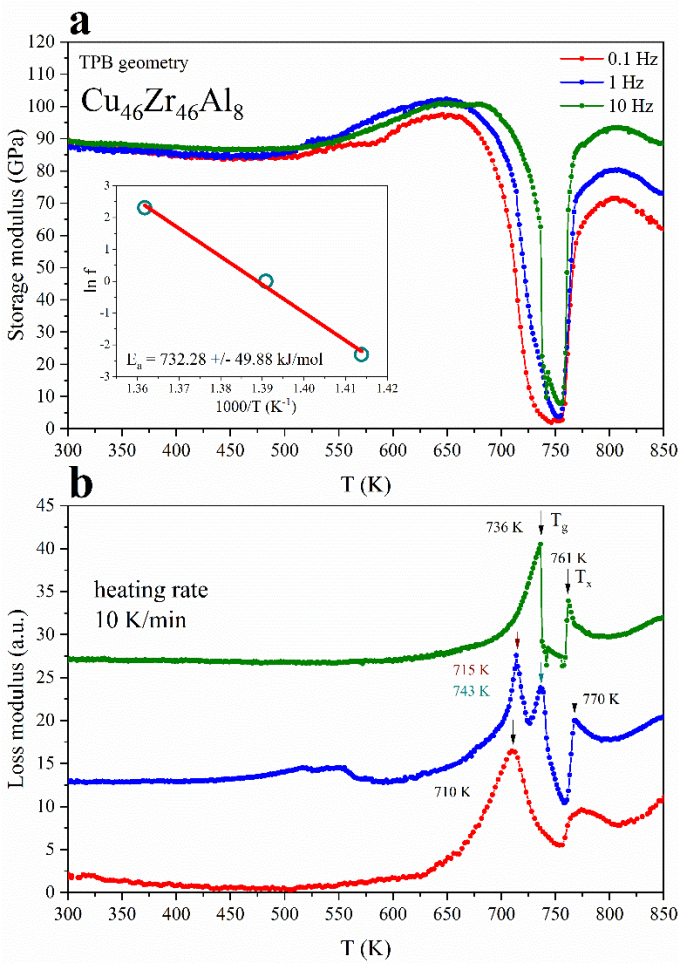

Fig. 4—Influence of the driving frequency on (a) the storage modulus (G') and (b) the loss modulus (G'') of $Cu_{46}Zr_{46}Al_8$ bulk metallic glass during continuous heating. The measurement frequencies were 0.1 to 1 to 10 Hz, and the heating rate was 10 K/min. The T_g measurements at different frequencies result in a linear Arrhenius behavior with a slope of 7.6 ± 0.1 eV obtained from the slope of the linear fit (inset).

Figure 5 displays the storage (G') and loss (G'') moduli of $Cu_{44}Zr_{44}Al_8Co_4$. Co addition increases T_g, and thus the thermal stability of the CuZrAl-base amorphous alloy. G'', as measured in TPB and torsion modes, remains constant in the glassy state at temperatures up to ~ 640 K. However, from 640 K to the T_g, it increases gradually due to the relaxation that occurs during heating. In the supercooled liquid region, a second peak (T_{g2}) is present in the G'' curve measured in TPB, confirming the sensitivity of the TPB analysis. Here, the SCLR is determined by the difference between the crystallization temperature and the glass transition temperature ($\Delta T_x = T_x - T_g$). It can be seen that the material shows higher resistance to thermomechanically induced changes under tension in comparison to TPB or torsion. By introducing 4 at. pct Co, amorphous phase separation occurs between softer Cu-rich and harder Co-rich phases in the matrix of $Cu_{44}Zr_{44}Al_8Co_4$ due to the positive heat of mixing of Cu-Co (6 kJ/mol). This suggests the strength retention at elevated temperatures. Compared to $Cu_{46}Zr_{46}Al_8$, 4 at. pct Co addition in the $Cu_{46-x/2}Zr_{46-x/2}Al_8Co_x$ amorphous alloy leads to a more stabilized G' at elevated temperatures, showing an increase in the thermomechanical stability.

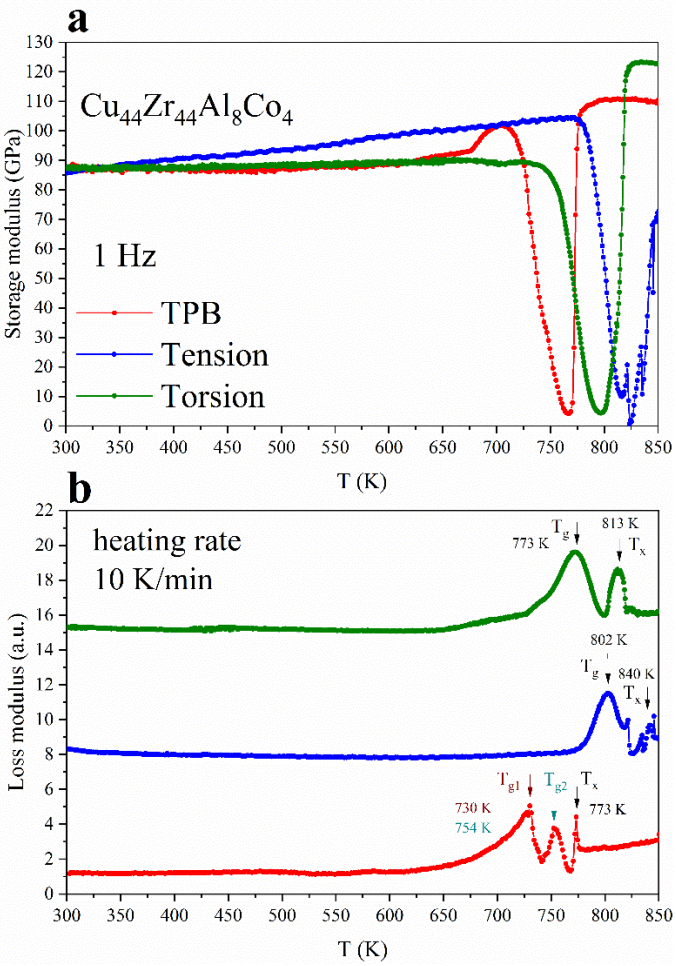

Fig. 5—Evolution of (a) the storage modulus (G') and (b) the loss modulus (G'') of $Cu_{44}Zr_{44}Al_8Co_4$ with temperature during continuous heating (10 K/min) from 300 K to 850 K at a fixed frequency of 1 Hz.

In the amorphous state, the dynamic mechanical properties of the $Cu_{44}Zr_{44}Al_8Hf_4$ alloy are similar to those observed for the $Cu_{44}Zr_{44}Al_8$ BMG. Figure 6 illustrates a pronounced difference between the onset of T_g in TPB mode compared to the other two modes observed in G'. T_g is characterized by the abrupt rise of G'', where the peak maximum in G'' can be addressed to T_x in G'. A larger hump indicating more stiffening of the $Cu_{44}Zr_{44}Al_8Hf_4$ alloy can be seen in the G' upon TPB. Similar to the previous samples, a pronounced dynamic glass transition, T_{g2}, is observed only in the TPB mode of deformation. In tension mode type of measurement, the T_g event sets in at higher temperatures compared to the other two deformation modes. Thus, in tension, a larger thermo-mechanical driving

force is required to visualize the modifications, which can be considered as a disadvantage of the tensile deformation mode.

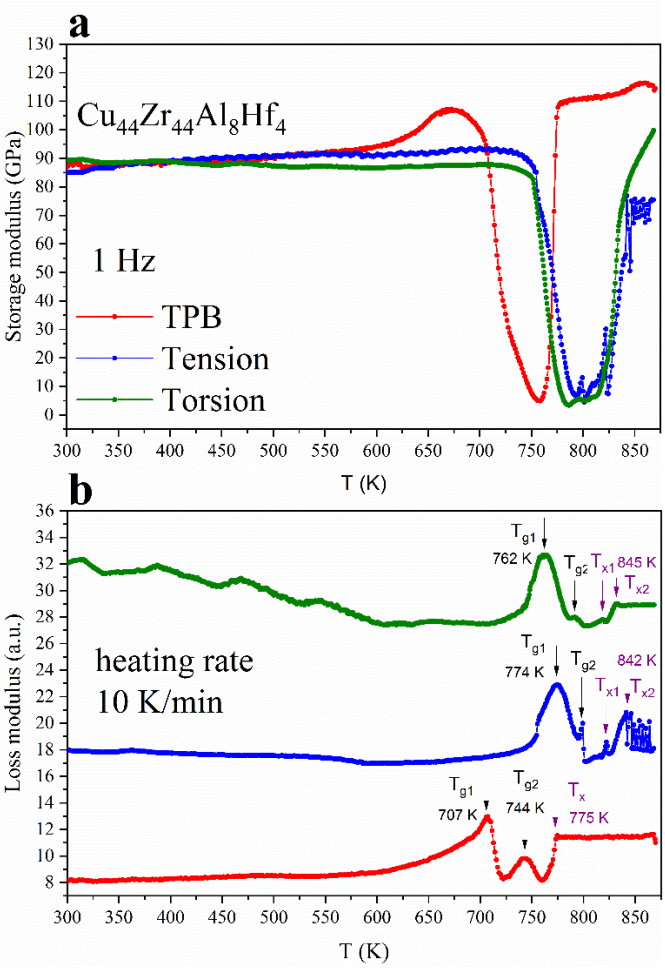

Fig. 6—Temperature dependence of (a) the storage (G') and (b) the loss moduli (G'') determined during continuous heating from 300 K to 850 K with a heating rate of 10 K/min at a testing frequency of 1 Hz.

Figure 7 shows the influence of adding two different minor alloying elements, i.e., Co and Hf. The presence of Co and Hf atoms (2 at. pct each) in the given proportion induces a more uniform profile of G' and G'' vs. temperature. Due to the shift of T_g towards higher temperatures and T_x being constant, ΔT becomes narrower. Combined with the results of Figure 5, these observations suggest that in the studied CuZr-based BMGs Co is the main minor alloying element influencing the dynamic behavior.

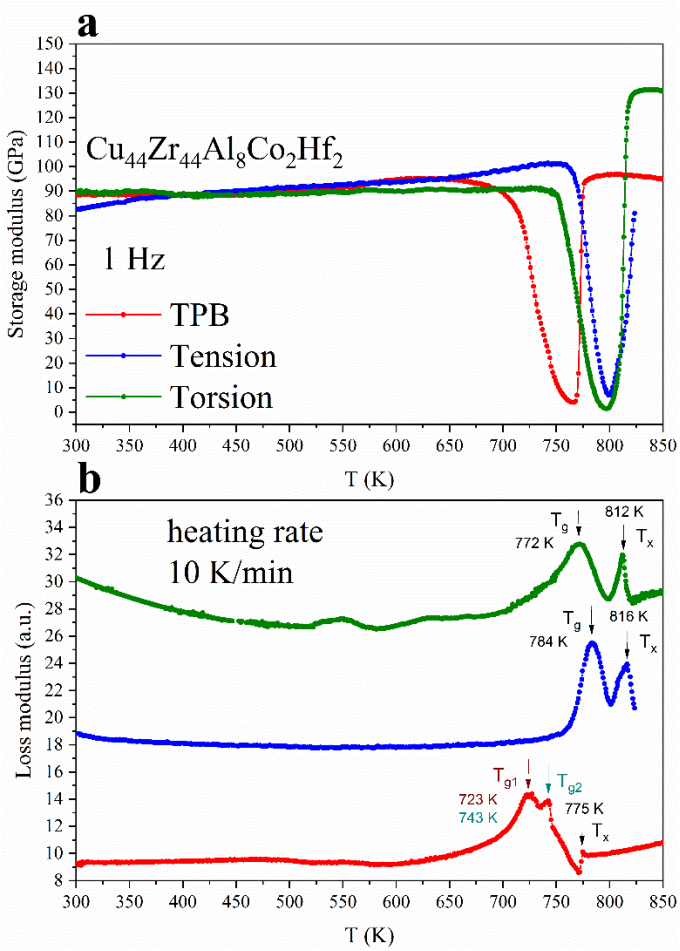

Fig. 7—(a) Storage (G') and (b) loss (G'') moduli of $Cu_{44}Zr_{44}Al_8Co_2Hf_2$ determined from 300 K to 850 K at a heating rate of 10 K/min and a frequency of 1 Hz.

Figure 8 illustrates the DMA results of the 4 different BMGs (i.e., $Cu_{46}Zr_{46}Al_8$, $Cu_{44}Zr_{44}Al_8Co_4$, $Cu_{44}Zr_{44}Al_8Hf_4$, and $Cu_{44}Zr_{44}Al_8Co_2Hf_2$) investigated under TPB. Co addition increases T_g, and thus the thermal stability of the CuZrAl-base amorphous alloy. The T_g of the $Cu_{44}Zr_{44}Al_8Hf_4$ alloy is similar to that observed for the $Cu_{44}Zr_{44}Al_8$. The presence of Co and Hf atoms (2 at. pct each) in the given proportion leads to a glass showing a more uniform profile of G' and G'' vs. temperature.

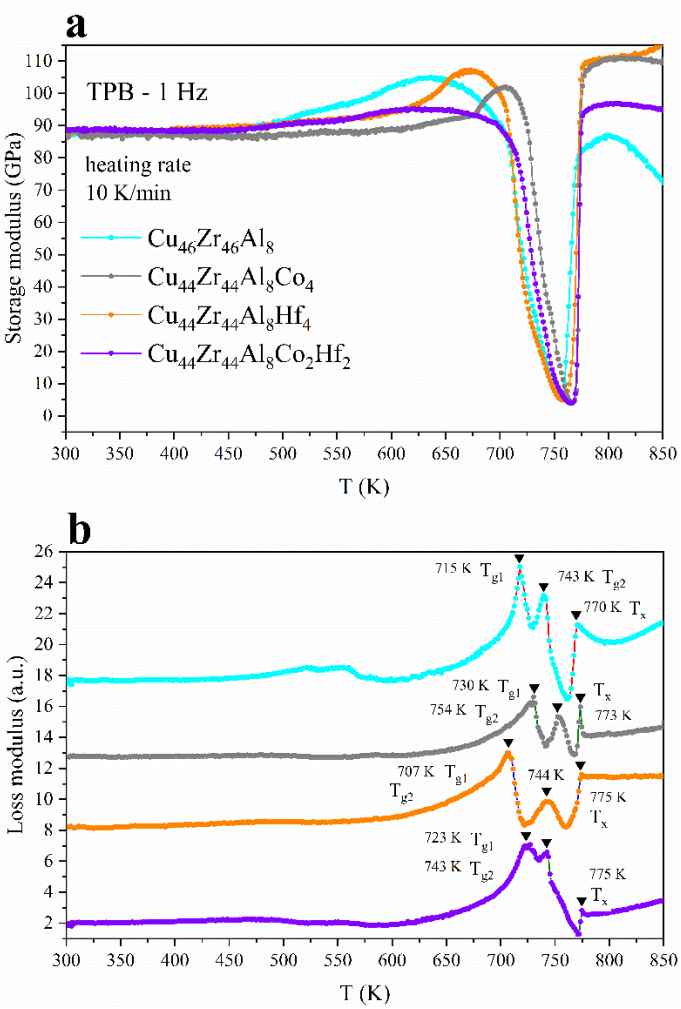

Fig. 8—Evolution of (a) the storage modulus (G') and (b) the loss modulus (G'') of the studied four BMGs ($Cu_{44}Zr_{44}Al_8$, $Cu_{44}Zr_{44}Al_8Co_4$, $Cu_{44}Zr_{44}Al_8Hf_4$, and $Cu_{44}Zr_{44}Al_8Co_2Hf_2$) with temperature during continuous heating (10 K/min) from 300 K to 850 K at a fixed frequency of 1 Hz.

IV. CONCLUSION

Measurements of the dynamic shear modulus in a temperature range of 300 K to 850 K have been performed on four types of CuZr-based bulk metallic glasses with various Hf and/or Co contents (2 to 4 at. pct), i.e., $Cu_{46}Zr_{46}Al_8$, $Cu_{44}Zr_{44}Al_8Co_4$, $Cu_{44}Zr_{44}Al_8Hf_4$, and $Cu_{44}Zr_{44}Al_8Co_2Hf_2$. Casting rectangular plates can generate fully glassy BMGs, as confirmed by an HRTEM study. The temperature of this transition is shifted towards higher temperatures when the testing frequency is increased for a given alloy, or when the Co content is increased for a given testing frequency. Thus, these observations suggest that the

Co content in the studied CuZr-based BMG leads to an enhancement in the dynamic mechanical stability at elevated temperatures. Upon 3-point bending, a pronounced second peak (T_{g2}) in G'' and broadening of the second broad diffraction peak are observed. This finding highlights the fact that, compared to tension and torsion, the TPB at 1 Hz frequency induces a complex stress state, and, thereby, triggers two different relaxation modes step by step until reaching T_x. The high value of the activation energy of this thermomechanically activated phenomenon indicates that a collective movement of atoms is involved in this relaxation process. Different from DMA tests performed under tension and torsion, the complex stress state generated by 3-point bending reveals the high measurement sensitivity manifested by the presence of an additional glass transition peak (T_{g2}).

ACKNOWLEDGMENTS

The authors would like to thank Eray Yüce, Parthiban Ramasamy, and Vladislav Zadorozhnyy for fruitful discussions, and Atacan Asci for his assistance with sample preparation. This work was supported by the European Research Council under the Advanced

Grant ‘‘INTELHYB – Next Generation of Complex Metallic Materials in Intelligent Hybrid Structures” (Grant No: ERC-2013-ADG-340025) and the Austrian Science Fund (FWF) under Project Grant I3937-N36.

REFERENCES

1. J. Schroers and N. Paton: Adv. Mater. Process., 2006, vol. 164, pp. 61–63.

2. R.W. Cahn, and A.L. Greer: in Physical Metallurgy (Fourth Edition), R.W. Cahn, and P. Haasen, eds., North-Holland, Oxford, 1996, pp 1723–1830.

3. Y.T. Cheng and W.L. Johnson: Science, 1987, vol. 235, pp. 997–1002.

4. B. Sarac and J. Schroers: Nat. Commun., 2013, vol. 4, p. 2158.

5. B. Sarac: Microstructure-Property Optimization in Metallic Glasses, Springer, Berlin, 2015, p. 89.

6. C.R. Jin, S.Y. Yang, X.Y. Deng, Y.W. Wang, and X.W. Cheng: Acta Metall. Sin. (Engl. Lett.), 2019, vol. 55, pp. 1561–68.

7. B. Sarac, J. Ketkaew, D.O. Popnoe, and J. Schroers: Adv. Funct. Mater., 2012, vol. 22, pp. 3161–69.

8. A. Révész, A. Horváth, G. Ribárik, E. Schafler, D.J. Browne, and Z. Kovács: Rev. Adv. Mater. Sci., 2019, vol. 58, pp. 304–12.

9. W.H. Gao, X.Y. Yi, X.L. Meng, G. Song, W. Cai, and L.C. Zhao: J. Mater. Sci. Technol., 2017, vol. 33, pp. 276–80.

10. Z.J. Yan, Y. Hu, K.K. Song, F.P. Dai, J. He, and J. Eckert, Appl. Phys. Lett., 2015, vol. 106.

11. B. Sarac, F. Spieckermann, A. Rezvan, C. Gammer, L. Krämer, J.T. Kim, J. Keckes, R. Pippan, and J. Eckert: J. Alloys Compd., 2019, vol. 784, pp. 1323–33.

12. B. Sarac, A. Bernasconi, J. Wright, M. Stoica, F. Spieckermann, M. Mühlbacher, J. Keckes, X. Bian, G. Wang, and J. Eckert: Mater. Sci. Eng. A, 2017, vol. 707, pp. 245–52.

13. B. Sarac, L. Zhang, K. Kosiba, S. Pauly, M. Stoica, and J. Eckert: Sci. Rep., 2016, vol. 6, p. 27271.

14. I. Okulov, I. Soldatov, I. Kaban, B. Sarac, F. Spieckermann, and J. Eckert: Nanomaterials, 2020, vol. 10, p. 84.

15. K.K. Song, X.L. Han, S. Pauly, Y.S. Qin, K. Kosiba, C.X. Peng, J.H. Gong, P.X. Chen, L. Wang, B. Sarac, S. Ketov,

M. Mühlbacher, F. Spieckermann, I. Kaban, and J. Eckert: Mater. Des., 2018, vol. 139, pp. 132–40.

16. In Mechanics of Solid Materials, J. Lemaitre, and C. Jean-Louis, eds., Cambridge University Press, Cambridge, 1990, pp 253–345.

17. In Mechanics of Solid Materials, J. Lemaitre, and C. Jean-Louis, eds., Cambridge University Press, Cambridge, 1990, pp 121–160.

18. J.M. Pelletier, C. Gauthier, and E. Munch: Mater. Sci. Eng. A, 2006, vol. 442, pp. 250–55.
19. J.M. Pelletier, J. Perez, and L. Duffrene: Acta Mater., 2000, vol. 48, pp. 1397–1408.
20. Q. Wang, J.M. Pelletier, and J.J. Blandin: J. Alloys Compd., 2010, vol. 504, pp. 357–61.
21. H.T. Jeong, E. Fleury, W.T. Kim, D.H. Kim, and K. Hono: J. Phys. Soc. Jpn., 2004, vol. 73, pp. 3192–97.
22. H.T. Jeong, E. Fleury, W.T. Kim, and D.H. Kim: Met. Mater. Int., 2007, vol. 13, pp. 447–53.
23. Z.F. Zhao, P. Wen, C.H. Shek, and W.H. Wang: Phys. Rev. B, 2007, vol. 75, p. 174201.
24. J.M. Pelletier, B. van de Moortèle, and J. Non-Cryst: Solids, 2007, vol. 353, pp. 3750–53.
25. K. Schröter, G. Wilde, R. Willnecker, M. Weiss, K. Samwer, and E. Donth: Eur. Phys. J. B, 1998, vol. 5, pp. 1–5.
26. J. Hachenberg, D. Bedorf, K. Samwer, R. Richert, A. Kahl, M.D. Demetriou, and W.L. Johnson: Appl. Phys. Lett., 2008,
vol. 92, p. 131911.
27. X.F. Liu, B. Zhang, P. Wen, W.H. Wang, and J. Non-Cryst: Solids, 2006, vol. 352, pp. 4013–16.
28. D. Suh, R.H. Dauskardt, and J. Non-Cryst: Solids, 2003, vol. 317, pp. 181–86.
29. W.H. Wang, P. Wen, X.F. Liu, and J. Non-Cryst: Solids, 2006, vol. 352, pp. 5103–09.
30. J.C. Qiao, R. Casalini, J.M. Pelletier, and J. Non-Cryst: Solids, 2015, vol. 407, pp. 106–09.

31. S. Etienne, J.Y. Cavaillé, J. Perez, R. Point, and M. Salvia: Rev. Sci. Instrum., 1982, vol. 53, pp. 1261–66.
32. S. Puech, J.J. Blandin, and J.L. Soubeyroux: Adv. Eng. Mater., 2007, vol. 9, pp. 764–68.

Antibacterial activity, cytocompatibility, and thermomechanical stability of $Ti_{40}Zr_{10}Cu_{36}Pd_{14}$ bulk metallic glass

Amir Rezvan[a,b], Elham Sharifikolouei[c], Alice Lassnig[a], Viktor Soprunyuk[d], Christoph Gammer[a], Florian Spieckermann[b], Wilfried Schranz[d], Ziba Najmi[e], Andrea Cochis[e], Alessandro Calogero Scalia[e], Lia Rimondini[e], Marcello Manfredi[f], Jürgen Eckert[a,b], Baran Sarac[a]

[a] *Erich Schmid Institute of Materials Science, Austrian Academy of Sciences, A-8700, Leoben, Austria*

[b] *Department of Materials Science, Chair of Materials Physics, Montanuniversität Leoben, A-8700, Leoben, Austria*

[c] *Department of Applied Science and Technology, Politecnico di Torino, Corso Duca Degli Abruzzi 24, 10129, Turin (TO), Italy*

[d] *University of Vienna, Faculty of Physics, Physics of Functional Materials, A-1090, Vienna, Austria*

[e] *Department of Health Sciences, Center for Translational Research on Autoimmune and Allergic Diseases – CAAD, Università Del Piemonte Orientale UPO, Corso Trieste 15/A, 28100, Novara (NO), Italy*

[f] *Department of Translational Medicine, Center for Translational Research on Autoimmune and Allergic Disease – CAAD, Università Del Piemonte Orientale UPO, Corso Trieste 15/A, 28100, Novara (NO), Italy*

ABSTRACT

This paper envisions $Ti_{40}Zr_{10}Cu_{36}Pd_{14}$ bulk metallic glass as an oral implant material and evaluates its antibacterial performance in the inhabitation of oral biofilm formation in comparison with the gold standard Ti–6Al–4V implant material. Metallic glasses are superior in terms of biocorrosion and have a reduced stress shielding effect compared with their crystalline counterparts. Dynamic mechanical and thermal expansion analyses on $Ti_{40}Zr_{10}Cu_{36}Pd_{14}$ show that these materials can be thermomechanically shaped into implants. Static water contact angle measurement on samples' surface shows an increased surface wettability on the Ti–6Al–4V surface after 48 h incubation in the water while the contact angle remains constant for $Ti_{40}Zr_{10}Cu_{36}Pd_{14}$. Further, high-resolution

transmission and scanning transmission electron microscopy analysis have revealed that $Ti_{40}Zr_{10}Cu_{36}Pd_{14}$ interior is fully amorphous, while a 15 nm surface oxide is formed on its surface and assigned as copper oxide. Unlike titanium oxide formed on Ti–6Al–4V, copper oxide is hydrophobic, and its formation reduces surface wettability. Further surface analysis by X-ray photoelectron spectroscopy confirmed the presence of copper oxide on the surface. Metallic glasses cytocompatibility was first demonstrated towards human gingival fibroblasts, and then the antibacterial properties were verified towards the oral pathogen Aggregatibacter actinomycetemcomitans responsible for oral biofilm formation. After 24 h of direct infection, metallic glasses reported a >70% reduction of bacteria viability and the number of viable colonies was reduced by ~8 times, as shown by the colony-forming unit count. Field emission scanning electron microscopy and fluorescent images confirmed the lower surface colonization of metallic glasses in comparison with controls. Finally, oral biofilm obtained from healthy volunteers was cultivated onto specimens' surface, and proteomics was applied to study the surface property impact on species composition within the oral plaque.

Graphical Abstract

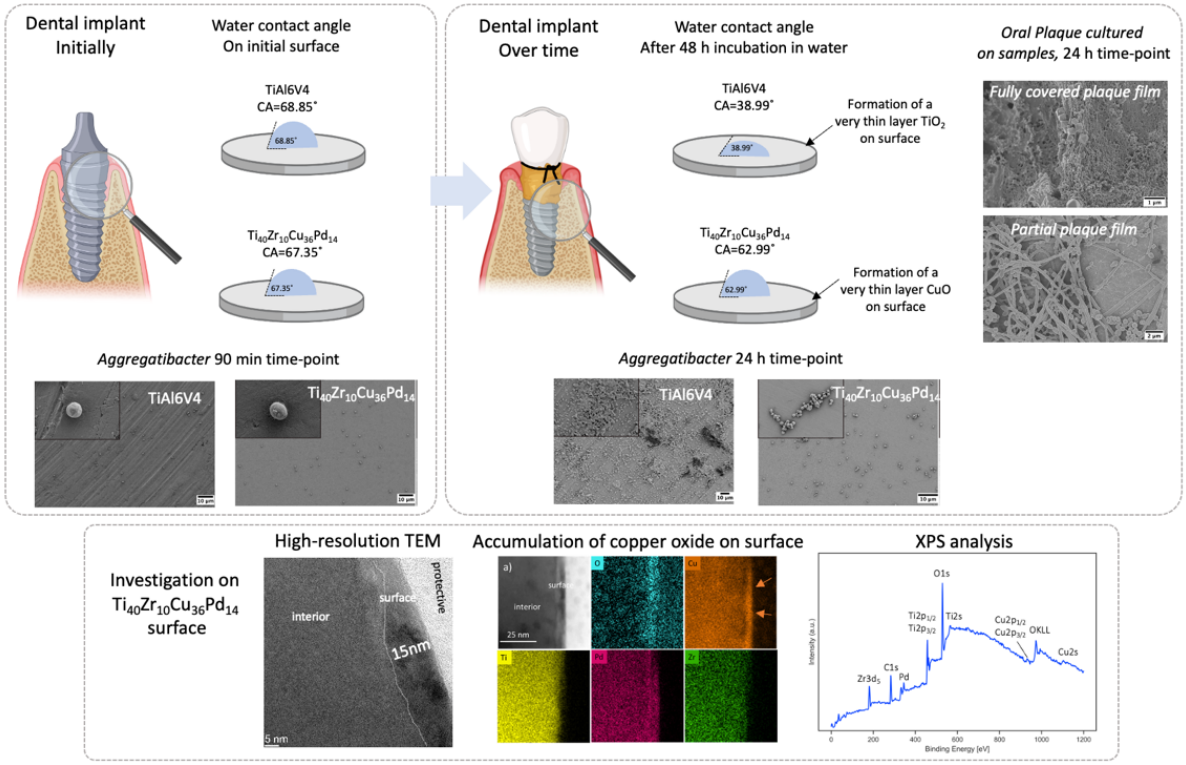

1. Introduction

Bacterial biofilm formation on oral implant surfaces is a leading cause of the development of peri-implant inflammatory disease, which affects the surrounding tissue of the implant, predominately the bone. The adhesion of pathogenic biofilm on the implant and peri-implant tissues results in bone loss and destruction of connective soft tissue. Currently, the gold standard oral implant is based on Ti–6Al–4V alloy. The combination of good biocompatibility and high strength makes Ti–6Al–4V alloy a desirable choice for oral implants. However, several disadvantages, including its elastic modulus mismatch with bone leading to a stress-shielding effect [1], weak wear resistance contributing to inflammation and fatigue corrosion, as well as the low hardness, have led to the search for alternative implant materials.

Sometimes above 500 bacterial species are involved in forming a biofilm on oral implant surfaces [2] that briefly starts with pellicle formation on the surface, followed by reversible bacterial adhesion with feeble interactions between

bacterial pellicle and implant surface or tissues around it that can conduct strong interactions. Finally, due to bacterial co-adhesion and the production of extra cellular polysaccharide matrix, a sophisticated 3D bacterial community is created into biofilm structures [3,4]. A great body of research has been conducted on the development of implant surfaces to interfere with each of the above-mentioned steps and, as a result, minimize the bacterial biofilm formation on oral implants. The development of antibacterial surfaces yet cytocompatible oral implants is not an easy task. There are several approaches to prevent or counteract bacterial colonization, such as the generation of superhydrophobic antifouling surfaces preventing the early adhesion. Sharifikolouei et al. have shown that zirconium-based metallic glasses with superhydrophobic surfaces can prohibit bacterial adhesion formation up to 95% while keeping their cytocompatibility up to 97% [5]. However, since oral implants are required to be well integrated within the pre-implant and bone tissue, superhydrophobicity of the surface might be a disadvantage. In fact, it has been shown that porous and hydrophilic surfaces might show superior bone growth and molecular surface functionalization [6,7]. Ferraris et al. have shown that the creation of a thin layer of nanotextured titanium oxide on Ti-implants can promote superior osseointegration, and the nanotextured pattern can help with the antifouling properties against Gram-positive and Gram-negative bacteria [8]. In another attempt, Li et al. have shown that Ti-implants coated with graphene enhance the biological activity of the implant surface and may further promote in vivo osteogenesis and osseointegration [9]. However, the long-term mechanical stability of graphene nanocoating is not studied, and it requires further evaluation. Surface functionalization of Ti implants is another popular approach to create cytocompatible and antibacterial surfaces. As an example, natural biomolecules such as gallic acid and polyphenols extracted from natural byproducts are shown to be successful for this purpose [10]. Another example is the loading of mesoporous dopamine (MPDA) nanoparticles with nitric oxide (NO) donor, S-

nitrosoglutathione (GSNO), which were immobilized on the surface of titanium (Ti) to reduce bacterial infection and improve osseointegration [11].

Bulk metallic glasses (BMGs) are relative newcomers in materials science, showing unique behavior due to the absence of crystallinity and the associated lack of microstructural features such as grain and phase boundaries [1,12–14]. Among advanced glassy multicomponent systems, Ti-based BMGs are exploited as biomedical materials mainly owing to low Young's modulus, high processability, good biocompatibility, and bioactivity of the Ti element [15–19]. Besides, they have a higher oxidation resistance, corrosion passivity, and lower corrosion current density than conventionally used Ti– 6Al–4V alloys, indicating a better corrosion resistance [20]. It has been proven that the mechanical, corrosion, biocompatible and antibacterial properties of Cu-bearing Ti-based BMG were enhanced by controlling the porosity [21–23]. Moreover, Ti-MGs and composites have 1.5 to 2 times better wear resistance than Ti-based crystalline alloys [24,25]. The grain-free microstructure also yields twice to three times higher fracture strength and hardness as compared to other conventionally used crystalline Ti-based alloys [26,27]. In the literature, some metallic glass types are reported as potential biomaterials considering the bioactivity of the constituent elements and their intermetallic compounds [28,29]. $Ti_{40}Zr_{10}Cu_{36}Pd_{14}$ BMG is robust in dental applications with high resistance to sterilization and corrosion when submerged in 0.9 wt% NaCl solution [30]. It possesses, in comparison to Ti–6Al 4V, higher strength and lower Young's modulus, which is beneficial in reducing the stress-shielding effect [31–34]. Moreover, metallic glasses show extensive plastic-like processability when heated to elevated temperatures [35,36]. These properties motivated us to study $Ti_{40}Zr_{10}Cu_{36}Pd_{14}$ BMG further.

To develop any concept in the framework of biomedical alloy systems, the biological safety investigation of compositions is of utmost importance in order to avoid adverse reactions to the human body. As an example, to broaden the concept, implantation guidelines for oral implants [37] suggest the application of

antibiotics as a precaution to avoid post-operative infections. This necessity is, however, problematic in a twofold manner. The increased presence of drug-resistant bacteria [38] reduces the options in the case of post-operative infections, and on the other hand, the development of antibiotic resistance is increased by the increasing prophylactic application of antibiotics. Moreover, surgical site infections (SSI) may be underestimated due to dormant bacteria that adhered to the initially sterile implant during the surgical intervention. Such dormant infections may break some weeks or months later. It is thus crucial to reduce the adhesion of microbial biofilms to the implant surface or control the bactericidal load over time to counteract the rising infection. Furthermore, the biocompatibility and the tissue- and osseointegration should be preserved. Specific groups of metallic glasses are believed to answer some of these issues.

In this work, first the microstructure and the mechanical properties of $Ti_{40}Zr_{10}Cu_{36}Pd_{14}$-BMG metallic glass are investigated. Then the evaluation of its performance as an oral implant is specifically investigated towards the oral strain Aggregatibater actinomycetemcomitans that is considered one of the main pathogen responsible for oral periodontal and peri-implant diseases. Moreover, to mimic the real conditions, oral plaque is collected from healthy volunteers and cultured on the implant devices; the changes in the bacterial consortium in response to the material is investigated by proteomics analysis.

2. Materials and methods

2.1. Casting

A $Ti_{40}Zr_{10}Cu_{36}Pd_{14}$ master alloy was synthesized using an Edmund Buehler AM0.5 arc melting system operating under a Ti-gettered argon atmosphere. The industrial-grade alloy constituents of 99.9% purity were weighed with an accuracy of ± 0.001 g. Rotary and diffusion pumps were utilized to evacuate the system to to 10^{-7} mbar. Upon melting, the melting current was raised to 160 A. To homogenize the ingot thoroughly, the melting was repeated four times. The

alloy was cast afterwards into a copper mold with a rod geometry of 3 mm in diameter and 60 mm in length. The pressure gradient required for suction between the designed mold cavity and the working chamber was attained by purging argon. From the cast rod pieces were cut for characterizations.

2.2. XRD, DSC, and TEM analyses

Structural analysis was conducted by X-ray diffraction (XRD) employing a Bruker D2 Phaser diffractometer with Co Kα radiation (λ = 1.7902 Å) with a step size of 0.02°. Differential scanning calorimetry (DSC) tests were performed with a Mettler Toledo DSC 3+ under an argon atmosphere at a constant heating rate of 10 K/min. The weight of the specimens was 10 ± 0.5 g. They were heated twice in the DSC, and normalization was done by subtracting the baseline from the original heating curve. The cooling rate between cooling intervals was 50 K/min to minimize the effect of the time spent for cooling on the overall DSC data. All the DSC measurements were repeated 4 times, and an error of ± 2 K was determined for the glass transition and crystallization temperatures. Detailed structural analysis was carried out using transmission electron microscopy (TEM). An electron transparent lamella of the surface region was created via focused ion beam (FIB) lift-out technique within a Zeiss Auriga workstation equipped with an omniprobe micromanipulator. To protect the sample surface during FIB cutting a protective carbon layer and an amorphous W layer was deposited on top of the surface using the gas injection system (GIS) of the work station. Coarse trench cuts up to fine polishing of the lamella was performed at acceleration voltage of 30 kV and current ranging from 2 nA down to 50 pA. The TEM analyses were conducted in a JEOL 2200FSat 200 kV, where HR-TEM was performed in the region close to the sample surface and the sample interior selected area diffraction (SAD) patterns and highresolution TEM (HR-TEM) images were recorded to verify the amorphous structure including TEM-EDX

analysis to study the elemental composition of the surface region and interior of the glass.

2.3. DMA and TE

Dynamic mechanical analysis (DMA) was conducted using a Diamond DMA (Perkin Elmer, Inc.) in compression mode within a temperature range from 300 K to 850 K while purging with N2 gas continuously upon heating, a constant heating rate of 10 K/min was employed at frequencies of 0.1 to 1 to 10 Hz. The specimens are solid rectangular shapes 6 mm in height and 3 mm in diameter. The experiments were performed by imposing 10 N axial force in a displacement-controlled mode with a displacement oscillation amplitude of 10 μm. Thermal expansion/ contraction (TE) was measured using a thermomechanical analyzer TMA 4000 (Perkin Elmer, Inc.) under a constant load of 50 mN. The specimens were heated from 300 K to 850 K at a 10 K/min heating/cooling rate.

2.4. Wear resistance analysis

Specimens (3 mm diameter) were submerged with 7 ml/specimen of artificial saliva solution and were placed inside a shaker (120 rpm, T = 37 °C) for 1, 3, and 7 consequent days. At each time point, the supernatants were collected and used to investigate the ion release (Ti, Zr, Cu, Pd for $Ti_{40}Zr_{10}Cu_{36}Pd_{14}$) from the surface using inductively coupled plasma mass spectrometry (ICP-MS, iCAP Q, ThermoFischer).

2.5. Antibacterial evaluation

2.5.1. Strain growth condition

Bacteria were purchased from the American Type Culture Collection (ATCC, Manassas, USA). Specimens' antibacterial properties were assayed towards Aggregatibacter actinomycetemcomitans (ATCC 33384), a Gram-negative bacteria commonly responsible for oral environmental infections leading to

periodontal and peri-implant diseases). The bacteria were cultivated in trypticase soy agar plates (TSA, Sigma-Aldrich) and incubated at 37 °C until round single colonies were formed; then, a few colonies were collected and spotted into 15 ml of Luria Bertani broth (LB, Sigma-Aldrich) and incubated overnight at 37 °C under agitation (120 rpm). The day after, a fresh broth culture was prepared prior to the experiment by diluting bacteria into a fresh medium till a final concentration of 1×10^5 bacteria/ml corresponding to a spectrophotometric optical density of 0.001 at 600 nm wavelength [39]. (Spark, from Tecan, Switzerland).

2.5.2. Antibacterial activity evaluation

Antibacterial properties were assayed after 90 min (early time point) and 24 h (late time point) of direct infection. The specimens (3 mm diameter) were submerged with 200 µl of LB containing 1×10^5 bacterial cells in a 96-multiwell plate. Then in order to improve contact between bacteria and specimens, the multiwall plate was agitated by using an orbital mini shaker inside the incubator. At each time point, the LB (from Sigma-Aldrich) were gently collected from each specimen to evaluate the number of viable floating bacteria, whereas adhered bacteria were detached from specimens' surface by sonication and vortex (5 min each, 3 times). The number of viable bacteria was determined by the colonyforming unit count (CFU) as previously detailed [8], whereas the viability of adhered bacteria was evaluated by means of their metabolic activity using the resazurin colorimetric metabolic assay (alamarBlue™, ready-to-use solution from Life Technologies) by directly adding the dye solution (0.0015% in phosphate buffer saline (PBS)) onto the infected specimens. After 4 h of incubation in the dark, the fluorescent signals (expressed as relative fluorescent units – RFU) were detected at 590 nm by spectrophotometer (Spark, from Tecan, Switzerland). Moreover, the fluorescent Live/Dead assay (BacLight™, Bacterial Viability Kit for microscopy, Invitrogen) was applied to visually detect viable

colonies adhered to the sample; images were collected with an EVOS FLoid microscope (from Life Technologies). Finally, field emission scanning electron microscopy (FESEM, SUPRATM 40, Zeiss) imaging was used to detect biofilm-like colonies aggregates; briefly, specimens were dehydrated by the alcohol scale (70-80-90-100% ethanol, 1 h each), swelled with hexamethyldisilazane, mounted onto stubs with conductive carbon tape and covered with a chromium layer. Images were collected at different magnifications using secondary electrons.

2.6. In vitro cytocompatibility evaluation

2.6.1. Cells cultivation

Human gingival fibroblast cells (HGF) were purchased from PromoCell (C 12,974) and cultivated in low-glucose Dulbecco's modified Eagle medium (DMEM, Sigma-Aldrich) supplemented with 10% fetal bovine serum (FBS, Sigma-Aldrich) and 1% antibiotics at 37 °C, 5% CO2 atmosphere. Cells were cultivated until 80%–90% confluence, detached by atrypsin EDTA solution (0.25% in PBS), harvested and used for experiments.

2.6.2. Cytocompatibility evaluation

Cells were directly seeded onto specimens' surface (3mm diameter) at a defined density (2000 cells/sample), and after 4 h of allowing adhesion, 450 µl of culture media was added to each sample. Subsequently, they were cultivated for 24 and 48 h; at each time point, the viability of the cells were evaluated using metabolic activity using the resazurin metabolic assay as prior described; moreover, the fluorescent Live/Dead assay was applied to visually check for viable cells (Live/Dead, Viability/Cytotoxicity Kit for mammalian cells, Invitrogen) with a digital EVOS FLoid microscope (from Life Technologies). Finally, the morphology of cells was visually investigated by FESEM imaging.

2.7. Oral plaque prevention

2.7.1. Preparation of oral plaque

Samples of oral plaque were collected from 3 healthy volunteers by non-invasive procedures and after obtaining their informed consensus in accordance with the Declaration of Helsinki. None of them used antibiotics nor had undergone periodontal treatment during 3 months prior to sampling. Oral plaque samples were taken from supragingival parts of premolars or molars with individual sterile Gracey curettes by gently scraping. After their removal, samples were pooled and maintained in sterile cooked meat culture broth (Sigma-Aldrich). Microorganisms were dispersed by vortex and subsequently transferred in 30 ml of fresh media. After 24 h, the bacterial community of oral plaque was frozen and stored at –80 °C to preserve the starting population.

2.7.2. Bacterial consortium assessment

In order to investigate whether $Ti_{40}Zr_{10}Cu_{36}Pd_{14}$-BMG has any effect on influencing the bacterial community involved in oral plaque, the samples were submerged into 300 μl of cooked meat broth, including about 1×10^3 bacterial cells. After incubation in anaerobic conditions (by means of anaerobic Bug Box, 500 rpm and 37 °C) for 24 h, the floating planktonic bacteria were collected and pelleted by centrifuging at 5000 rpm for 20 min. In order to investigate bacterial biofilm, the samples of $Ti_{40}Zr_{10}Cu_{36}Pd_{14}$-BMG and Ti–6Al–4V were washed once with PBS solution to remove unattached bacterial cells. Then, the samples were sonicated three times (5 min followed by 20 s vortex) to detach bacterial biofilm that was pelleted as detailed for the planktonic counterpart. Moreover, bacteria-contaminated material surfaces and biofilm feature and development were visually checked by FESEM as previously described.

2.7.3. Protein extraction and digestion

Protein extraction of planktonic and biofilm was performed by adding 200 μl of lysis buffer, mainly composed of 8 M urea buffer (pH 8.5) and Tris-HCl, to both

planktonic and biofilm form samples obtained in the previous section. For the release of all bacterial cells' proteins, the samples were sonicated 6 times (each time 10 s). After protein quantification assayed by using Bradford reagent (Sigma-Aldrich), a certain volume of protein samples that equals 80 µg (threshold concentration for proteomics assay) was added to 25 µl of 100 mM ammonium bicarbonate (NH4HCO3). For protein reduction, two following solutions: 15 µl trifluoroethanol (TFE, 99%) and 2.5 µl of dithiothreitol (200 mM DTT stock solution) (Sigma-Aldrich), were added and kept at 60 °C for 30 min. Furthermore, proteins were alkylated with 10 µL of cysteine blocking reagent (Iodoacetamide, IAM, 200 mM; Sigma-Aldrich) for 30 min at room temperature in the dark and digested with trypsin (Promega, Sequence Grade) overnight at 37 °C. Trypsin activity was stopped by adding 2 µL of neat formic acid and the digests were dried by speed vacuum [40].

2.7.4. Proteomics analysis

In order to investigate the impact of Ti-BMG on bacterial consortia of oral biofilm, proteomics analysis was performed on the protein samples prepared in the previous section.

The digested peptides were analyzed with a UHPLC Vanquish system (Thermo Scientific, Rodano, Italy) coupled with an Orbitrap Q-Exactive Plus (Thermo Scientific, Rodano, Italy). Peptides were separated by a reverse phase column (Accucore™ RP-MS 100 × 2.1 mm, particle size 2.6 µm). The column was maintained at a constant temperature of 40 °C at a flow rate of 0.2 mL/min. Mobile phases A and B were water and acetonitrile, respectively, both acidified with 0.1% formic acid. The analysis was performed using the following gradient: 0–5 min from 2% to 5% B; 5–55 min from 5% to 30% B; 55–61 from 30% to 90% B and held for 1 min, at 62.1 min the percentage of B was set to the initial condition of the run at 2% and hold for about 8 min in order to re-equilibrate the

column, for a total run time of 70 min. The mass spectrometry (MS) analysis was performed in positive ion mode. The electrospray ionization source was used with a voltage of 2.8 kV. The capillary temperature, sheath gas flow, auxiliary gas, and spare gas flow were set at 325 °C, 45, 10, and 2 arb, respectively. S-lens were set at 70 rf. For the acquisition of spectra, a data-dependent (ddMS2) top 10 scan mode was used. Survey full-scan MS spectra (mass range m/z 381 to 1581) were acquired with resolution R = 70,000 and AGC target 3×10^6. MS/MS fragmentation was performed using high-energy c-trap dissociation (HCD) with resolution R = 35,000 and automatic gain control target of 1×10^6. The normalized collision energy (NCE) was set to 30. The injection volume was 3 µl. The mass spectra analysis was carried out using Mascot v.2.4 (Matrix Science Inc., Boston, USA): the digestion enzyme selected was trypsin, with 2 missed cleavages, and a search tolerance of 10 ppm was specified for the peptide mass tolerance, and 0.1 Da for the MS/MS tolerance. The charges of the peptides to search for were set to 2+, 3+, and 4+, and the search was set on monoisotopic mass. The following modifications were specified for the search: carbamidomethyl cysteines as fixed modification and oxidized methionine as variable modification. The Human Oral Microbiome Database V3 was used, and a target-decoy database search was performed. False discovery rate was fixed at 1% [41]. Peptides were mapped to their respective taxa of origin using Unipept [42].

2.8. Statistical analysis of data

Experiments were performed in triplicate. Results were statistically analyzed using the SPSS software (v.20.0, IBM, USA). First, data normal distribution and homogeneity of variance were confirmed by the Shapiro-Wilk's and the Levene's test, respectively; then, groups were compared by the one-way ANOVA using the Tukey's test as post-hoc analysis. Significant differences were established at $p < 0.05$.

3. Results and discussion

3.1. Materials properties evaluation

Fig. 1 shows images of (a) the casting set-up and (b) the outer surface appearance of the cast rods of 3 mm in diameter. Fig. 1c displays the differential scanning calorimetry (DSC) data obtained from the cast alloy. The curve exhibits an endothermic event, characteristic of glass transition to supercooled liquid, followed by exothermic reactions corresponding to crystallization of the supercooled liquid. The glass exhibits two exothermic peaks associated with a two-stage crystallization. X-ray diffraction (XRD) of $Ti_{40}Zr_{10}Cu_{36}Pd_{14}$ shown in the inset signifies a glassy nature, which is confirmed by transmission electron microscopy (TEM) studies (Fig. 4). Neither crystals nor any features (i.e., defects, shear bands, or nanocrystals) are observed throughout the sample, which corroborates the amorphous state of the as-cast BMG.

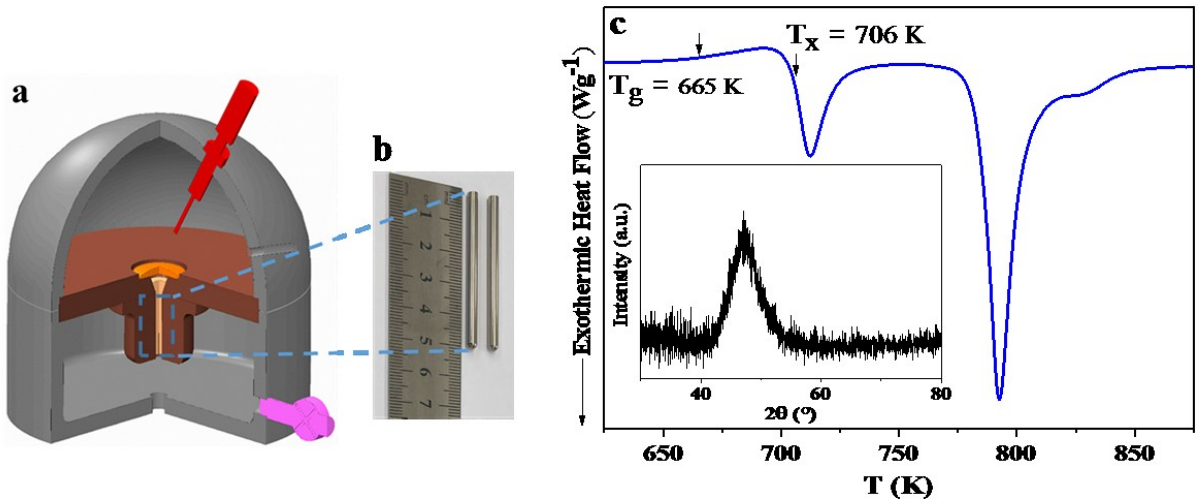

Fig. 1. (a) 3D demonstration of an arc melter suction casting (b) The produced $Ti_{40}Zr_{10}Cu_{36}Pd_{14}$ BMG (c) DSC analysis together with the XRD data of the as-cast sample in c-inset.

BMG in many biomedical applications requires a net-shape manufacturing process. The large resistance of BMG to crystallization results in an accessible supercooled liquid region (SCLR) on a convenient time scale for processing. This allows for a net-shape process, where the BMG behaves like a plastic [43–46]. It means, the sluggish crystallization kinetics in the SCLR confers a promising net-

shape processing route, by which the material can be deformed within a much longer time window [35,36,47]. In this regard, the structural relaxation and crystallization behavior of glasses exposed to thermomechanical driving forces merit in-depth exploration. Fig. 2 illustrates the dynamic mechanical analysis (DMA) and thermal expansion (TE) results of the as-cast $Ti_{40}Zr_{10}Cu_{36}Pd_{14}$ glass investigated under compression. The storage modulus (G'), the loss modulus (G''), and thereby the loss factor (tan δ) of Ti-based BMG are, in general, sensitive to the applied frequency. To assess the influence of frequency on the thermo-mechanical response, specimens were tested in compression mode employing a fixed heating rate of 10 K/min at various frequencies. Fig. 2 (a), (b), and (c) present respectively the evolution of G', G'', and tan δ in $Ti_{40}Zr_{10}Cu_{36}Pd_{14}$ at three different testing frequencies (0.1–1–10 Hz). Although the frequency does not seem to affect the characteristic temperatures, the glass transition and crystallization events are mitigated as the frequency varies from 0.1 to 10 Hz. This suggests that 0.1 Hz can involve larger groups of atoms to respond in a more intense oscillation way, whereas with higher frequencies, a larger thermo-mechanical driving force is required to visualize the effects, which can be considered a disadvantage. The glass transition temperature (T_g) and crystallization temperature (T_x) are registered from G'' and tan δ. The peak maximum of the hump exhibited in the α region of the G'' can be addressed to the T_g (654 ± 1 K). G00 increases as the temperature approaches the onset of crystallization (T_{x1} = 709 ± 1 K). After 709 K, the first crystallization sets in, and thus it drops drastically to a minimum at 734 ± 1 K, followed by variations in the evolution of G'' and a second rise afterwards as the temperature reaches 791 ± 1 K, there the second crystallization takes place and G'' drops again. G' of 0.1 develops an evident shoulder as the temperature ranges from 382 ± 1 K – 416 K, indicating a clear relaxation. G' decreases afterwards from 92 ± 1 GPa gradually to 70 ± 1 GPa at 578 ± 1 K, followed by a plateau till T_g. G' rises and heads up with 90° at the onset of crystallization temperature to 137 ± 1 GPa and afterwards

with variations in values further to 193 ± 1 GPa at 822 ± 1 K. Fig. 2 (d) shows the corresponding dilatometer trace. The dilatation curve is linear at lower temperatures until the onset of structural relaxation at 493 ± 1 K, where the thermal expansion starts to counteract the contraction, which saturates around 550 ± 1 K. The ordinate signal remains more or less constant during the transition into the supercooled liquid state, and thereafter until the first crystallization is reached, which is indicated by a step-like drop in the signal within 709 ± 1 – 724 ± 1 K. Afterwards, the glass continues to expand obeying nearly the same thermal expansion coefficient as below 493 K. A further penetration step occurs at 791 ± 1 K as the glass crystallizes in the second stage till 812 ± 1 K. These observations elucidate the processing range, in which the considered Ti-based glass can be thermomechanically shaped to implants [48–50].

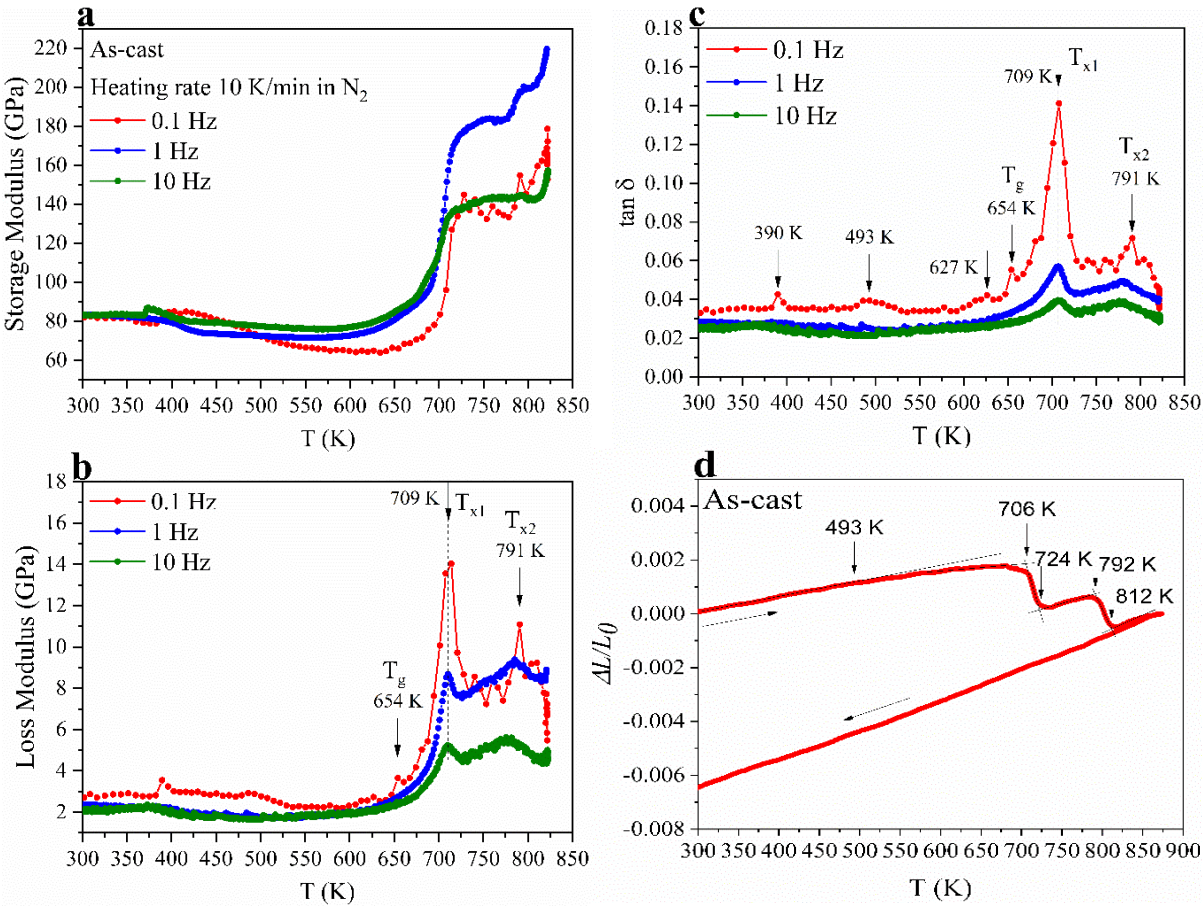

Fig. 2. DMA and TE data of the as-cast samples; (a) Storage modulus (G'), (b) loss modulus (G''), (c) loss factor (tan δ), and (d) thermal expansion of $Ti_{40}Zr_{10}Cu_{36}Pd_{14}$ BMG as a function

of temperature. The heating rate was 10 K/min, and the DMA measurement frequencies were 0.1–1–10 Hz.

Static water contact angle measurements were conducted via the sessile drop method on the etched surface of as-cast $Ti_{40}Zr_{10}Cu_{36}Pd_{14}$ BMG and Ti–6Al–4V, and the same test was repeated on their surface after incubation in a water medium for 48 h at 37 °C, and rpm = 120. The results are shown in Fig. 3. According to this figure, the water contact angle for both etched samples is in the same range of values. The purpose of etching was to remove any unwanted oxide layer caused during casting. However, after 48 h incubation in water, the hydrophilicity of Ti–6Al–4V increases significantly while the water contact angle for $Ti_{40}Zr_{10}Cu_{36}Pd_{14}$ BMG remains the same. Previous studies show that the formation of the TiO2 layer on Ti–6Al–4V can significantly increase its surface wettability [51]. There are two possibilities to explain this phenomenon. $Ti_{40}Zr_{10}Cu_{36}Pd_{14}$ BMG is much more resistant to oxidation compared with Ti–6Al–4V. Therefore, the extent of oxidation for Ti–6Al–4V after 48 h is expected to be much more significant than $Ti_{40}Zr_{10}Cu_{36}Pd_{14}$ BMG. Furthermore, depending on the type of the oxide layer, the wetting behavior is expected to be different. The oxidation behavior of Ti–6Al–4V is very well-studied, and it is a fact that the formation of TiO2 on Ti–6Al–4V improves the surface wettability significantly [52]. On the other hand, the oxide layer forming on $Ti_{40}Zr_{10}Cu_{36}Pd_{14}$ BMG could be TiO_2, Cu_2O, or ZrO_2. In the case of Cu_2O formation, the oxide layer is studied to have a hydrophobic to the superhydrophobic surface, and therefore, if it is partially formed on $Ti_{40}Zr_{10}Cu_{36}Pd_{14}$ BMG, it would not improve the surface wettability [53]. A similar outcome is expected from ZrO_2. Therefore, further investigation is required to identify the type of oxide layer formed on $Ti_{40}Zr_{10}Cu_{36}Pd_{14}$ BMG.

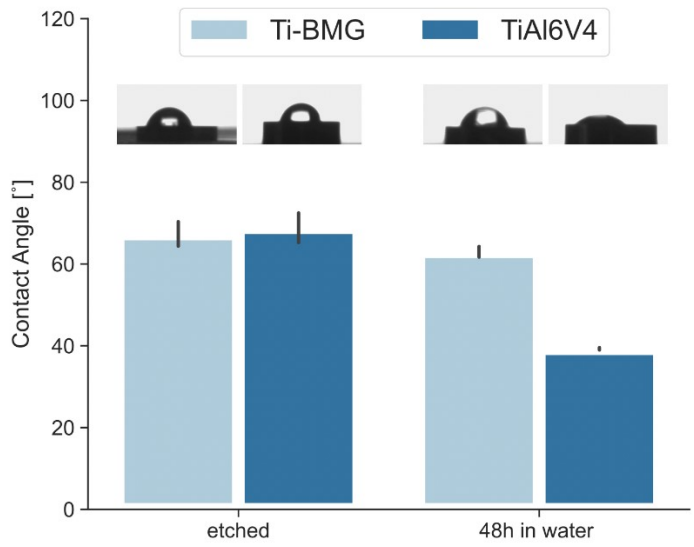

Fig. 3. Water contact angle measurements on $Ti_{40}Zr_{10}Cu_{36}Pd_{14}$-BMG (referred to as Ti-BMG for short) and Ti–6Al–4V after etching and after 48 h incubation in water at 37 °C, rpm = 120.

The surface of $Ti_{40}Zr_{10}Cu_{36}Pd_{14}$ was further analyzed by HRTEM, and its results are presented in Fig. 4. Since the surface is an important contributor to the antifouling properties of the alloy, specific attention is paid to distinguishing between the surface of the alloy in comparison with its interior. Fig. 4a shows the TEM picture of the sample's crosssection and the surface, and the interior part of BMG is marked. While the sample interior is fully amorphous, as shown in Fig. 4b and inset, a 15 nm thin surface region was identified, showing a mixed amorphous and nanocrystalline structure in Fig. 4c, as confirmed by the selected area diffraction (SAD) patterns in the inset of 4c, respectively. The lattice distance in crystalline surface area was measured to be 0.22 nm.

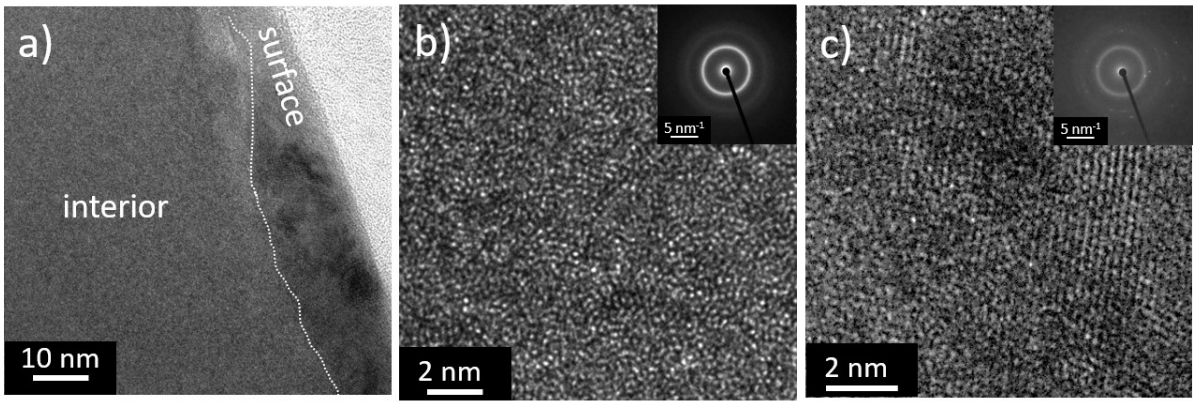

Fig. 4. HR-TEM images comparing the structure of the interior and the surface of the as-cast $Ti_{40}Zr_{10}Cu_{36}Pd_{14}$ glass; (a) overview, (b) close-up of the fully amorphous interior, and (c) close-up of the surface region showing nanocrystals embedded in an amorphous matrix.

The elemental distribution of both regions was determined using STEM-EDX, as shown in Fig. 5. From the elemental maps in Fig. 5a significant change in elemental compositions between the interior of the glass and its surface can be seen. Fig. 5b shows an EDX line scan to quantify the change of composition, showing an increase of oxygen and copper in the 15 nm thin surface region and a decrease of Ti, Zr, and Pd, corroborating the possible copper oxide formation. Since O is also detected in this analysis, and Pd is a noble metal, the oxide surface layer can be deduced to be copper oxide predominantly.

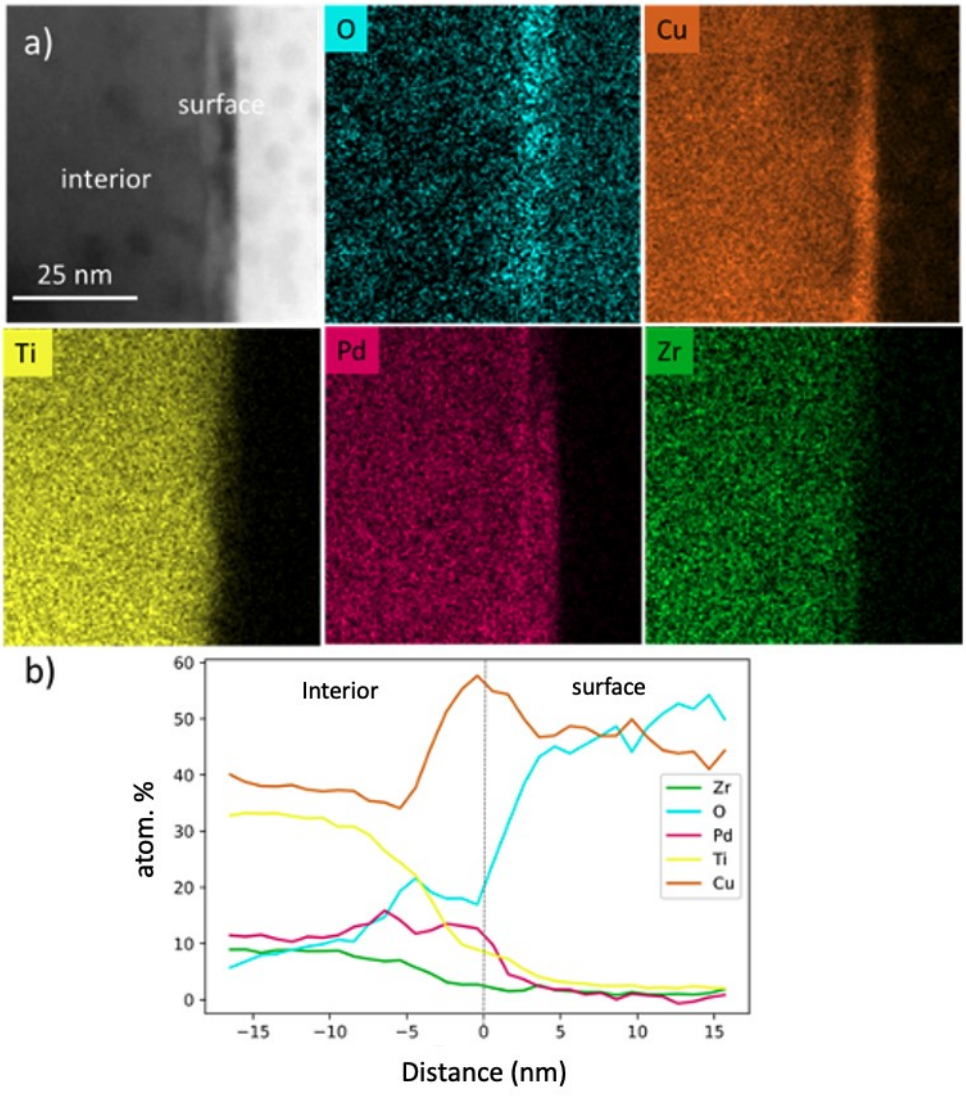

Fig. 5. TEM-EDX analysis showing a change of the elemental composition between interior and surface of the as-cast $Ti_{40}Zr_{10}Cu_{36}Pd_{14}$ glass (a) elemental maps of O, Cu, Ti, Pd, and Zr and (b) line-scan across the transition between the interior and surface region.

Further surface analysis on as-cast $Ti_{40}Zr_{10}Cu_{36}Pd_{14}$ was conducted by XPS and is shown in Fig. 6a. According to this graph, there must be at least a very thin oxide layer must be present on the samples surface, evidenced by the O1s and OKLL peaks [54]. The binding energy peak position of the O1s are: As-cast – 529 ± 1 eV, as-cast after ion etch – 529 ± 1 eV, after incubation in water for 48 h _ 531 ± 1 eV, after incubation in artificial saliva for 48 h – 532 ± 1 eV. Sample surface was ion-etched, and the XPS analysis was repeated (see Fig. 6b), showing similar results. In both spectra, the principal peaks of titanium (Ti2s, Ti2p), oxygen (O1s), zirconium (Zr3d), copper (Cu2p), and palladium are revealed. Cu 2p peaks correspond to the CuO, supporting the TEM findings [51].

The carbon is mainly due to surface contamination, and after etching, it almost disappeared. The as-cast samples were also incubated in water for 48 h at 37 °C, rpm = 120, and their XPS analysis is shown in Fig. 6c. In this figure, the main carbon and oxygen peaks dominate the whole spectra. New sodium peak at around ~500 kV is due to the adsorbed ions on the surface of the metallic glass. Ultimately, since $Ti_{40}Zr_{10}Cu_{36}Pd_{14}$ will be utilized as oral implants, the same incubation procedure was repeated on them, this time in artificial saliva (Fig. 6d). The full composition of artificial saliva is presented in supplementary material. According to this figure, the main peaks are carbon and oxygen, suppressing all other peaks from the metallic glass compositions. The composition of artificial saliva is based on organic compounds, and therefore, it is expected to have the adhered layer showing mainly carbon and oxygen as main peaks.

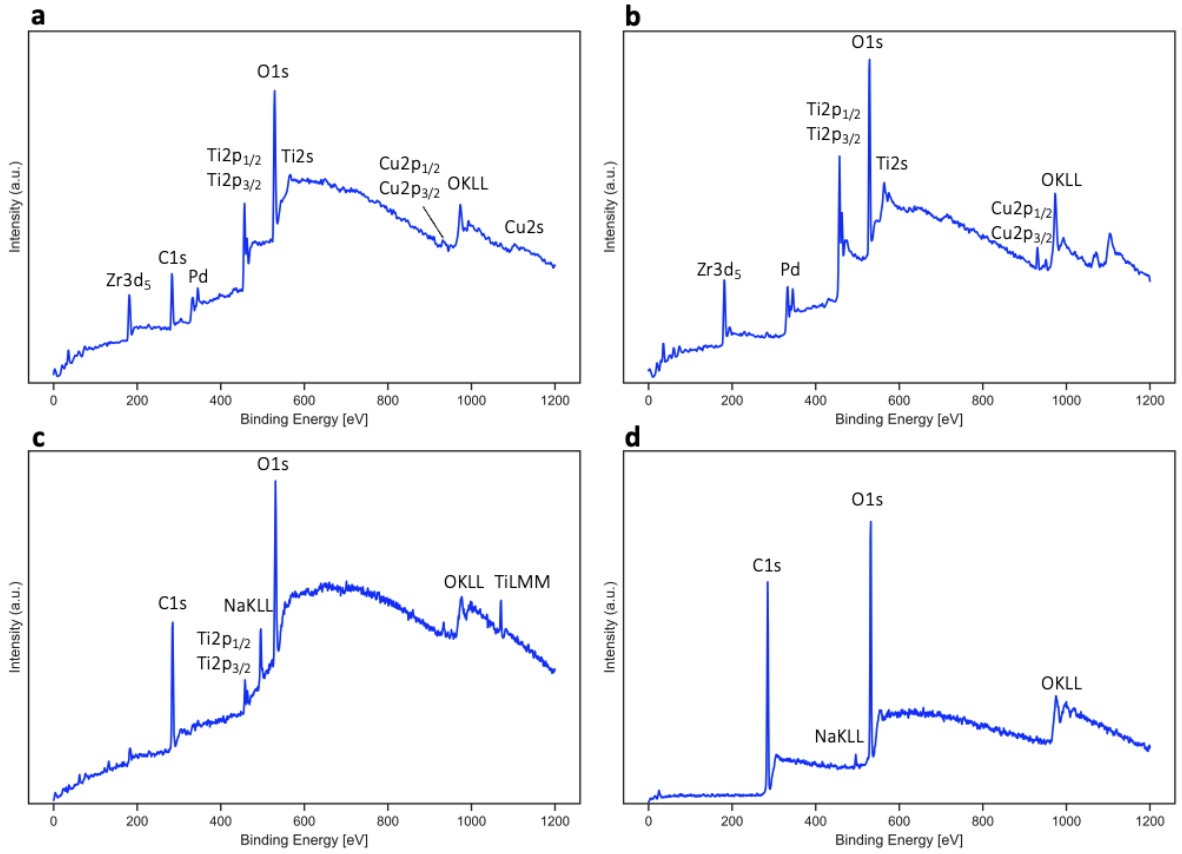

Fig. 6. XPS analysis of $Ti_{40}Zr_{10}Cu_{36}Pd_{14}$ BMG surface for the (a) as-cast sample (b) ion-etched as-cast sample (c) after incubation in water for 48 h at 37 °c, rpm = 120, (d) after incubation in artificial saliva for 48 h at 37 °c, rpm = 120.

3.2. Antibacterial activity evaluation

In this study, the oral pathogen Aggregatibacter actinomycetemcomitans was selected due to its widespread pathogenic potency in intraoral infection with particular involvement in the oral biofilm development [55,56]. The aim of this study was to investigate whether the $Ti_{40}Zr_{10}Cu_{36}Pd_{14}$-BMG holds antifouling properties by reducing the number of adhered bacteria at the 90 min early-stage or antibacterial properties, thus being able to reduce the number of proliferating bacteria and the amount of biofilm-like 3D structures at the late 24 h time point [57]. Both metabolic (alamarBlue, CFU count) and visual approaches (Live/Dead, FESEM) have been exploited to evaluate the specimens' performances. Results are summarized in Fig. 7. Prior to the tests, the FESEM investigation shows that the surface of $Ti_{40}Zr_{10}Cu_{36}Pd_{14}$-BMG and the Ti–6Al–

4V control were relatively the same, which were polished with the same protocol (Fig. S1 in the Supplementary data file).

In Fig. 7a, the density of the viable colonies adhered to the specimens' surface are given after early (90 min) and late (24 h) time points by the fluorescent Live/Dead assay (viable bacteria stained in green). After 90 min (upper panel), the density and the distribution of the viable bacteria onto specimens' surface was comparable between BMG and controls; therefore, an apparent antifouling activity of the BMG preventing bacteria adhesion was not observed. Therefore, the physical-chemical properties of the test materials are not suitable for preventing bacterial adhesion, as well as the lack of ions release (mainly Cu) deprived specimens of a possible defense mechanism. However, moving to the 24 h results (lower panel), the density and the distribution of viable bacterial results are highly reduced on the $Ti_{40}Zr_{10}Cu_{36}Pd_{14}$-BMG surfaces in comparison to the Ti–6Al–4V controls, thus suggesting a killing activity exploited in the function of time. Moreover, some 3D biofilm-like aggregates were observed in the Ti–6Al–4V specimens, whereas only single random colonies were detectable for the $Ti_{40}Zr_{10}Cu_{36}Pd_{14}$-BMG ones. The same visual confirmations were achieved by FESEM images (Fig. 7-b); random single colonies were observed after 90 min for both specimens, but after 24 h, numerous biofilm-like aggregates were detected on control surfaces while mainly single ones were still present on the $Ti_{40}Zr_{10}Cu_{36}Pd_{14}$-BMG test specimens.

Fluorescent and FESEM images were confirmed by the count of the viable colonies (CFU, Fig. 7-c) detached from the specimens' surface; after 90 min, 7.5×10^1 and 5×10^1 colonies were counted for Ti–6Al–4V and $Ti_{40}Zr_{10}Cu_{36}Pd_{14}$-BMG, respectively. However, after 24 h, the number of living bacterial colonies on the surface of Ti–6Al–4V showed a significant increase ($p < 0.05$), approximately ~8 times more than the ones attached to $Ti_{40}Zr_{10}Cu_{36}Pd_{14}$-BMG ($28.5 \times 10^3$ vs. 3×10^3, respectively) as summarized in Table 1.

Table 1: Number of viable colonies (CFU) of A. actinomycetemcomitans attached to the sample surface after 90 min and 24 h of infection. Results represent means ± deviation standard.

Samples	Adhered CFU count	
	After 90 min (x10^1)	After 24 h (x10^3)
Ti-6Al-4V	7.5 (±2.5)	28.5 (±0.5)
Ti-BMG	5 (±0.0)	3 (±0.0)[a]

[a] = $p<0.05$ vs Ti-6Al-4V

As a logical consequence of the reduction of the number of viable colonies showed by the CFU count, when the metabolic activity of the bacteria colonizing specimens' surface was measured by the Alamar blue assay (Fig. 7d), a significant reduction ($p < 0.001$, representing ≈70%) was obtained for the $Ti_{40}Zr_{10}Cu_{36}Pd_{14}$-BMG specimens in comparison with the control ones.

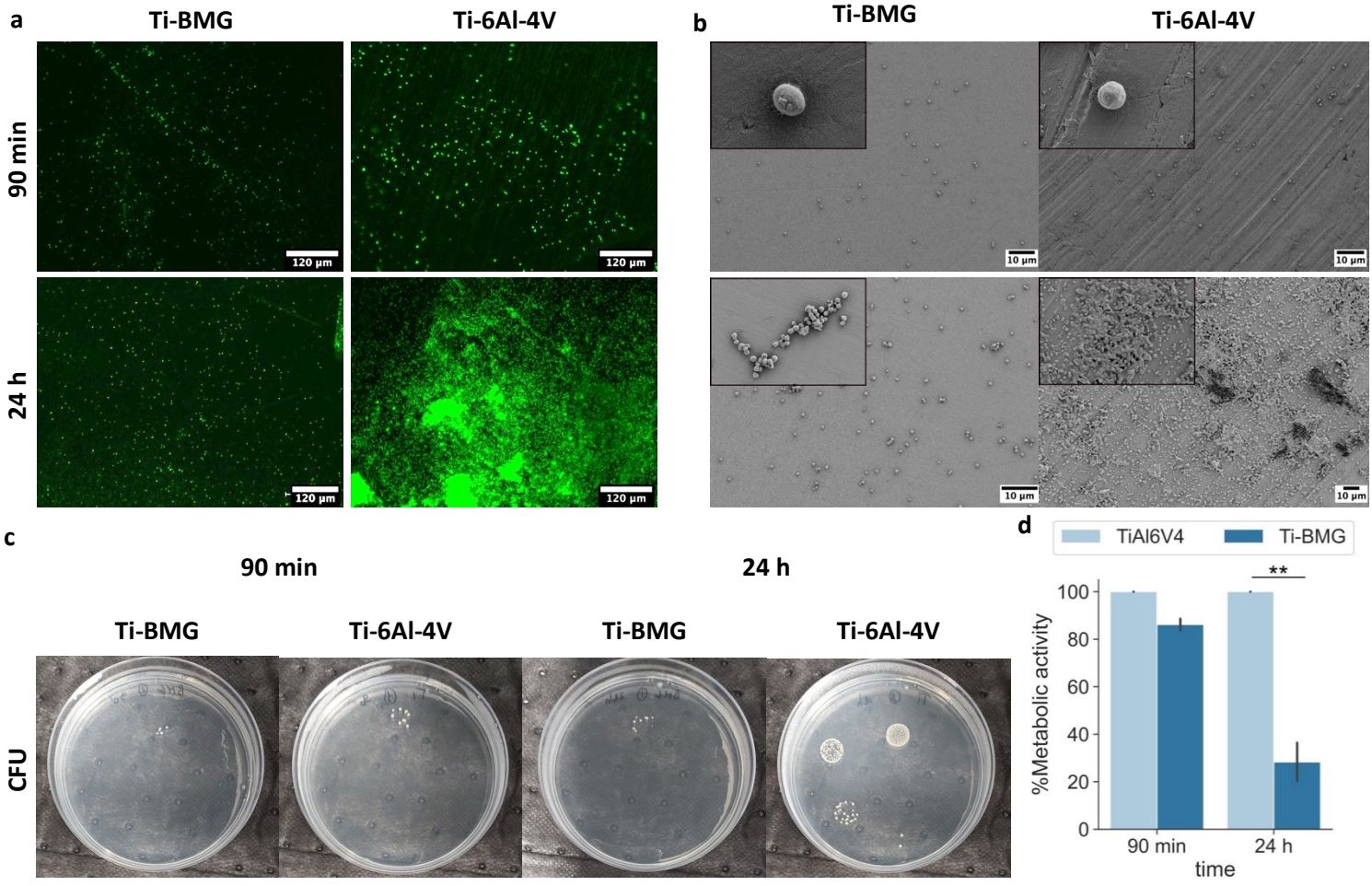

Fig. 7. Antibacterial test to assess antiadhesive and antibacterial properties of $Ti_{40}Zr_{10}Cu_{36}Pd_{14}$-BMG (referred to as Ti-BMG for short) and Ti–6Al–4V on aerobic bacterial strain, A. actinomycetemcomitans: (a) Live/Dead assay on the surface of samples after 90 min and 24 h incubation time; (b) SEM images after 90 min and 24 h of direct contact. (c) Colony-forming unit (CFU) after 90 min and 24 h incubation time. (d) % Metabolic activity on samples' surface

after 90 min and 24 h incubation time. The values are normalized with respect to Ti–6Al–4V as a control for each time point (** indicates p-value <0.01).

Such a significant difference in terms of antibacterial activity on the surface of two inert Ti-based alloys ($Ti_{40}Zr_{10}Cu_{36}Pd_{14}$-BMG and Ti–6Al–4V) can find the first explanation according to their oxidation range. As previously seen in Fig. 3, the incubation of Ti–6Al–4V in water (or, in this case, a water-based medium) could decrease the water contact angle significantly on Ti–6Al–4V. Wang et al. [58] have previously shown that the oxidation of Ti–6Al–4V significantly increases its wettability. In fact, when the aim is to enhance the proteins and cells' attachment to the Ti–6Al–4V surface, oxidation of the surface can be exploited as a complementary strategy [52]. On the other hand, HRTEM analysis conducted on $Ti_{40}Zr_{10}Cu_{36}Pd_{14}$-BMG reported in Fig. 4 shows the formation of a nanometers-thick layer of copper oxide representing a hydrophobic-to-superhydrophobic surface. Therefore, the surface wettability is not improved even after partial surface oxidation. Many research analyses on the interaction of bacteria with materials surfaces have indicated that bacteria attachment on the surface increases when the surface is more hydrophilic and this is the reason why many efforts have been conducted on the development of superhydrophobic surfaces to prohibit the early bacterial attachment [5].

Another possible explanation of the $Ti_{40}Zr_{10}Cu_{36}Pd_{14}$-BMG killing activity can be ascribed to the Cu layer formed in the superficial zone as reported in Figs. 4 and 5. In fact, copper represents a well-known ion holding antibacterial properties: it is of pivotal importance for bacterial metabolisms by regulating the activity of many enzymes such as tyrosine and dopamine that require copper as donor/receptor [59]. Therefore, the coordination of copper can be exploited through a Fenton chemistry route to introduce highly reactive radicals such as hydroxyl groups (ROS), causing oxidation of proteins and lipids [60]. In this scenario, as previously discussed by the Authors [61] once bacteria try to adhere

to the specimens' surface, they expose the [4Fe–4S] clusters of proteins in order to coordinate iron exchange that is crucial for the metabolic activity. The presence of copper results in a direct impairment of the [4Fe–4S] clusters leading to the release of Fenton-active Fe in the cytoplasm, where toxic ROS accumulate, and this brings bacteria to death.

3.3. Cytocompatibility evaluation

The cytocompatibility of $Ti_{40}Zr_{10}Cu_{36}Pd_{14}$-BMG specimens was investigated preliminary in vitro on Human gingival fibroblast (HGF) cells. HGF cells were selected as a representative of the soft tissue responsible for the device sealing in the peri-implant region; here, the positive cells' repopulation of the device regulates the pro-inflammatory cascade activation [39] as well as represents a physical hurdle for bacteria invasion. Accordingly, HGF cells were directly seeded on the samples' surfaces, and after 24 and 48 h, the viability and the morphology of adhered and spread cells were determined by Live/Dead and SEM imaging as reported in Fig. 8a and b, respectively, a representative for 24 h cultivation. Results from SEM demonstrated that the cells were able to successfully adhere and spread onto both the control Ti–6Al–4V and test $Ti_{40}Zr_{10}Cu_{36}Pd_{14}$-BMG surfaces, while the Live/Dead assay confirmed that such cells were viable and that their confluence was comparable to the control. So, the test BMG surfaces were confirmed to be cytocompatible towards HGF. Later, the viability of the cells was further evaluated employing the metallic activity using the resazurin (Alamar blue) assay; results are reported in Fig. 8c. As a confirmation of the images from fluorescence and SEM, the metabolism of cells resulted as comparable between control ad test BMG at both 24/48 h time-points; a slight increase was observed for the BMG after 48 h, but the values resulted as not significant in comparison to the control ($p > 0.05$); this is a promising finding based on the pivotal role played by fibroblasts in the early sealing step and the previous results showing a strong antibacterial effect (Fig. 7), meaning that the

amount of Cu exposed at the materials' interface is sufficient to prevent bacterial colonization, but it is not toxic for human cells colonizing the device. Indeed, to confirm that the Cu is not released from the surface into the solution, the ion-release test was conducted by submerging samples into artificial saliva solutions for 1,3 and 7 consequent days. Fig. 8d shows that the amount of the released Cu into the solution is at its peak after 3 days of submersion, but its maximum concentration is below 12 ppb. It has been previously shown that a minimum concentration of 250 ppm Cu in the solution is required to induce any effect on cells or bacteria [62].

In general, these results are in line with previous literature. Kaushik et al. reported about cytocompatibility of metallic glass thin films (TiCuNi) applied onto Si substrate upon exposure to muscle cells, allowing for successful adhesion, spread, and proliferation [63]. Similarly, Liens et al. showed similar biological performances between $Ti_{40}Zr_{10}Cu_{36}Pd_{14}$-BMG and Ti–6Al–4V when human osteoblasts (MG63 osteosarcoma cells) or dermal fibroblast (primary cells from human derma) were cultivated in direct contact onto those surfaces [64].

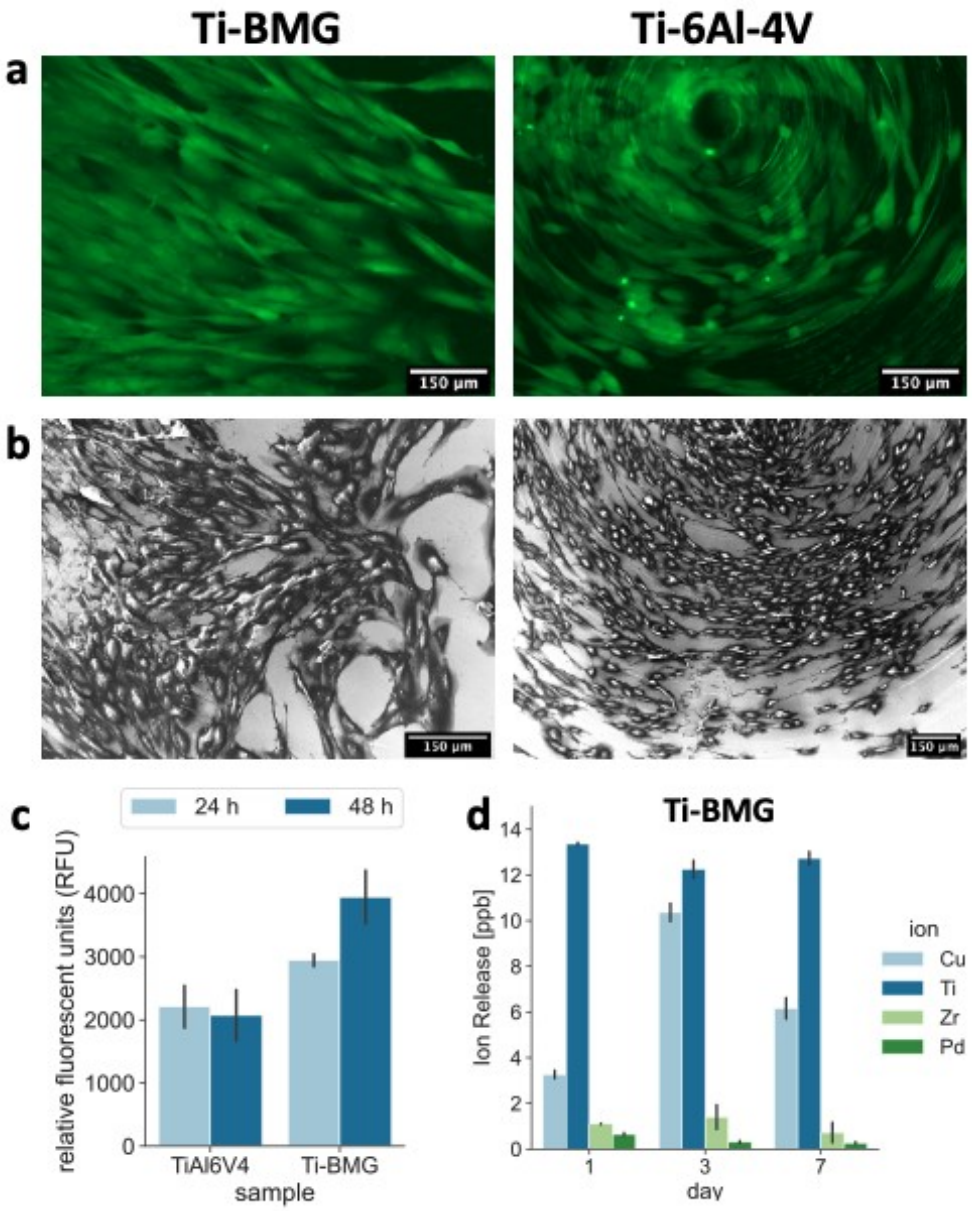

Fig. 8. Cytocompatibility evaluation of $Ti_{40}Zr_{10}Cu_{36}Pd_{14}$ -BMG and Ti–6Al–4V. HGF cells were cultivated directly on samples surface for 24 and 48 h, and the cytocompatibility was evaluated by: (a) Live/Dead images after 24 h, (b) SEM images of attached cells on the samples' surfaces, (c) Metabolic activity after 24 and 48 h. Ti–6Al–4V is used as control sample; differences between $Ti_{40}Zr_{10}Cu_{36}Pd_{14}$-BMG and Ti–6Al–4V were not significant (p-value >0.05), and (d) Ion-release measured by ICP-MS from $Ti_{40}Zr_{10}Cu_{36}Pd_{14}$-BMG after submersion into artificial saliva solution for 1, 3, and 7 days (T = 37 °C, rpm = 120).

3.4. Oral biofilm investigation

After validating $Ti_{40}Zr_{10}Cu_{36}Pd_{14}$-BMG specimens cytocompatibility and antibacterial activity towards the single strain A. actinomycetemcomitans, the ability of such innovative materials to prevent infections in the oral environment

was tested by using a fresh sample of oral biofilm collected from healthy donors. Oral biofilm is a complex multispecies community composed of microorganisms from multiple pathogenic and non-pathogenic bacteria as well as fungi. So, it can be expected that different implant materials perform differently in contact with oral biofilm, and each promotes selective adherence during early biofilm formation [65]. Based on these premises, in this work, as a next step, the samples' behavior was tested on the oral biofilm, including a number of bacterial communities with complicated interactions between them.

Fig. 9 shows the FESEM pictures taken from 24 h of incubation of samples inside a harvested oral biofilm. Fig. 9a shows the surface of $Ti_{40}Zr_{10}Cu_{36}Pd_{14}$-BMG where parts of the surface are covered by the oral biofilm. The biofilm, however, does not appear to be continuous to cover the whole surface. Higher magnification FESEM pictures show very sparse and slim biofilm growing on the surface so that single colonies of different bacterial species are properly distinguishable. Moving to Fig. 9b, the massive biofilm on the Ti–6Al–4V is clearly reported. A higher resolution picture of the biofilm shows that an extremely thick and dense layer of biofilm formed and fully covered the implant's surface; hence, in most parts of the surface, protrusions of bacterial biofilm are apparent. Unlike $Ti_{40}Zr_{10}Cu_{36}Pd_{14}$-BMG, the distinction between single colonies is difficult. As the obtained results of antibacterial activity showed on the surface of $Ti_{40}Zr_{10}Cu_{36}Pd_{14}$-BMG, a Cu-rich oxide layer with 15 nm thick was formed, and as a result, surface properties turned into a hydrophobic-to-superhydrophobic one; so, a sparse layer of biofilm on the samples' surfaces can be justified. In contrast, the surface of the Ti–6Al–4V turned into a hydrophilic due to the formation of a single layer of Ti oxides.

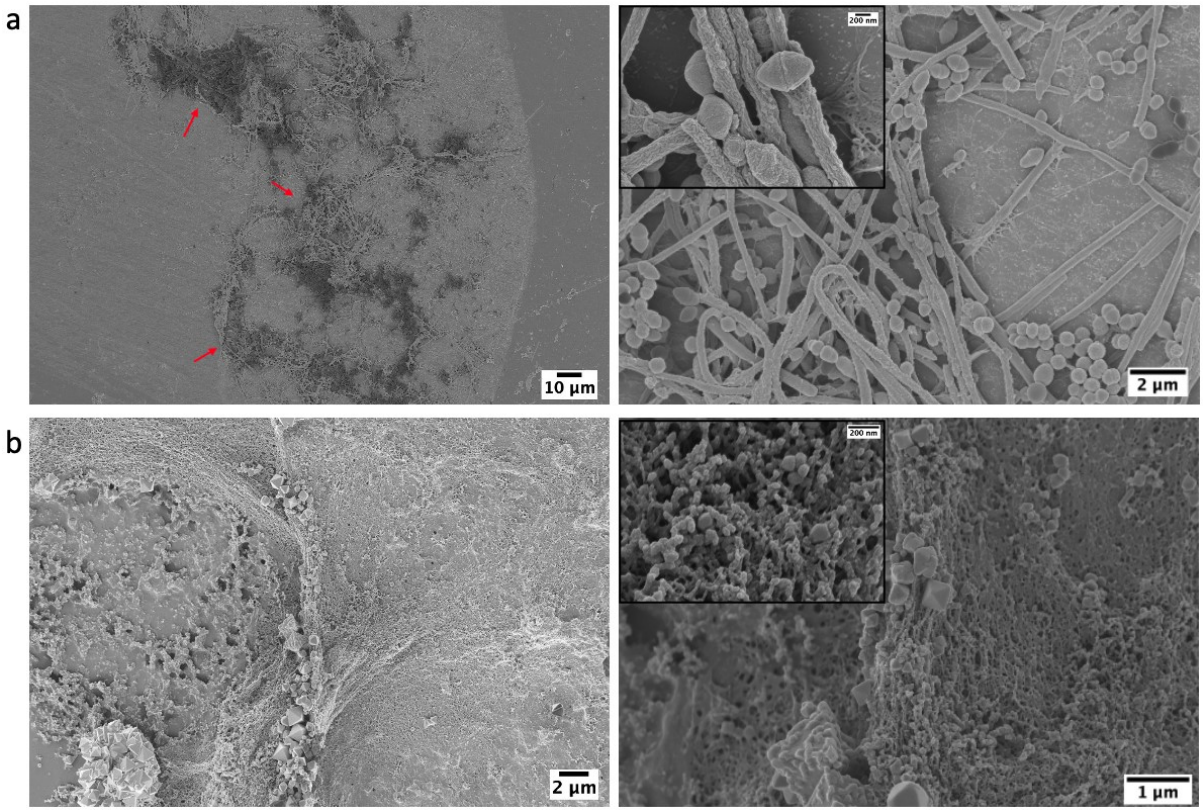

Fig. 9. FESEM pictures on (a) oral biofilm on $Ti_{40}Zr_{10}Cu_{36}Pd_{14}$-BMG after 24 h incubation and (b) oral biofilm on Ti–6Al–4V.

Further experiments to assess any change or shift of bacterial communities in the oral biofilm during incubation on the $Ti_{40}Zr_{10}Cu_{36}Pd_{14}$-BMG surface in comparison to Ti–6Al–4V were carried out by proteomics. The extraction of proteins was done in both planktonic and biofilm forms (detailed in section 2.7), and their concentration was first determined with the quantitative Bradford assay. Because of the very small size of the samples (3mm diameter), the concentration of extracted proteins in the biofilm form was much less than the limit concentration of proteomics (<80 µg). So, the proteomics assay was doable only for the planktonic form. Fig. 10 shows the prevalence of different oral bacterial phyla in the planktonic form (referred to as PF, detailed information on the prevalence of bacterial species in oral biofilm showed in Fig. S2 in the Supplementary data file). According to this result, the most prevalent bacterial phylum is Firmicutes, 85% and 87% for Ti–6Al–4V and $Ti_{40}Zr_{10}Cu_{36}Pd_{14}$-BMG,

respectively. They are Gram-positive bacterial strain mainly found as normal flora in the human intestine [66]. As reported in research, the oral microbiome found in healthy people as the human microbiome containing the phyla Firmicutes, Proteobacteria, Actinobacteria, Bacteroidetes and Fusobacteria [67]. Although the Actinobacteria phylum represents a small percentage of oral and gut microbiota, they are considered interesting phyla due to their role in some gastrointestinal and systemic diseases [68].

Despite an evident difference in terms of biofilm accumulation on the surface obtained by the SEM quantitative analysis, qualitative results from proteomic did not reveal significant shifts of populations within the oral biofilm community, with minimum differences between biofilm in contact with Ti–6Al–4V controls and $Ti_{40}Zr_{10}Cu_{36}Pd_{14}$-BMG test ones (≈1% for Bacteroidetes and Proteobacteria). Taking into account that oral biofilm sampling was performed from healthy donors presenting an oral physiological condition (intended as free from any pathological condition), these results can be interpreted as the ability of the samples to prevent biofilm colonization without causing impairments on its physiological composition.

However, to better understand the role of the $Ti_{40}Zr_{10}Cu_{36}Pd_{14}$-BMG in preventing oral biofilm formation as the future perspective we plan to i) improve the specimens' manufacture to obtain a sufficient area to screen the adhered biofilm by proteomics and ii) extend the analysis to oral biofilm obtained from pathological patients (such as periodontitis or gingivitis cases).

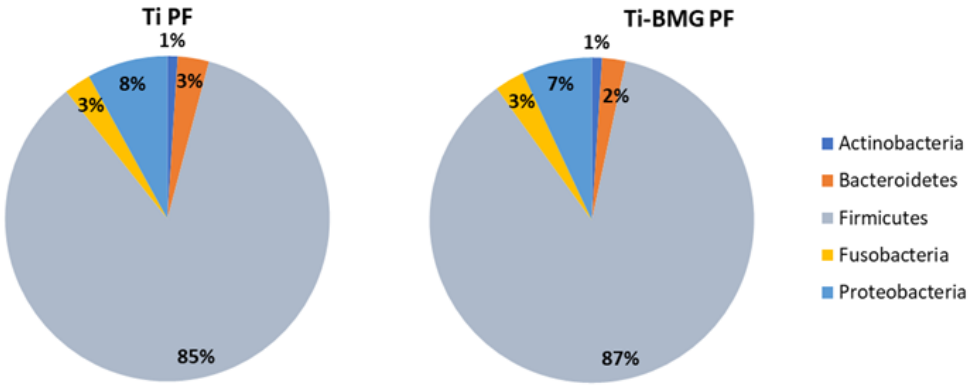

Fig. 10. Distribution of bacterial phyla in a planktonic form in oral biofilm done by proteomics analysis (Detailed information of bacterial species prevalence shown in Fig. S2 in supplementary data). PF indicates planktonic form.

4. Conclusions

This work decodes the intrinsic nature of $Ti_{40}Zr_{10}Cu_{36}Pd_{14}$-BMG targeted for biomedical oral implants. Casting 3 mm diameter rods of the given composition can generate a fully amorphous glass, as confirmed by an HRTEM study. The viscoelastic behavior of $Ti_{40}Zr_{10}Cu_{36}Pd_{14}$-BMG is manifested via dynamic mechanical analysis upon compression. At temperatures below the glass transition, the considered glasses deform primarily elastic, and the material responds independently of the testing frequency. A driving frequency of 1 Hz is conducive to visualizing the supercooled liquid region. Instead of the TiO_2 surface oxide in Ti–6Al–4V, the formation of CuO on the Ti-BMG, according to the TEM and XPS analyses, reduces the bacterial metabolic activity of the oral pathogen A. actinomycetemcomitans while increasing the cytocompatibility of the fibroblasts responsible for the device sealing on soft tissues. Finally, the formation of harmful oral biofilm is reduced, whereas its composition in bacterial communities was not changed for samples obtained from healthy volunteers.

Credit author statement

AR contributed to methodology, writing original draft, ES contributed to conceptualization, methodology and writing original draft, AL contributed to experimental investigation and discussion, VS contributed to experimental investigation and discussion, CG contributed to experimental investigation, FS contributed to discussion, WS provided resources and contributed to discussion, ZN contributed to biological analysis and writing original draft, AC contributed to the editing, review, discussion, and validation of biological analysis, AS contributed to biological analysis, LR contributed to discussion and validation, MM contributed to proteomics analysis, JE supervised the study, provided resources, reviewed and edited the draft, and acquired the funding source. BS contributed to methodology, provided resources, contributed to writing original draft, supervised the study, and acquired the funding source.

Supplementary data

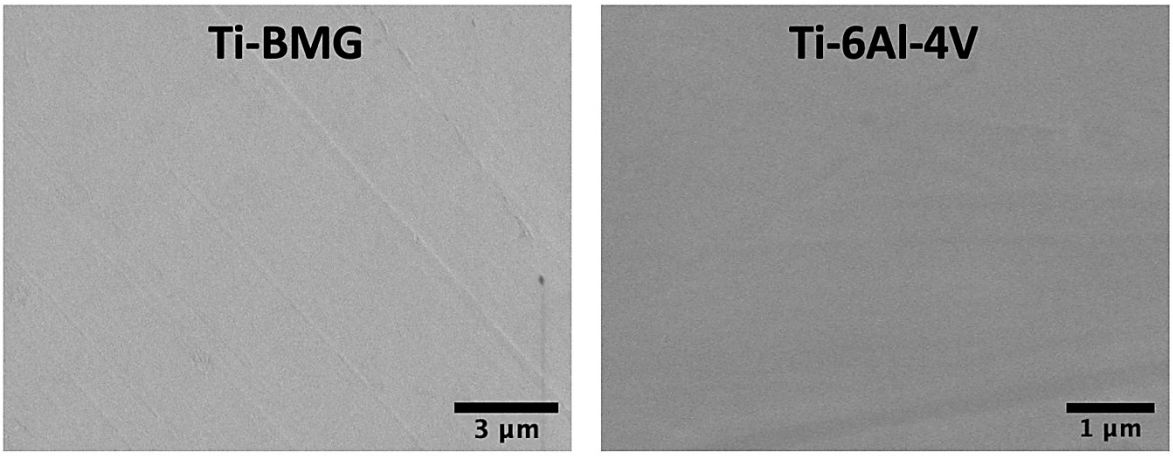

Fig. S1. Comparison of surface morphology of the Ti-BMG and Ti-6Al-4V as-cast state samples.

S1. Oral biofilm proteomics analysis

In order to investigate the impact of $Ti_{40}Zr_{10}Cu_{36}Pd_{14}$-BMG on bacterial consortia of oral biofilm obtained from healthy donors, proteomics analysis was performed on the protein samples.

In Figure S2 the complete list of the detected species is given, together with their quantification in terms of prevalence (%) over the total amount. The red line represents the threshold of populations representing at least >1%.

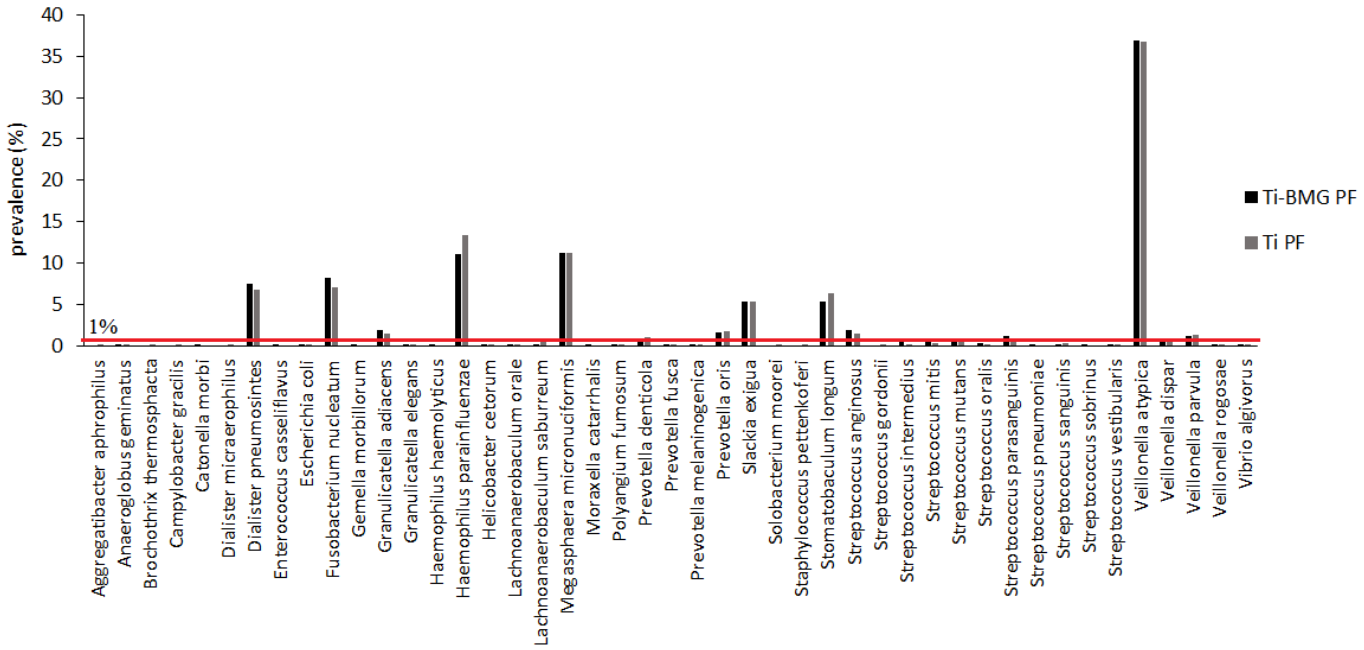

Fig. S2. Distribution of bacterial species in planktonic form in oral biofilm done by proteomics analysis (red line shows the prevalence of 1%). PF indicates planktonic form.

References

[1] M. Geetha, A.K. Singh, R. Asokamani, A.K. Gogia, Ti based biomaterials, the ultimate choice for orthopaedic implants – a review, Prog. Mater. Sci. 54 (2009) 397–425.

[2] R. Saini, P.P. Marawar, S. Shete, S. Saini, Periodontitis, a true infection, J. Global Infect. Dis. 1 (2009) 149–150.

[3] P.D. Marsh, Dental plaque as a biofilm and a microbial community – implications for health and disease, BMC Oral Health 6 (2006) S14.

[4] O.Y. Yu, I.S. Zhao, M.L. Mei, E.C.-M. Lo, C.-H. Chu, Dental biofilm and laboratory microbial culture models for cariology research, Dent. J. 5 (2017) 21.

[5] E. Sharifikolouei, Z. Najmi, A. Cochis, A.C. Scalia, M. Aliabadi, S. Perero, L. Rimondini, Generation of cytocompatible superhydrophobic Zr–Cu–Ag metallic glass coatings with antifouling properties for medical textiles, Mater, Today Bio 12 (2021), 100148.

[6] E. Velasco-Ortega, I. Ortiz-García, A. Jiménez-Guerra, L. Monsalve-Guil, F. Muñoz-Guzón, R.A. Perez, F.J. Gil, Comparison between sandblasted acid-etched and oxidized titanium dental implants: in vivo study, Int. J. Mol. Sci. 20 (2019) 3267.

[7] S.W. Tan, T.N. Sut, W.Y. Jeon, B.K. Yoon, J.A. Jackman, On/off switching of lipid bicelle adsorption on titanium oxide controlled by sub-monolayer molecular surface functionalization, Appl. Mater. Today 27 (2022), 101444.

[8] S. Ferraris, A. Cochis, M. Cazzola, M. Tortello, A. Scalia, S. Spriano, L. Rimondini, Cytocompatible and anti-bacterial adhesion nanotextured titanium oxide layer on titanium surfaces for dental and orthopedic implants, Front. Bioeng. Biotechnol. 7 (2019) 103.

[9] K. Li, C. Wang, J. Yan, Q. Zhang, B. Dang, Z. Wang, Y. Yao, K. Lin, Z. Guo, L. Bi, Y. Han, Evaluation of the osteogenesis and osseointegration of titanium alloys coated with graphene: an in vivo study, Sci. Rep. 8 (2018) 1843.

[10] D.S. Morais, R.M. Guedes, M.A. Lopes, Antimicrobial approaches for textiles: from research to market, Materials 9 (2016) 498.

[11] K. Xu, Z. Yuan, Y. Ding, Y. He, K. Li, C.C. Lin, B.L. Tao, Y.L. Yang, X. Li, P. Liu, K.Y. Cai, Near-infrared light triggered multi-mode synergetic therapy for improving antibacterial and osteogenic activity of titanium implants, Appl. Mater. Today 24 (2021), 101155.

[12] A.L. Greer, Metallic glasses...on the threshold, Mater. Today 12 (2009) 14–22.

[13] W.H. Wang, C. Dong, C.H. Shek, Bulk metallic glasses, Mater. Sci. Eng. R 44 (2004) 45–89.

[14] L.C. Liu, M. Hasan, G. Kumar, Metallic glass nanostructures: fabrication, properties, and applications, Nanoscale 6 (2014) 2027–2036.

[15] B. Sarac, S. Bera, S. Balakin, M. Stoica, M. Calin, J. Eckert, Hierarchical surface patterning of Ni- and Be-free Ti- and Zr-based bulk metallic glasses by thermoplastic net-shaping, Mater. Sci. Eng., C 73 (2017) 398–405.

[16] S. Bera, P. Ramasamy, D. S¸ opu, B. Sarac, J. Zalesak, C. Gammer, M. Stoica, M. Calin, J. Eckert, Tuning the glass forming ability and mechanical properties of Ti-based bulk metallic glasses by Ga additions, J. Alloys Compd. 793 (2019) 552–563.

[17] S. Bera, B. Sarac, S. Balakin, P. Ramasamy, M. Stoica, M. Calin, J. Eckert, Micropatterning by thermoplastic forming of Ni-free Ti-based bulk metallic glasses, Mater. Des. 120 (2017) 204–211.

[18] B. Sarac, S. Bera, F. Spieckermann, S. Balakin, M. Stoica, M. Calin, J. Eckert, Micropatterning kinetics of different glass-forming systems investigated by thermoplastic net-shaping, Scripta Mater. 137 (2017) 127–131.

[19] M. Calin, A. Gebert, A.C. Ghinea, P.F. Gostin, S. Abdi, C. Mickel, J. Eckert, Designing biocompatible Ti-based metallic glasses for implant applications, Mater. Sci. Eng., C 33 (2013) 875–883.

[20] J.J. Oak, D.V. Louzguine-Luzgin, A. Inoue, Fabrication of Ni-free Ti-based bulkmetallic glassy alloy having potential for application as biomaterial, and investigation of its mechanical properties, corrosion, and crystallization behavior, J. Mater. Res. 22 (2007) 1346–1353.

[21] P. Du, T. Xiang, X. Yang, G. Xie, Enhanced mechanical and antibacterial properties of Cu-bearing Ti-based bulk metallic glass by controlling porous structure, J. Alloys Compd. 904 (2022), 164005.

[22] P. Du, T. Xiang, Z. Cai, G. Xie, The influence of porous structure on the corrosion behavior and biocompatibility of bulk Ti-based metallic glass, J. Alloys Compd. 906 (2022), 164326.

[23] P. Du, Z. Wu, K. Li, T. Xiang, G. Xie, Porous Ti-based bulk metallic glass orthopaedic biomaterial with high strength and low Young's modulus produced by one step SPS, J. Mater. Res. Technol. 13 (2021) 251–259.

[24] B. Lin, R. Mu, L.F. Yang, X.F. Bian, Antibacterial effect of metallic glasses, Chin. Sci. Bull. 57 (2012) 1069–1072.

[25] Y.S. Lin, C.F. Hsu, J.Y. Chen, Y.M. Cheng, P.Y. Lee, Wear behavior of mechanically alloyed Ti-based bulk metallic glass composites containing carbon nanotubes, Metals 6 (2016) 289.

[26] D.C. Hofmann, L.M. Andersen, J. Kolodziejska, S.N. Roberts, J.P. Borgonia, W.L. Johnson, K.S. Vecchio, A. Kennett, Optimizing bulk metallic glasses for robust, highly wear-resistant gears, Adv. Eng. Mater. 19 (2016), 1600541.

[27] S.F. Lin, S.F. Ge, Z.W. Zhu, W. Li, Z.K. Li, H. Li, H.M. Fu, A.M. Wang, Y.X. Zhuang, H.F. Zhang, Double toughening Ti-based bulk metallic glass composite with high toughness, strength and tensile ductility via phase engineering, Appl. Mater. Today 22 (2021), 100944.

[28] J. Schroers, G. Kumar, T.M. Hodges, S. Chan, T.R. Kyriakides, Bulk metallic glasses for biomedical applications, JOM 61 (2009) 21–29.

[29] H.F. Li, Y.F. Zheng, Recent advances in bulk metallic glasses for biomedical applications, Acta Biomater. 36 (2016) 1–20.

[30] A. Liens, A. Etiemble, P. Rivory, S. Balvay, J.M. Pelletier, S. Cardinal, D. Fabregue, H. Kato, P. Steyer, T. Munhoz, J. Adrien, N. Courtois, D.J. Hartmann, J. Chevalier, On the potential of bulk metallic glasses for dental implantology: case study on $Ti_{40}Zr_{10}Cu_{36}Pd_{14}$, Materials 11 (2018).

[31] S.L. Zhu, X.M. Wang, F.X. Qin, M. Yoshimura, A. Inoue, New TiZrCuPd quaternary bulk glassy alloys with potential of biomedical applications, Mater. Trans. 48 (2007) 2445–2448.

[32] F.X. Qin, M. Yoshimura, X.M. Wang, S.L. Zhu, A. Kawashima, K. Asami, A. Inoue, Corrosion Behavior of a Ti-based bulk metallic glass and its crystalline alloys, Mater. Trans. 48 (2007) 1855–1858.

[33] G. Lütjering, Property optimization through microstructural control in titanium and aluminum alloys, Mater. Sci. Eng., A 263 (1999) 117–126.

[34] P. Gong, L. Deng, J. Jin, S. Wang, X. Wang, K. Yao, Review on the research and development of Ti-based bulk metallic glasses, Metals 6 (2016) 264.

[35] B. Sarac, J. Eckert, Thermoplasticity of metallic glasses: processing and applications, Prog. Mater. Sci. 127 (2022), 100941.

[36] J. Schroers, The superplastic forming of bulk metallic glasses, JOM 57 (2005) 35–39.

[37] F. Schwarz, J. Becker. Die Behandlung periimplantärer Infektionen an Zahnimplantaten, Deutsche Gesellschaft für Implantologie, Deutsche Gesellschaft für Zahn-, Mund- und Kieferheilkunde, 05/2016.

[38] T.E. Rams, J.E. Degener, A.J. van Winkelhoff, Antibiotic resistance in human periimplantitis microbiota, Clin. Oral Implants Res. 25 (2014) 82–90.

[39] A. Cochis, S. Ferraris, R. Sorrentino, B. Azzimonti, C. Novara, F. Geobaldo, F. Truffa Giachet, C. Vineis, A. Varesano, A. Sayed Abdelgeliel, S. Spriano, L.

Rimondini, Silver-doped keratin nanofibers preserve a titanium surface from biofilm contamination and favor soft-tissue healing, J. Mater. Chem. B 5 (2017) 8366–8377.

[40] E. Dalla Pozza, M. Manfredi, J. Brandi, A. Buzzi, E. Conte, R. Pacchiana, D. Cecconi, E. Marengo, M. Donadelli, Trichostatin A alters cytoskeleton and energy metabolism of pancreatic adenocarcinoma cells: an in depth proteomic study, J. Cell. Biochem. 119 (2018) 2696–2707.

[41] J. Brandi, S. Cheri, M. Manfredi, C. Di Carlo, V. Vita Vanella, F. Federici, E. Bombiero, A. Bazaj, E. Rizzi, L. Manna, G. Cornaglia, U. Marini, M.T. Valenti, E. Marengo, D. Cecconi, Exploring the wound healing, anti-inflammatory, antipathogenic and proteomic effects of lactic acid bacteria on keratinocytes, Sci. Rep. 10 (2020), 11572.

[42] R. Gurdeep Singh, A. Tanca, A. Palomba, F. Van der Jeugt, P. Verschaffelt, S. Uzzau, L. Martens, P. Dawyndt, B. Mesuere, Unipept 4.0: functional analysis of metaproteome data, J. Proteome Res. 18 (2019) 606–615.

[43] B. Sarac, G. Kumar, T. Hodges, S.Y. Ding, A. Desai, J. Schroers, Three-dimensional shell fabrication using blow molding of bulk metallic glass, J. Microelectromech. Syst. 20 (2011) 28–36.

[44] J. Schroers, Processing of bulk metallic glass, Adv. Mater. 22 (2010) 1566–1597.

[45] B. Sarac, J. Schroers, Designing tensile ductility in metallic glasses, Nat. Commun. 4 (2013) 2158.

[46] B. Sarac, J. Ketkaew, D.O. Popnoe, J. Schroers, Honeycomb structures of bulk metallic glasses, Adv. Funct. Mater. 22 (2012) 3161–3169.

[47] B. Sarac, Microstructure-Property Optimization in Metallic Glasses, Springer International Publishing, 2015, p. 89.

[48] S. Maeda, T. Yamasaki, Y. Yokoyama, D. Okai, T. Fukami, H.M. Kimura, A. Inoue, Viscosity measurements of $Zr_{55}Cu_{30}Al_{10}Ni_5$ and $Zr_{50}Cu_{40-x}Al_{10}Pd_x$ (x=0,

3 and 7 at.%) supercooled liquid alloys by using a penetration viscometer, Mater. Sci. Eng., A 449 (2007) 203–206.

[49] A. Rezvan, B. Sarac, V. Soprunyuk, J.T. Kim, K.K. Song, C.J. Li, W. Schranz, J. Eckert, Influence of combinatorial annealing and plastic deformation treatments on the intrinsic properties of Cu46Zr46Al8 bulk metallic glass, Intermetallics 127 (2020), 106986.

[50] A. Inoue, Stabilization of metallic supercooled liquid and bulk amorphous alloys, Acta Mater. 48 (2000) 279–306.

[51] N.S. McIntyre, S. Sunder, D.W. Shoesmith, F.W. Stanchell, Chemical information from XPS—applications to the analysis of electrode surfaces, J. Vac. Sci. Technol. 18 (1981) 714–721.

[52] G. Wang, J. Li, K. Lv, W. Zhang, X. Ding, G. Yang, X. Liu, X. Jiang, Surface thermal oxidation on titanium implants to enhance osteogenic activity and in vivo osseointegration, Sci. Rep. 6 (2016), 31769.

[53] Y. He, Z.S. Fishman, K.R. Yang, B. Ortiz, C. Liu, J. Goldsamt, V.S. Batista, L.D. Pfefferle, Hydrophobic CuO nanosheets functionalized with organic adsorbates, J. Am. Chem. Soc. 140 (2018) 1824–1833.

[54] S. Ward, M.A. Isaacs, G. Gupta, M. Mamlouk, S.S. Pramana, Boosting the oxygen evolution activity in non-stoichiometric praseodymium ferrite-based perovskites by A site substitution for alkaline electrolyser anodes, Sustain. Energy Fuels 5 (2021) 154–165.

[55] L. Jia, N. Han, J. Du, L. Guo, Z. Luo, Y. Liu, Pathogenesis of important virulence factors of porphyromonas gingivalis via toll-like receptors, Front. Cell. Infect. Microbiol. 9 (2019).

[56] P. Gholizadeh, A. Pormohammad, H. Eslami, B. Shokouhi, V. Fakhrzadeh, H.S. Kafil, Oral pathogenesis of Aggregatibacter actinomycetemcomitans, Microb. Pathog. 113 (2017) 303–311.

[57] A. Cochis, B. Azzimonti, C. Della Valle, E. De Giglio, N. Bloise, L. Visai, S. Cometa, L. Rimondini, R. Chiesa, The effect of silver or gallium doped

titanium against the multidrug resistant Acinetobacter baumannii, Biomaterials 80 (2016) 80–95.

[58] S. Wang, Y. Liu, C. Zhang, Z. Liao, W. Liu, The improvement of wettability, biotribological behavior and corrosion resistance of titanium alloy pretreated by thermal oxidation, Tribol. Int. 79 (2014) 174–182.

[59] L.R. Rivera, A. Cochis, S. Biser, E. Canciani, S. Ferraris, L. Rimondini, A.R. Boccaccini, Antibacterial, pro-angiogenic and pro-osteointegrative zeinbioactive glass/copper based coatings for implantable stainless steel aimed at bone healing, Bioact. Mater. 6 (2021) 1479–1490.

[60] Y. Yoshida, S. Furuta, E. Niki, Effects of metal chelating agents on the oxidation of lipids induced by copper and iron, Biochim. Biophys. Acta 1210 (1993) 81–88.

[61] A. Cochis, B. Azzimonti, R. Chiesa, L. Rimondini, M. Gasik, Metallurgical gallium additions to titanium alloys demonstrate a strong time-increasing antibacterial activity without any cellular toxicity, ACS Biomater. Sci. Eng. 5 (2019) 2815–2820.

[62] A. Reyes-Jara, N. Cordero, J. Aguirre, M. Troncoso, G. Figueroa, Antibacterial effect of copper on microorganisms isolated from bovine mastitis, Front. Microbiol. 7 (2016) 626.

[63] N. Kaushik, P. Sharma, S. Ahadian, A. Khademhosseini, M. Takahashi, A. Makino, S. Tanaka, M. Esashi, Metallic glass thin films for potential biomedical applications, J. Biomed. Mater. Res. B 102 (2014) 1544–1552.

[64] A. Liens, A. Etiemble, P. Rivory, S. Balvay, J.M. Pelletier, S. Cardinal, D. Fabrègue, H. Kato, P. Steyer, T. Munhoz, J. Adrien, N. Courtois, D.J. Hartmann, J. Chevalier, On the potential of bulk metallic glasses for dental implantology: case study on Ti40Zr10Cu36Pd14, Materials 11 (2018) 249.

[65] B. Grössner-Schreiber, M. Griepentrog, I. Haustein, W.D. Müller, K.P. Lange, H. Briedigkeit, U.B. G€obel, Plaque formation on surface modified dental implants. An in vitro study, Clin. Oral Implants Res. 12 (2001) 543–551.

[66] L. Dong, J. Yin, J. Zhao, S.-R. Ma, H.-R. Wang, M. Wang, W. Chen, W.-Q. Wei, Microbial similarity and preference for specific sites in healthy oral cavity and esophagus, Front. Microbiol. 9 (2018) 1603.

[67] A.M. Valm, The structure of dental plaque microbial communities in the transition from health to dental caries and periodontal disease, J. Mol. Biol. 431 (2019) 2957–2969.

[68] C. Binda, L.R. Lopetuso, G. Rizzatti, G. Gibiino, V. Cennamo, A. Gasbarrini, Actinobacteria: a relevant minority for the maintenance of gut homeostasis, Dig. Liver Dis. 50 (2018) 421–428.

$Ti_{40}Zr_{10}Cu_{36}Pd_{14}$ Bulk Metallic Glass as Oral Implant Material

Amir Rezvan[a, b], Elham Sharifikolouei[c], Viktor Soprunyuk[d], Wilfried Schranz[d], Juraj Todt[b], Alice Lassnig[a], Christoph Gammer[a], Nikolaus August Sifferlinger[e], Atacan Asci[b], Ilya Okulov[f, g], Sandra Schlögl[h], Jozef Keckes[b], Ziba Najmi[i], Andrea Cochis[i], Alessandro Calogero Scalia[i], Lia Rimondini[i], Baran Sarac[a], Jürgen Eckert[a, b]

[a] *Erich Schmid Institute of Materials Science, Austrian Academy of Sciences, Jahnstraße 12, A-8700 Leoben, Austria*

[b] *Department of Materials Science, Chair of Materials Physics, Montanuniversität Leoben, Jahnstraße 12, A-8700 Leoben, Austria*

[c] *Department of Applied Science and Technology, Politecnico di Torino, Corso Duca Degli Abruzzi 24, 10129, Turin (TO), Italy*

[d] *University of Vienna, Faculty of Physics, Physics of Functional Materials, Boltzmanngasse 5, A-1090 Vienna, Austria*

[e] *Department of Mineral Resources Engineering, Chair of Mining Engineering and Mineral Economics, Montanuniversität Leoben, Franz-Josef-Straße 18, A-8700, Leoben, Austria*

[f] *Leibniz Institute for Materials Engineering – IWT, Badgasteiner Str. 3, 28359 Bremen, Germany*

[g] *Faculty of Production Engineering University of Bremen, Badgasteiner Str. 1, 28359 Bremen, Germany*

[h] *Polymer Competence Center Leoben GmbH, Roseggerstrasse 12, 8700 Leoben, Austria*

[i] *Department of Health Sciences, Center for Translational Research on Autoimmune and Allergic Diseases − CAAD, Università del Piemonte Orientale UPO, Corso Trieste 15/A, 28100 Novara (NO), Italy*

Abstract

The application of highly biocompatible advanced materials leads to fewer complications and more successful medical treatments. This study proposes $Ti_{40}Zr_{10}Cu_{36}Pd_{14}$ bulk metallic glass (BMG) as an oral implant material and provides insights into its possible processing routes, where high-temperature compression molding via an optimized process is adopted to both evaluate the thermoplastic net-shaping kinetics and tune the intrinsic properties of the alloy. We present processed BMGs and BMG composites of the same composition with improved thermomechanical stability, from which high strength retention at temperatures, compared to the cast glass, by above 100 K higher is registered via dynamic mechanical analysis. ~100 nm thin surface layers comprised of Ti, Cu, and Zr oxides form at the surface of the alloys, as identified by high-resolution transmission microscopy. Besides, the drop in the corrosion current density of the processed glass by two orders of magnitude along with 4 orders of magnitude lower passivation current density compared to the values of the as-cast state confirms an extremely high stability in a 0.9 wt.% saline environment which can be linked to surface hydrophobicity. Cytocompatibility analysis conducted by seeding human gingival fibroblast cells (HGF) directly onto the thermoplastically formed $Ti_{40}Zr_{10}Cu_{36}Pd_{14}$ BMG reveals no adverse effect on cytocompatibility. On the other hand, the formation of a nanoscale oxide layer on the thermoplastically formed samples leads to significantly higher cell attachments on the surface.

Graphical abstract

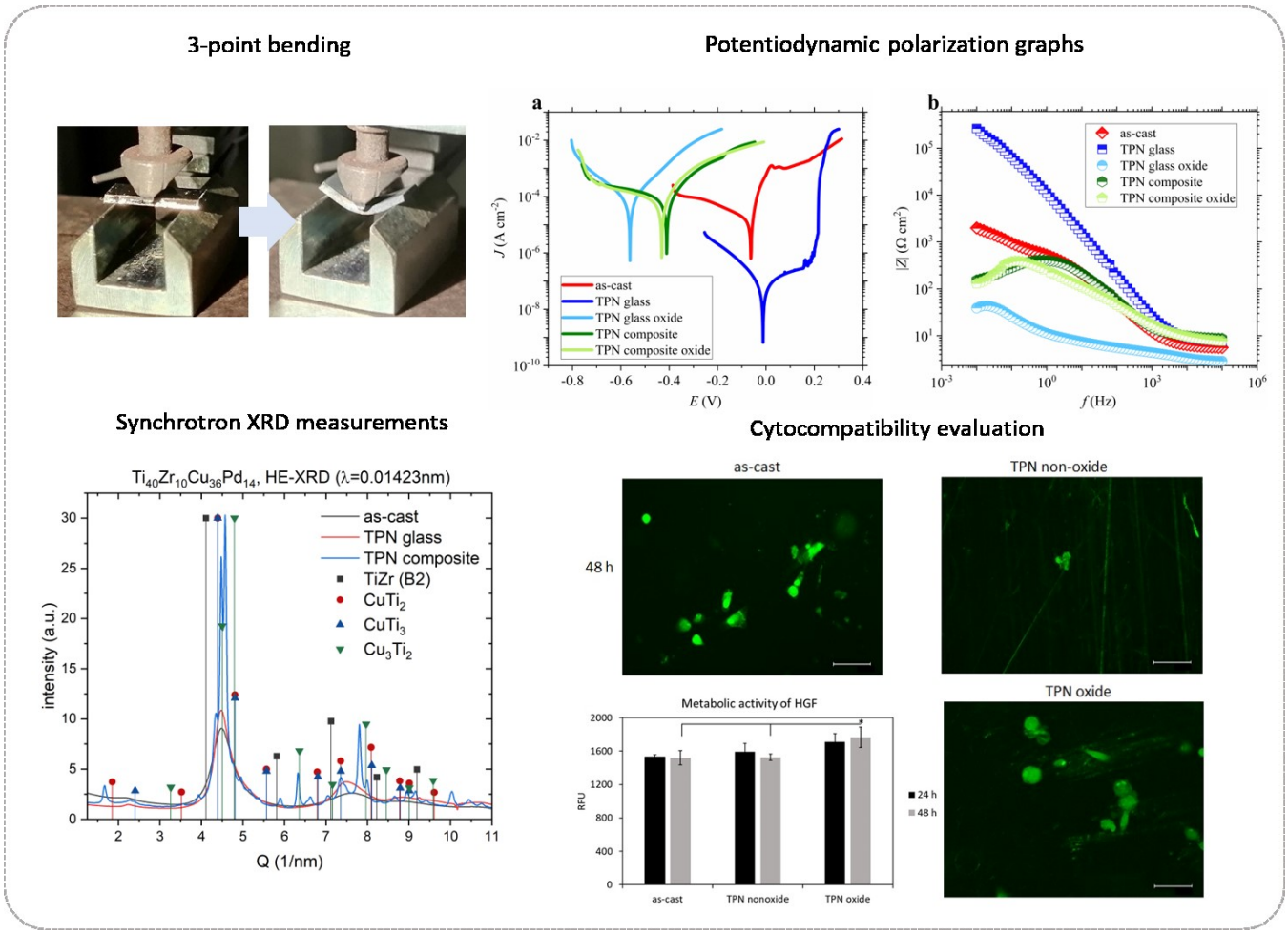

1. Introduction

Considering the demand for functional materials that can be used in biomedical applications, surface topography becomes important, thereby processing and net-shaping of materials. The disadvantage of most crystalline metals is that they possess strength values of either above 100 MPa or below 10^{-7} MPa. They pass the in-between values with their phase transition from a solid to a liquid state [1]. Bulk metallic glasses (BMGs) grant access to an ideal processing region, in which glassy metals with a strength of less than 10^{-7} MPa and a viscosity of 10^{3} – 10^{8} Pa s can be processed like plastics [2].

The drawback of direct casting is the limitation to simple shapes, such as rods and plates. Thermoplastic net-shaping (TPN) is a two-step process where the

casting and forming steps of BMGs are decoupled [3, 4]. Thereby the cast piece undergoes deformation after it is heated close to the crystallization temperature (T_x), the region where BMGs show their highest deformability. From an engineering viewpoint, the surface micro-patterning of BMGs can be achieved by TPN in the supercooled liquid region (SCLR), by which hierarchically modulated surfaces of high complexity can be generated [4-7]. However, marginal glass-forming ability and the high susceptibility of specific types of BMGs towards oxidation result in limited formability when formed into microcavities, where the resistance against flow restricts the desired patterns to bump-shaped microfeatures with controlled height and rounded corners [8]. Moreover, crystallization has to be avoided. Crystallization limits the processing time for a hot-forming operation since the flow in crystalline materials is orders of magnitude higher than in the supercooled liquid region (SCLR) [9]. An appealing characteristic of metallic glasses is that the crystallization kinetics in the SCLR is sluggish. This allows excellent net-shape processing on a convenient time scale, i.e., the material can be deformed within a rather large time window [2].

The assessment of the viscoelastic behavior of glasses under controlled laboratory conditions is an approach to estimate how the materials could respond in harsh environments. A suitable technique is dynamic mechanical analysis (DMA), conveying information about the thermo-mechanically driven structural relaxation and crystallization behavior in advanced glassy multicomponent systems.

The life expectancy in industrialized countries has increased in the last decades and, consequently, the necessity for restorative medicine. One of the strongest emerging economic fields in this context are dental implants and medical devices. When it comes to oral implants, there are several parameters at force to be considered. The direct biocompatibility is evaluated by the cell adhesion and proliferation on the surface, and indirect cytocompatibility is connected to the

corrosion and wear resistance of the material. If the implant releases wear debris over time, it could cause inflammation on the surgery side leading to a retrieval of the implant. Additionally, with the advancement of functional biomaterials, there is a search for the development of antifouling implant surfaces. The most popular oral implants rely on Ti- and Zr-based alloys for their proven biocompatibility [10, 11]. As mentioned before, metallic glasses have the advantage of improved oxidation and corrosion resistance compared with their crystalline counterparts, which in this case, is crucial to prevent inflammation in the long term [12, 13]. In this regard, toxic-element free $Ti_{60}Zr_{20}Si_8Ge_7B_3Sn_2$ and $Ti_{50}Zr_{30}Si_8Ge_7B_3Sn_2$ metallic glasses have been reported to have higher pitting potential and a larger passivation domain coupled with outstanding cytocompatibility in contact with mesenchymal stem cells [14]. When it comes to antifouling properties, one of the most essential factors to control are the surface chemistry and topography. Bacteria with various physicochemical characteristics adhere differently to a given material, and the surface is the first place they encounter. In other words, depending on the bacteria's surface characteristics, which are defined by their genome, adhering bacteria might have a preference to adhere to hydrophobic or hydrophilic surfaces [15]. Sharifikolouei et al. [16] have used this approach to develop Zr-based metallic glasses with promising antifouling properties. One might say that the surface wettability of Ti-based metallic glasses such as $Ti_{40}Zr_{10}Cu_{36}Pd_{14}$ is similar to that of Ti-6Al-4V as the gold standard for oral implants. However, in our previous study [17], it was shown that the initial performance of $Ti_{40}Zr_{10}Cu_{36}Pd_{14}$ BMG is similar to Ti-6Al-4V for oral implants, but after an extended time, the formation of an oxide layer (TiO_2) on the surface of Ti-6Al-4V promotes a significantly higher oral biofilm formation. Additionally, $Ti_{40}Zr_{10}Cu_{36}Pd_{14}$ BMG has higher strength and lower Young's modulus compared with Ti-6Al-4V, which is beneficial to alleviate the stress-shielding effect [18-21], and lower ion release below the cytotoxicity threshold in artificial saliva solution [17].

In this work, the structural relaxation kinetics and crystallization behavior of $Ti_{40}Zr_{10}Cu_{36}Pd_{14}$ upon net-shaping is evaluated by a sensitive frequency-dependent DMA technique at elevated temperatures, which gives insights into the impact of thermoplastic net-shaping under certain conditions. The corrosion behavior of oxide-containing and oxide-free fully glassy and partially crystallized, i.e., composite, samples are analyzed through potentiodynamic polarization and electrochemical impedance spectroscopy. The oxidation of the alloy is investigated by means of TEM-EDX. Furthermore, the effect of the oxide layer formation on the cell cytocompatibility of $Ti_{40}Zr_{10}Cu_{36}Pd_{14}$ BMG is assessed by cultivating human gingival fibroblast (HGF) cells directly onto the specimen surfaces.

2. Materials and Methods

2.1 Materials Preparation

2.1.1 Casting

A $Ti_{40}Zr_{10}Cu_{36}Pd_{14}$ master alloy was prepared in an Edmund Buehler AM0.5 arc melting system operated under a Ti-gettered argon atmosphere. The industrial-grade alloy constituents of 99.9% purity were weighed with an accuracy of ± 0.001 g. Rotary and diffusion pumps were utilized to evacuate the system down to 10^{-7} mbar. During melting, the melting current went up to a maximum of 160 A. To ensure homogeneity of the ingot, the melting was repeated four times. The alloy was cast afterwards into a copper mold with a rod geometry of 2 mm diameter and 50 mm length. The pressure gradient necessary for suction between the designed mold cavity and the working chamber was attained by purging argon. From the cast rod pieces were cut for subsequent characterization.

2.1.2 Thermoplastic net-shaping

High-temperature compression molding was adopted to evaluate the thermoplastic net-shaping kinetics of the alloy, where the process parameters

such as time, temperature, and pressure were optimized. The specimens ($Ti_{40}Zr_{10}Cu_{36}Pd_{14}$ BMG) were solid cylinder shapes ~ 3.5 mm in height and 2 mm in diameter. They were heated to temperatures around 713 K then pressed by up to 10 kN with the loading rates of 10^{-2} s^{-1} (TPN glass) and 10^{-3} s^{-1} (TPN composite). The deformation in the course of heating was carried out under a vacuum of 10^{-4} mbar.

2.2 Materials Characterization

2.2.1 Synchrotron XRD and TEM analyses

Structural analysis was carried out by high-energy X-ray diffraction (XRD) in transmission geometry with a monochromatic beam of 14.23 pm wavelength. Two-dimensional diffraction patterns were collected on a Perkin Elmer XRD 1621 two-dimensional X-ray detector placed approx. 1.3 m downstream of the samples and were azimuthally integrated using the pyFAI software package [22]. The detector geometry was determined using a LaB6 calibration standard and using the routines provided by pyFAI. Peak indexing was performed using the PDF-2 database (ICDD, Newton Square, USA) within EVA (Bruker AXS, Karlsruhe, Germany). Detailed structural analysis was carried out using transmission electron microscopy (TEM). Electron transparent lamellae of the surface region was created via focused ion beam (FIB) lift-out in a Zeiss Auriga workstation equipped with an Omniprobe micromanipulator. To protect the sample surface during FIB cutting a protective carbon layer and an amorphous W layer were deposited on top of the surface using the gas injection system (GIS) of the work station. Coarse trench cuts up to fine polishing of the lamellae were performed at an acceleration voltage of 30 kV and currents ranging from 2 nA down to 50 pA. The TEM analyses were conducted in a JEOL 2200FS microscope at 200 kV, equipped with an Oxford Ultim Max EDX detector. The cross-sections were analyzed using scanning TEM mode, and the elemental

compositions, depending on the sample interior and surface, were measured using EDX mapping.

2.2.2 DMA and TE

Dynamic mechanical analysis (DMA) was conducted in 3-point bending mode within a temperature range from 300 K to 850 K while purging with N_2 gas continuously upon heating, a constant heating rate of 5 K min^{-1} was employed at frequencies of 0.1 to 1 to 10 Hz. The specimens had solid rectangular shapes of 5 mm in length, 2 mm in width, and 1 mm in thickness. The experiments were performed by imposing 10 N axial force in a displacement-controlled mode with a displacement oscillation amplitude of 5 μm. At the test's domain, the maximum stress across the samples reached 30 N mm^{-2}. Thermal expansion/contraction (TE) was measured using a Discovery HR-3 device (TA Instruments) under a constant load of 50 mN. The specimens were heated from 300 K to 850 K at 5 K min^{-1} heating/cooling rates.

2.2.3 Electrochemical investigations

The electrochemical measurements were conducted in a three-electrode glass cell at room temperature. A 0.5 mm diameter 23 cm long Pt wire ring and a RE-1BP type Ag/AgCl reference electrode with a ceramic junction filled with 3 M NaCl electrolyte (+0.195 V vs. reference hydrogen electrode) were used as counter and reference electrodes, respectively. The samples were cut, and one side was mirror-polished in the as-cast state and after TPN. In order to block the signal, the back side of the samples was painted with nail varnish. The immersed areas of the samples were 0.093 ± 0.006 (as-cast), 0.041 ± 0.008 (TPN glass and oxide layer) and 0.118 ± 0.005 (TPN crystallized and oxide layer), as determined by an Olympus BX51 Fluorescence Microscope using the Olympus Stream Motion 1.9.3. software – Extended Focal Imaging feature and area calculation function. The electrochemical measurements were performed with a Gamry Interface

1010E Potentiostat/Galvanostat/ZRA. Before the experiments, the open circuit potential was applied for 3600 s to stabilize the working electrode–electrolyte interface. Electrochemical impedance spectroscopy (EIS) was performed at OCP at an AC amplitude of 10 mV recorded from 100000 to 0.01 Hz. Afterwards, linear sweep voltammetry (LSV) was conducted with the same electrodes. The forward scan ran at 1 mV s^{-1} ranged from –0.3 V vs. OCP until +1.5 V vs. Ag/AgCl or when the current density reached 0.01 A cm^{-2}. The reverse scans were also conducted using the same parameters but excluded from the results because repassivation was not attained in any of the samples. At least two tests were performed for each composition and electrolyte for statistical information.

2.2.4 Contact angle measurements

Static water contact angle measurements were conducted on a DSA 100 (Drop Shape Analysis System) from Kruess GmbH via the sessile drop method on the etched surface of the as-cast and TPN $Ti_{40}Zr_{10}Cu_{3}6Pd_{14}$ BMGs. De-ionized water droplets with a volume of 2 μL were placed on the surface of the samples by an automated deposition procedure and their contact angle with the solid surface were recorded and analyzed using the embedded high-resolution camera and the specialized software of the measuring device. Two different holding substrates were employed to align the samples properly as the small surface area made the contact angle measurements challenging to carry out. The contact angles were measured after 10 s deposition and then in appropriate time intervals until the 60th second. The results are presented in the form of 10 s and the time dependent value after 60 s, accordingly. For each sample, the average of 5 measurements was taken.

2.3 In vitro cytocompatibility evaluation

2.3.1 Cell cultivation

Human gingival fibroblast cells (HGF) were purchased from Promo Cell (PCS-201-018) and cultivated in minimal essential medium eagle-alpha modification (α-MEM, Sigma-Aldrich) supplemented with 10% fetal bovine serum (FBS, Sigma-Aldrich) and 1% antibiotics at 310 K, 5% CO_2 atmosphere. The cells were cultivated until 80%–90% confluence, detached by a trypsin-EDTA solution (0.25% in phosphate buffer solution – PBS), harvested and used for the experiments.

2.3.2 Cytocompatibility evaluation

The cells were directly seeded onto the specimens' surface (2 mm diameter) at a defined density (2000 cells/sample), and after 4 hours of allowing adhesion, 300 µL of culture media was added to each sample. Subsequently, they were cultivated for 24 and 48 hours; at each time point, the viability of the cells was evaluated by means of their metabolic activity using the resazurin colorimetric metabolic assay (alamarBlue™, ready-to-use solution from Life Technologies) by directly adding the dye solution (0.015% in PBS) onto the wells containing specimens. After 4 hours of incubation in the dark, the fluorescent signals (expressed as relative fluorescent units – RFU) were detected at 590 nm by a spectrophotometer (Spark, Tecan, Switzerland). Moreover, the fluorescent Live/Dead assay was applied to visually check for viable cells (Live/Dead, Viability/ Cytotoxicity Kit for mammalian cells, Invitrogen) with a digital EVOS FLoid microscope (Life Technologies). Finally, the morphology of the cells was visually investigated by scanning electron microscopy (SEM, JSM-IT500, JEOL); briefly, specimens were dehydrated by the alcohol scale (70-90% ethanol, 1 hour each and 100% for 2 hours), swelled with hexamethyldisilazane, mounted onto stubs with carbon tape and metalized with gold for 2 minutes (smart coater, JEOL). Images were collected at different magnifications (×200 and ×500) using a secondary electron detector.

2.4 Statistical analysis of data

The experiments were performed in triplicate, and the results were statistically analyzed using the SPSS software (v.20.0, IBM, USA). First, the data normal distribution and the homogeneity of the variance were confirmed by Shapiro-Wilk's and Levene's tests, respectively; then, groups were compared by the one-way ANOVA using Tukey's test as post-hoc analysis. Significant differences were established at p-values <0.05.

3. Results and Discussion

3.1 Structural and compositional characterization

Synchrotron XRD patterns of $Ti_{40}Zr_{10}Cu_{36}Pd_{14}$ as-cast, TPN glass, and TPN composite are shown in Fig. 1. The patterns of $Ti_{40}Zr_{10}Cu_{36}Pd_{14}$ as-cast and TPN glass signify a glassy nature. However, the second sharp diffraction peak of the TPN glass is deconvoluted into two peaks, indicating structural modifications. Hence, it can be concluded that the applied thermomechanical driving force during the TPN process can induce structural heterogeneities [23]. On the pattern of the TPN composite, crystalline diffraction peaks corresponding to the B2-TiZr, $CuTi_2$, $CuTi_3$, and Cu_3Ti_2 phases are superimposed. Exploring the structure reveals that spherulites surrounded by semi-crystalline outer shells are formed in the glassy matrix. These shells act as a synergy between order and disorder in the structure. Larger needle-shaped Cu_3Ti_2 phases precipitate in the center of the spherulites. To these phases, finer needles of tetragonal CuTi attach at 90°. Rather at the center of spherulites, $CuTi_3$ of a few percent might form during solidification upon eutectic reactions as the cooling rate is kept at its threshold during casting in order to cast the largest possible BMG. B2-TiZr is present primarily in mature spherulites. It nucleates in the vicinity of the tetragonal CuTi crystals and grows in all directions to the shell. This grants the spherical shape to the spherulites [24].

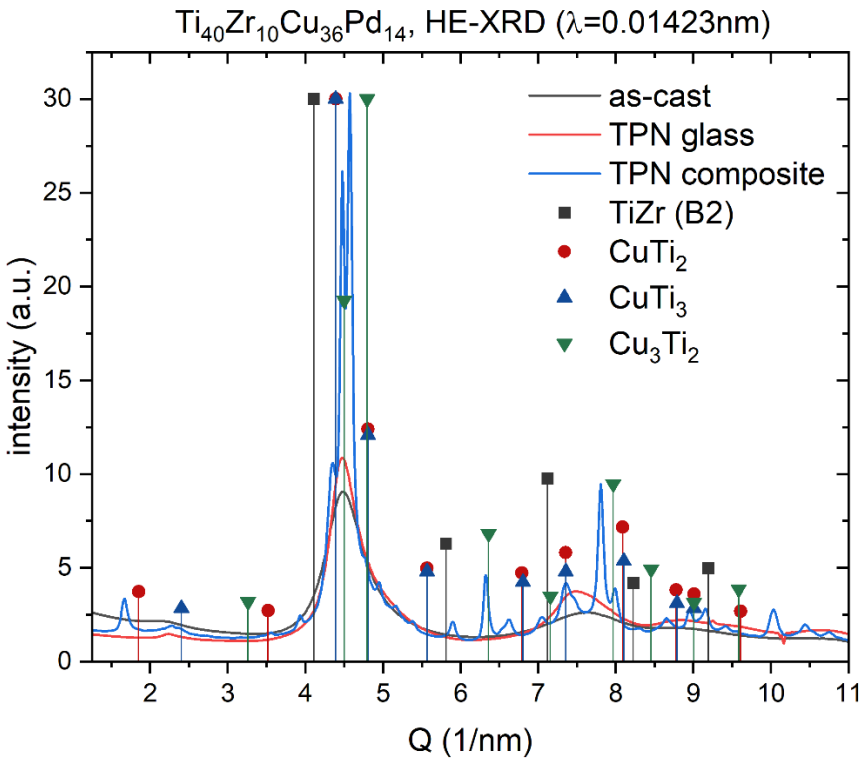

***Fig. 1**. Synchrotron XRD measurements of three selected samples (i.e., as-cast, TPN glass, and TPN composite) in reciprocal space. The diffraction patterns of TPN composite delineate the evolution of B2-TiZr, $CuTi_2$, $CuTi_3$, and Cu_3Ti_2.*

The surface of the TPNed $Ti_{40}Zr_{10}Cu_{36}Pd_{14}$ BMG was further studied by STEM-EDX to demonstrate the distinction between the surfaces and the interior regions, as the surface is what cells come in contact to and thus is important for cytocompatibility. The elemental distributions of the both regions shown in Fig. 2 indicate a clear change in the elemental compositions between the interior of the alloys and their surface. This change was quantified via EDX line scans. The analyzed region is indicated by a horizontal dashed line in the electron image in Fig 2. The transition between the bulk material towards the oxidized surface is accompanied by Pd enrichment, followed by an enrichment of O, Zr, Ti, and Cu towards the sample surface and thus a depletion of Pd. The surface layer of ~100 nm possibly consists of Ti, Cu, and Zr oxides. Underneath, a Pd-enriched interface is observed, towards which the oxidation kinetics is controlled by

oxygen diffusion in the scale. This interfacial Pd layer acts as a barrier to further oxygen diffusion. The elemental maps and line scans of the composite alloy detect more or less the same oxide formation as on the glassy alloy (Supplementary data). It should be noted that the TEM-EDX line scans lead to an overestimation of the at.% of Cu because the lamellae were mounted onto a Cu grid. The trend, however, is still noticeable across the oxidized surface.

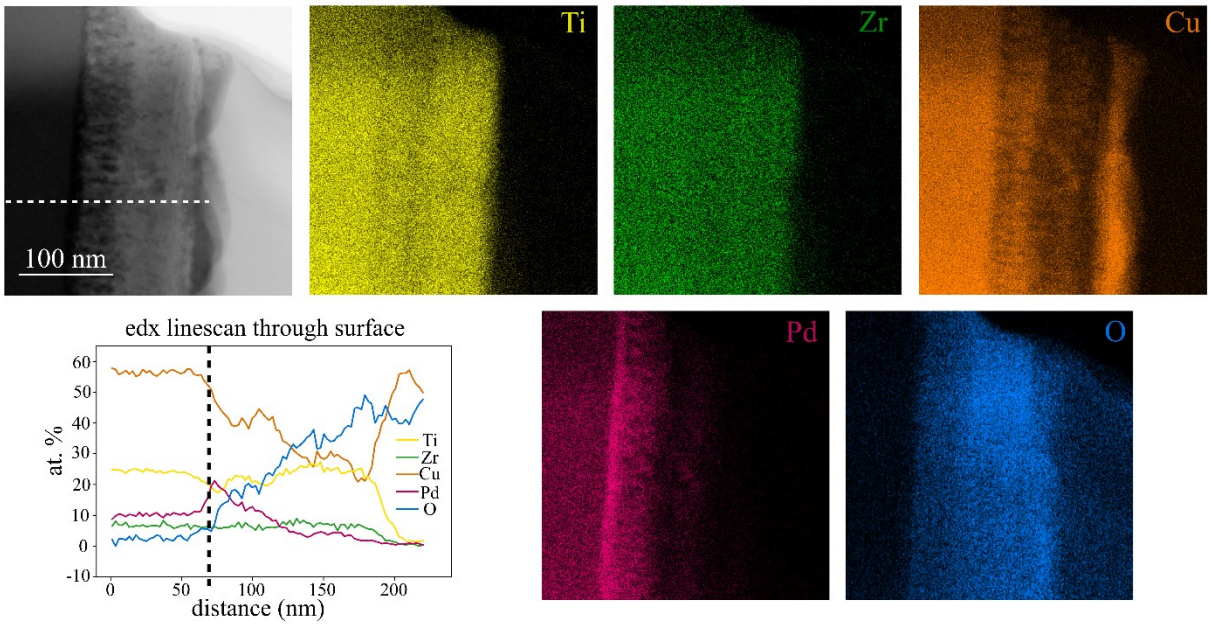

Fig. 2. *Cross-sectional TEM-EDX analyses showing a variation of the elemental compositions between the interior (left part) and the oxidized surface of the as-cast* $Ti_{40}Zr_{10}Cu_{36}Pd_{14}$ *glass, including elemental maps of Ti, Zr, Cu, Pd, and O; together with line-scans across the transition between the interior and surface region (extracted from the white dashed line in the electron image).*

3.2 Thermomechanical properties

The structural relaxation kinetics and crystallization behavior of $Ti_{40}Zr_{10}Cu_{36}Pd_{14}$ as the key events upon shaping were evaluated by a sensitive frequency-dependent DMA technique in 3-point bending (TPB) mode at room and elevated temperatures, which allows to gain more insight into the impact of thermoplastic net-shaping under the given conditions [25]. In comparison to tension- and torsion-type measurements, TPB is more sensitive to structural changes around the glass transition temperature T_g and thus advantageous to visualize the effects

[26]. As a hypothesis, the oscillation of the individual mobile species via TPB transforms into a more cooperative oscillation of a large group of mobile species by a percolation process with the same phase [27]. This can incorporate an ordering of atoms, leading to elastic stiffening of the BMGs. Unlike the TPB mode, tension- and torsion-induced free volume in the structure during DMA is hardly conducive to relaxation of the system. In this case, each atom practically oscillates around its own position with its own phase. That would lead to a structural rearrangement in the medium- and short-range order because the distance between the atoms is larger than the range of the damped oscillation. And thus, a cooperative oscillatory relaxation with the same phase is hence barely possible in the system. Fig. 3a illustrates the storage modulus (G'), the loss modulus (G''), and the loss factor ($tan\ \delta$) of the glassy $Ti_{40}Zr_{10}Cu_{36}Pd_{14}$. At temperatures below the glass transition, the considered BMG deforms primarily elastic, and the mechanical response is independent of the testing frequency, whereas higher temperatures and lower frequencies around the supercooled liquid region (SCLR) derive atomic mobility. This is manifested by the glass transition events taking place at higher temperatures when the frequency increases from 0.1 to 1 to 10 Hz. In contrast, the frequency does not seem to have that much effect on the onset temperature of crystallization (T_x) as it varies from 0.1 to 10 Hz. The glass transition temperature (T_g) of the traces is marked by a sudden change in the slope of G', which yields values of 649, 662, and 668 K ± 1 for the given frequencies. G' of 0.1 Hz drops drastically beyond T_g to its absolute minimum value of 47 ± 1 GPa at the onset of crystallization (T_{x1} = 692 ± 1 K). In G', the onsets of the increase after the first and second sharp drops correspond to T_{x1} and T_{x2}, respectively, at 692 and 775 K ± 1. In G'' and $tan\ \delta$, the two maxima are associated with a two-stage glass crystallization. Stiffening owing to β-relaxation is observed at 1 and 10 Hz prior to the glass transition. The hump in the evolution of G'' depicted in the inset of Fig. 3a indicates relaxation in the γ region. A driving frequency of 0.1 Hz, compared to 1 and 10 Hz, is conducive to a clear

visualization of the crystallization events. After full crystallization, the G' of 1 and 10 Hz exceed their values of the initial states. The variations in the frequency-dependent T_g values are quantified in an Arrhenius plot, revealing an activation energy of $E_a = 8.6 \pm 1.9$ eV (830 ± 183 kJ/mol) attributed to α-relaxation [27-29] (Fig. 3b). This high value is indicative of collective motion of a large number of atoms in this BMG [30-32]. These observations corroborate an accessible SCLR in which the material can be shaped to oral implants [33, 34].

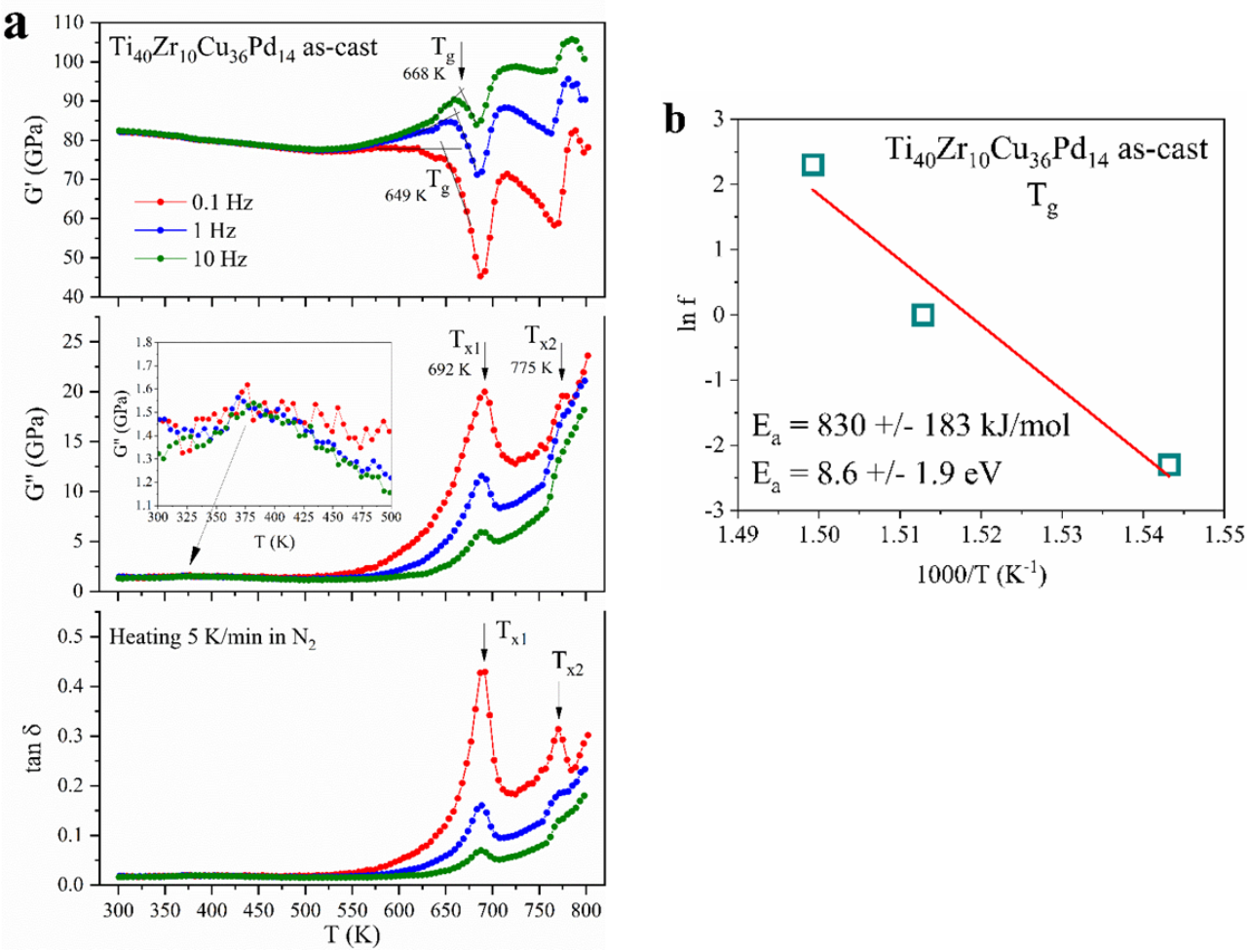

Fig. 3. *(a) Storage modulus (G'), loss modulus (G''), and loss factor (tan δ) of the cast $Ti_{40}Zr_{10}Cu_{36}Pd_{14}$ glass as a function of temperature. The measurement frequencies were 0.1 to 1 to 10 Hz, and the heating rate was 10 K/min. The T_g measurements at different frequencies result in a linear Arrhenius behavior with a slope of 8.6 ± 1.9 eV obtained from the slope of the linear fit (b).*

Fig. 4 displays the evolution of G', G'', and *tan* δ of the deformed $Ti_{40}Zr_{10}Cu_{36}Pd_{14}$ specimens in the glassy and composite states. In G'' of 0.1 Hz, the peak maxima can be addressed to T_{x1} and T_{x2}, for which values of 723 ± 1 and 777 ± 1 K for the TPN glass are registered. T_{x1} of the TPN composite yields an ascending value of 727 ± 1 K, and T_{x2} of the TPN composite has the same value as T_{x1}. The frequencies of 1 and 10 Hz show an evident alleviation of the crystallization events (G'' and *tan* δ of Figs. 4a and b). Fig. 4c illustrates the G', G'', and *tan* δ measurements of the as-cast, TPN glass, and TPN composite samples at 0.1 Hz. G' of the as-cast material displays a plateau up to T_g (649 ± 1 K); then the intact elastic structure breaks up, by which G' drops to its minimum of 47 ± 1 GPa at T_{x1} (692 ± 1 K) and rises to 71 ± 1 GPa at 716 ± 1 K, followed by a second drop to 58 ± 1 GPa at T_{x2} (775 ± 1 K). G' increases afterwards to 82 ± 1 GPa at 789 ± 1 K and decreases to 77 ± 1 GPa at 798 ± 1 K. The characteristic events in the evolution of G'' and *tan* δ of the TPN glass and the TPN composite are mitigated compared to those of the as-cast alloy. The onset of the sudden increase in the slope of G'' and *tan* δ in the course of heating can be linked to T_g, which is shifted towards higher temperatures in the TPN glass and the TPN composite. This confirms a higher thermomechanical stability of the processed glasses at elevated temperatures. Fig. 4d illustrates the corresponding dilatometer traces. The dilatation curve of the as-cast material is basically linear at lower temperatures until the onset of structural relaxation at 493 ± 1 K, where thermal expansion starts to counteract with contraction, which saturates around 550 ± 1 K [17]. The ordinate signal remains more or less constant during the transition into the supercooled liquid state and thereafter until the first crystallization is reached, which is indicated by a step-like drop in the signal within 706 – 724 ± 1 K. Afterwards, the glass continues to expand obeying nearly the same thermal expansion coefficient as below 493 K [17]. A further penetration step occurs at 792 ± 1 K as the glass crystallizes in the second stage until 812 ± 1 K. The two-stage crystallization pathway traversed in the as-cast glass is smoothened after

TPN, which is also confirmed by DMA by the disappearance of the T_{x1} peak. Hence, G' of the TPN samples is stabilized up to 723 ± 1 K, whereas G'' of the as-cast drops at 623 ± 1 K.

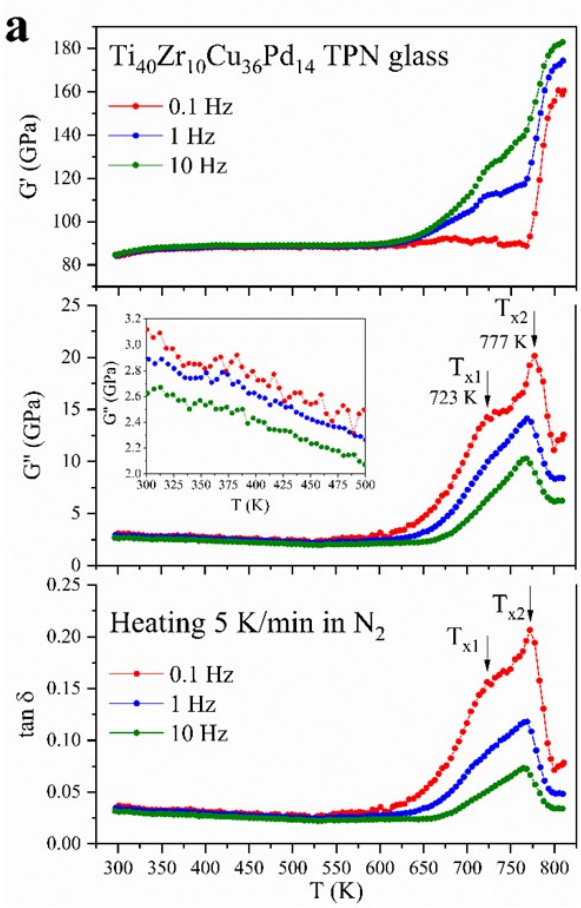
a
Ti40Zr10Cu36Pd14 TPN glass
0.1 Hz
1 Hz
10 Hz
G' (GPa)
G'' (GPa)
Tx2
777 K
Tx1
723 K
T (K)
Heating 5 K/min in N2
tan δ

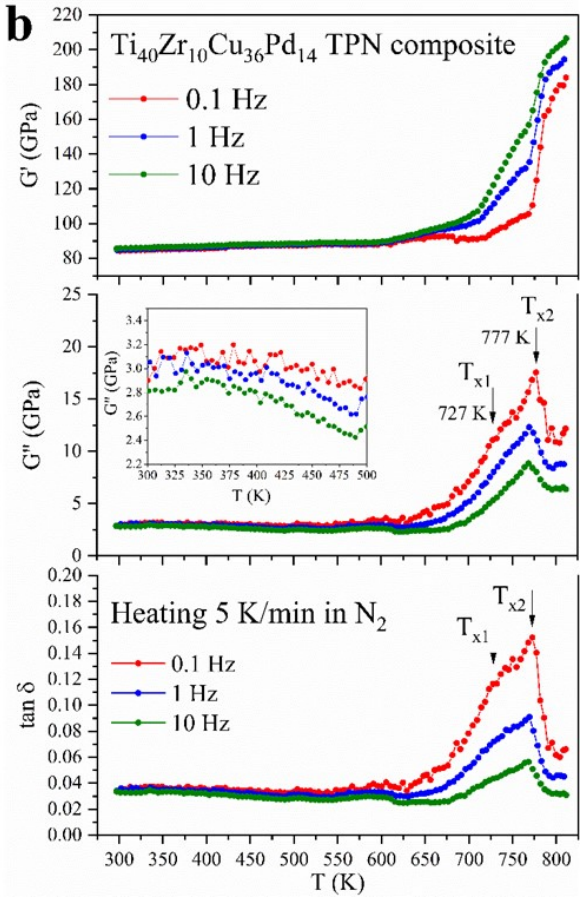
b
Ti40Zr10Cu36Pd14 TPN composite
0.1 Hz
1 Hz
10 Hz
G' (GPa)
G'' (GPa)
Tx2
777 K
Tx1
727 K
T (K)
Heating 5 K/min in N2
tan δ

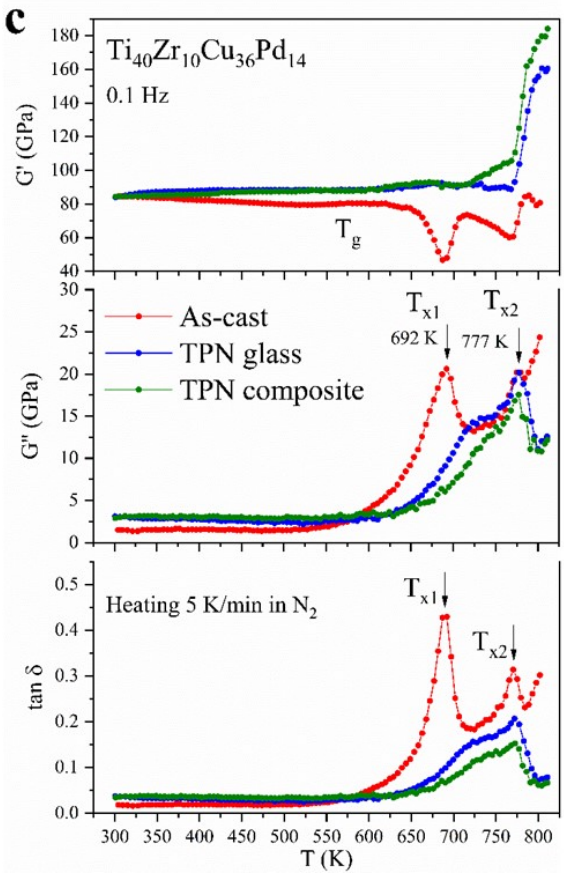
c
Ti40Zr10Cu36Pd14
0.1 Hz
G' (GPa)
Tg
As-cast
TPN glass
TPN composite
Tx1
692 K
Tx2
777 K
G'' (GPa)
Heating 5 K/min in N2
tan δ
T (K)

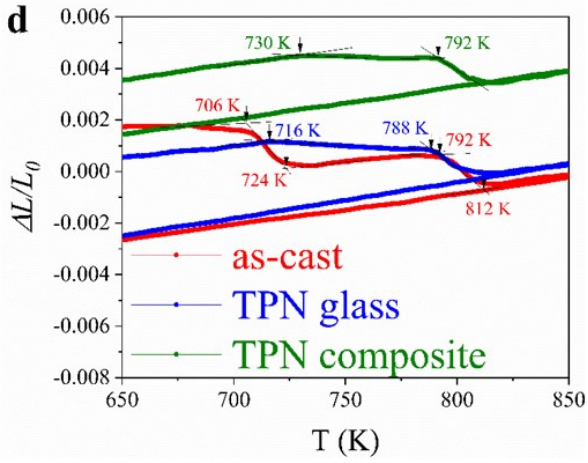
d
730 K
792 K
706 K
716 K
788 K
792 K
724 K
812 K
ΔL/L0
as-cast
TPN glass
TPN composite
T (K)

Fig. 4. *Evolution of the storage modulus (G'), the loss modulus (G"), and the loss factor (tan δ) with temperature during continuous heating (10 K/min) from 300 K to 850 K at a fixed frequency of 1 Hz of (a) TPN glass, (b) TPN composite, and (c) the comparison. The corresponding dilatometer traces are depicted in (d).*

3.3 Corrosion activity

The linear sweep polarization graphs in Fig. 5a indicate clear differences between different states of the material, as well as the oxide formation upon TPN. The as-cast state of the $Ti_{40}Zr_{10}Cu_{36}Pd_{14}$ BMG has a corrosion potential, E_{corr}, of –62 ± 4 mV with a corresponding corrosion current density, J_{corr}, of 15.1 ± 0.7 μA cm^{-2}. For long-waiting times, the sample crystallizes under TPN conditions, which leads to a shift of E_{corr} towards more negative potentials (i.e., –411 ± 2 mV), where J_{corr} also increases (24.4 ± 1.0 μA cm^{-2}).

After TPN, provided that the amorphous state is retained, E_{corr} gets closer to zero (–12 ± 2 mV mV) with a huge drop in J_{corr} = 0.03 ± 0.002 μA cm^{-2}. The shift of the corrosion potential towards more positive values favors the formation of a protective surface, leading to a slow-down in corrosion rate [35]. The drop in the corrosion current density by two orders of magnitude confirms a very high stability of this state in 0.9 wt.% saline environment. Similarly, the passivation current density, J_{pass}, of the TPN glass samples is only 0.14 ± 0.007 μA cm^{-2}, i.e., much lower than that of the as-cast state (~1250 ± 60 μA cm^{-2}). Compared to the TPN glass, the TPN samples with an oxide layer formed upon TPN show much more negative E_{corr} values (–563 ± 2 and –430 ± 5 mV for the amorphous and composite specimens, respectively), with similar J_{corr} values (43 ± 3 and 46 ± 3 μA cm^{-2}, respectively) which is 2 orders of magnitude larger. This finding also indicates that corrosion happens much faster in oxide-layer-containing samples.

The frequency-dependent Bode magnitude plots of the samples in Fig. 5b show an agreement with the results obtained from LSV. The TPN glass displays the largest $|Z|$ (~6437 ± 193 kΩ cm^2) which can be accounted for the lowest J_{corr}.

This value is only ~2 ± 0.06 kΩ cm^2 for the as-cast state, i.e., about 3200 times lower. The composite structure in the other three sample types leads to a small Bode magnitude with a clear hump observed at low to medium-range frequencies. Due to the enhanced corrosion properties of the as-cast glass with respect to the TPN composite counterparts, the following contact angle and cytocompatibility analysis was performed using the TPN glass and its oxide layer.

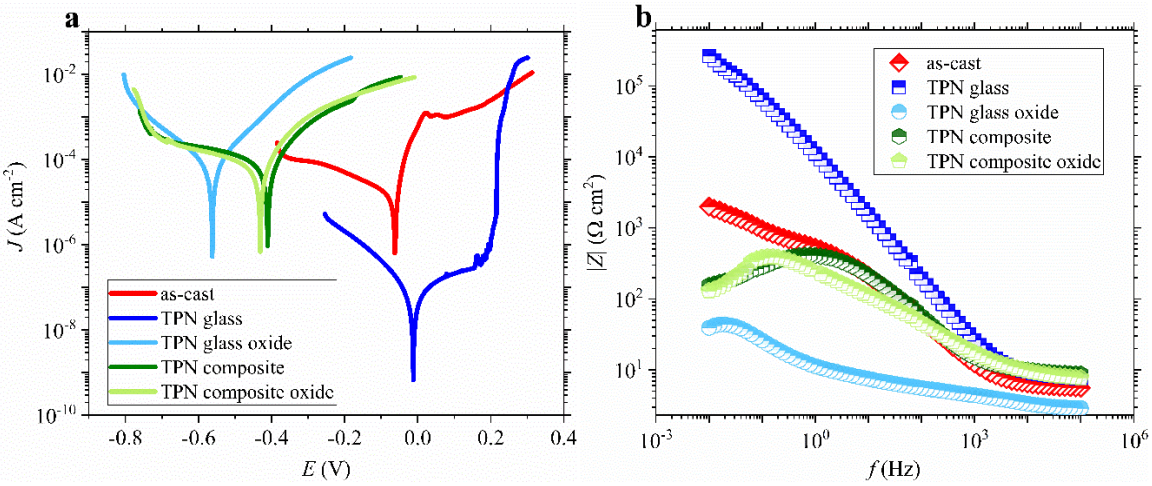

Fig. 5. *(a) Potentiodynamic polarization graphs of different state samples with and without oxide layers. Note that the standard deviation of E_{corr} is within ±1 mV, whereas for J_{corr}, the deviation is within 0.025% of the measured data. The reference potential has a redox potential of +0.195 V vs. a reference hydrogen electrode. (b) Bode magnitude plots of the corresponding sample at their open circuit potential.*

3.4 Contact angle measurements

The results from the static water contact angle measurements conducted on the etched surface of the as-cast and TPN $Ti_{40}Zr_{10}Cu_{36}Pd_{14}$ BMGs are shown in Table 1. The TPN $Ti_{40}Zr_{10}Cu_{36}Pd_{14}$ BMG is investigated both on the oxidized and polished sides. The water contact angle values of the specimens are close to each other; however, a slight decrease of the oxidized surface can be observed. The close values observed for the surfaces can be linked to the similar hydrophobic character of the surface oxides, c.f. Cu oxide for the as-cast vs. mixture of Ti, Cu and Zr oxides for the TPN oxide. After polishing (TPN glass), the surface hydrophobicity increases, which could be due to the Ti-rich, Zr- and Pd-

containing oxide layer with Ti:Zr:Pd ratio of 6.2:1.8:1 in at.% attained from X-ray photoelectron spectroscopy analysis (unpublished data). The increase in surface hydrophobicity can be also correlated with the decrease in corrosion rates and increase in surface resistivity as confirmed in section 2.3.

Table 1. Water contact angle data of the as-cast and TPN $Ti_{40}Zr_{10}Cu_{36}Pd_{14}$ BMG.

	Mean / °	**SD / °**
as-cast	96.8	2.1
TPN glass	100.2	1.8
TPN glass oxide	94.9	2.4

3.4 Cytocompatibility Study

The effect of the formed oxide layer on surfaces of $Ti_{40}Zr_{10}Cu_{36}Pd_{14}$ TPN glass specimens on HGF cells was evaluated by comparing their cytocompatibility properties with TPN glass without oxide layer and as-cast $Ti_{40}Zr_{10}Cu_{36}Pd_{14}$ BMG (control sample). This evaluation was preliminarily performed *in vitro* on HGF cells selected as a representative of the soft tissue in contact with implants that replaced the dental cavity as it represents a physical hurdle for bacteria invasion [36]. Accordingly, HGF cells were directly seeded on the samples' surfaces, and after 24 and 48 hours, the viability and the morphology of adhered and spread cells were determined by fluorescent Live/Dead assay and SEM imaging, respectively (Fig. 6b). The metabolic activity of the cells was evaluated using the colorimetric resazurin assay (Alamar blue); the results are reported in Fig. 6a, indicating that the metabolism of cells was comparable between TPN with an oxide layer and TPN without an oxide layer and as-cast samples at both 24/48 hours' time-points. A statistically significant difference was observed for the TPN samples with an oxide layer after 48 hours in comparison to the TPN specimens without an oxide layer and the control samples ($p < 0.05$ indicated by *, Fig. 6a). As a confirmation of the cells' metabolic activity results, the images obtained from the Live/Dead assay and SEM demonstrate that the cells were able to successfully adhere and spread onto the $Ti_{40}Zr_{10}Cu_{36}Pd_{14}$-TPN with oxide layer

surfaces; however, on the surfaces of TPN specimens without oxide layer and as-cast samples some cells are in round shapes and the confluence of these roundish cells onto the TPN samples without oxide layer is more pronounced than for the ones on the control specimens. The surface wettability of the as-cast $Ti_{40}Zr_{10}Cu_{36}Pd_{14}$ BMG has been investigated previously by Rezvan et al. [17] as a favorable surface for its antifouling properties. One would expect that the same surface with hydrophobic characteristics is not favorable for direct attachment of cells on the surface. Of course, this does not mean that the surface is cytotoxic, since the green color of those cells in the fluorescent Live/Dead assay demonstrates that the cells were alive. The same behavior with no significant differences is observed for the TPNed non-oxide layer. This means that the thermoplastic net-shaping, an important process in shaping metallic glasses into their final form to be utilized as implants, does not adversely affect the cytocompatibility (Fig. 6b). EDX-TEM investigations of the oxide layer of the TPNed samples, on the other hand, show an enrichment of Ti, Zr, Cu and the presence of oxygen towards the surface, meaning that a mix of Ti, Cu, and Zr oxides is present. Indeed, the presence of titanium oxide could significantly enhance the surface wettability, thereby favoring cells attachment, as previously demonstrated by Wang et al. [37]. This could justify the better performance of the oxide layer in easing cell attachment.

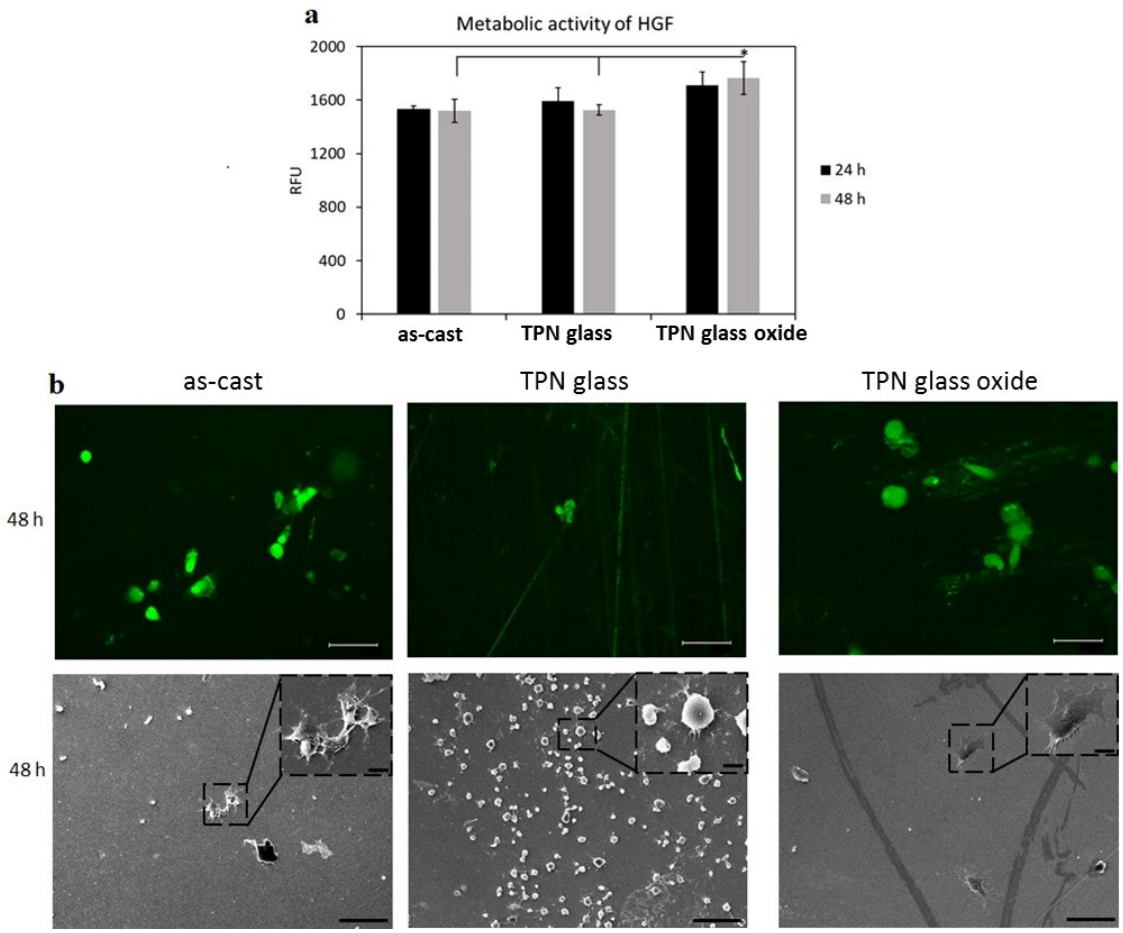

Fig. 6. *Cytocompatibility evaluation of $Ti_{40}Zr_{10}Cu_{36}Pd_{14}$ TPN glass specimens with and without oxide layer towards HGF that were seeded directly onto their surfaces. $Ti_{40}Zr_{10}Cu_{36}Pd_{14}$ BMG (as-cast) was considered as control sample. The cytocompatibility activity after 24 and 48 hours was evaluated by: a) metabolic activity after 24 and 48 hours; b)* ***upper panel****: Fluorescent Live/Dead images of the surface attached cells after 48 hours; scale bars are 100 µm;* ***bottom panel****: SEM images of the surface attached cells after 48 hours at two different magnifications ×200 (scale bar 100 µm) and ×500 (scale bar 50 µm). * indicates p value< 0.05.*

4. Conclusions

The prospects of $Ti_{40}Zr_{10}Cu_{36}Pd_{14}$ BMG as oral implant material are advanced in the aspects of processing, structure-dependent mechanical performance, corrosion, hydrophobicity, and bioactivity. In this study we have investigated the effect of thermoplastic net-shaping, the process required to reach the final desired shape of the implants, on the BMG's microstructure, corrosion behavior and cytocompatibility. It is confirmed by dynamic mechanical analysis that optimized

thermoplastic processing leads to BMGs and BMG composites showing a more stabilized G' up to ~700 K, revealing an increase in the thermomechanical stability by above 100 K in comparison to the as-cast glass. In 0.9 wt.% NaCl solution, corrosion is strongly inhibited in the TPNed glass determined from ~4 orders of magnitude lower J_{corr} values as well as two orders of magnitude larger $|Z|$ at low-frequencies compared to the as-cast material. A cytocompatibility analysis was conducted by seeding human gingival fibroblast cells (HGF) directly onto the oxide-layer-containing and oxide layer-free $Ti_{40}Zr_{10}Cu_{36}Pd_{14}$ BMG after thermoplastic net-shaping, using the as-cast $Ti_{40}Zr_{10}Cu_{36}Pd_{14}$ BMG as control. The results demonstrate that thermoplastic net-shaping does not adversely affect the cytocompatibility. On the other hand, the formation of ~100 nm thin surface layers consisting of Ti, Cu, and Zr oxides improves cells attachment. The attributing factor for this improvement is related to the presence of titanium oxide on the surface that significantly improves the surface wettability.

Acknowledgments

B.S. acknowledges the Austrian Science Fund (FWF) under project grant I3937-N36. E.S. would like to thank European Commission for providing funding for this project under the Horizon 2020 research and innovation program for Marie Skłodowska-Curie Individual Fellowship, with the acronym “MAGIC” and grant agreement N. 892050. A.L. acknowledges financial support by the Austrian Science Fund (FWF) under the project grant T891-N36, Y1236-N37. Additional support was provided through the ERC Proof of Concept Grant TriboMetGlass (grant ERC-2019-PoC-862485). We acknowledge DESY (Hamburg, Germany), a member of the Helmholtz Association HGF, for the provision of experimental facilities. Parts of this research were carried out at PETRA III and we would like to thank Dr. Nobert Schell and Dr. Emad Maawad for assistance in using beamline P07B, operated by Helmholtz Zentrum Hereon. Authors thank Siavash Amirosanloo and Katja Hrbinič for their assistance in the water contact angle measurements.

CRediT authorship contribution statement

AR contributed to methodology, investigation, formal analysis, validation and writing original draft, ES methodology, validation and writing original draft, VS investigation and review & editing, WS resources and review & editing, JT investigation and review & editing, AL investigation, review & editing and funding acquisition, CG resources and review & editing, NAS review & editing, AA investigation, IO review & editing, SS investigation and review & editing, JK resources and funding acquisition, ZN methodology, investigation, and review & editing, AC review & editing, ACS review & editing, LR supervision and review & editing, BS conceptualization, methodology, validation, writing original draft, supervision and funding acquisition, JE contributed tosupervision, review & editing, resources, and funding acquisition.

Supplementary

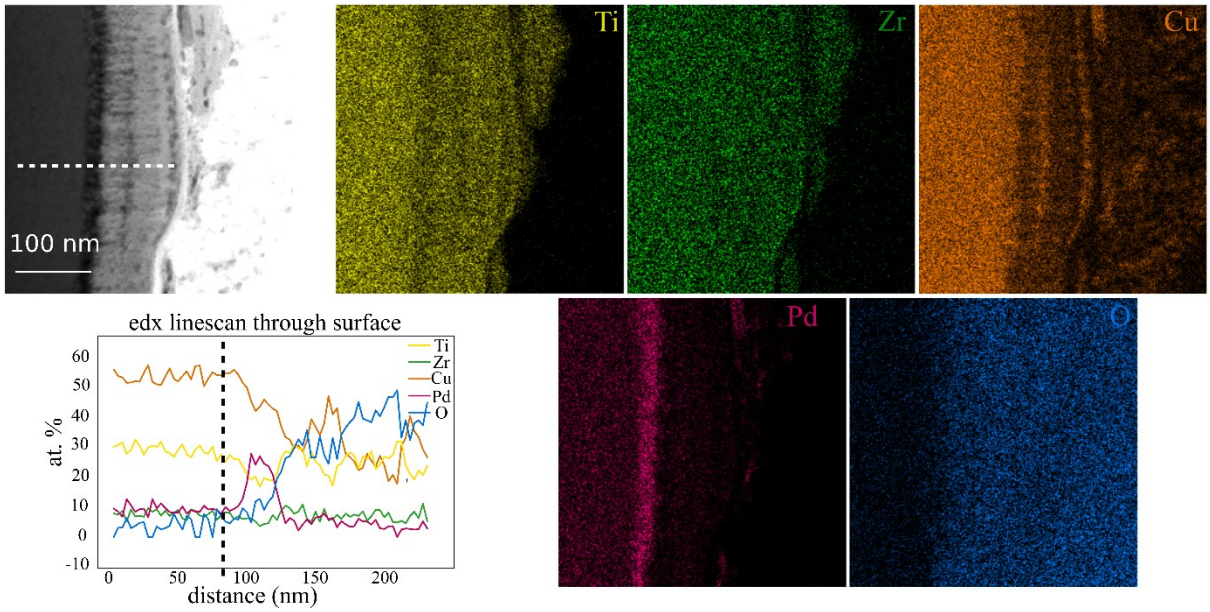

Fig. S1. *Cross-sectional TEM-EDX analyses taken from the composite alloy showing a variation of the elemental composition between the interior (left part) and the oxidized surface of the TPNed* $Ti_{40}Zr_{10}Cu_{36}Pd_{14}$ *composite, including elemental maps of Ti, Zr, Cu, Pd, and O with a line scan for each element.*

References

[1] J. Schroers, T.M. Hodges, G. Kumar, H. Raman, A.J. Barnes, P. Quoc, T.A. Waniuk, Thermoplastic blow molding of metals, Mater. Today 14 (2011) 14–19,

[2] B. Sarac, J. Eckert, Thermoplasticity of metallic glasses: Processing and applications, Prog. Mater. Sci. 127 (2022) 100941, https://doi.org/10.1016/j.pmatsci.2022.100941.

[3] J. Schroers, The superplastic forming of bulk metallic glasses, Jom-Us 57 (2005) 35–39, https://doi.org/10.1007/s11837-005-0093-2.

[4] B. Sarac, G. Kumar, T. Hodges, S.Y. Ding, A. Desai, J. Schroers, Three-dimensional shell fabrication using blow molding of bulk metallic glass, J Microelectromech S 20 (2011) 28–36, https://doi.org/10.1109/JMEMS.2010.2090495.

[5] B. Sarac, S. Bera, S. Balakin, M. Stoica, M. Calin, J. Eckert, Hierarchical surface patterning of Ni- and Be-free Ti- and Zr-based bulk metallic glasses by thermoplastic net-shaping, Mater. Sci. Eng., C 73 (2017) 398–405, https://doi.org/10.1016/j.msec.2016.12.059.

[6] J. Schroers, Processing of bulk metallic glass, Adv. Mater. 22 (2010) 1566–1597, https://doi.org/10.1002/adma.200902776.

[7] M. Hasan, J. Schroers, G. Kumar, Functionalization of metallic glasses through hierarchical patterning, Nano Lett. 15 (2015) 963–968, https://doi.org/10.1021/nl504694s.

[8] B. Sarac, S. Bera, F. Spieckermann, S. Balakin, M. Stoica, M. Calin, J. Eckert, Micropatterning kinetics of different glass-forming systems investigated by thermoplastic net-shaping, Scr. Mater. 137 (2017) 127–131, https://doi.org/10.1016/j.scriptamat.2017.02.038.

[9] G. Kumar, A. Desai, J. Schroers, Bulk metallic glass: The smaller the better, Adv. Mater. 23 (2011) 461–476, https://doi.org/10.1002/adma.201002148.

[10] G.S. Leventhal, Titanium, a metal for surgery, J. Bone Joint Surg. Am. 33-A (1951) 473-474,

[11] H.F. Li, Y.F. Zheng, Recent advances in bulk metallic glasses for biomedical applications, Acta Biomater. 36 (2016) 1–20,

[12] C.Y. Xie, I. Milosev, F.U. Renner, A. Kokalj, P. Bruna, D. Crespo, Corrosion resistance of crystalline and amorphous CuZr alloys in NaCl aqueous environment and effect of corrosion inhibitors, J Alloy Compd 879 (2021) 160464, https://doi.org/10.1016/j.jallcom.2021.160464.

[13] M.M. Vasić, T. Žák, N. Pizúrová, I.S. Simatović, D.M. Minić, Influence of Thermal Treatment on Microstructure and Corrosion Behavior of Amorphous $Fe_{40}Ni_{40}B_{12}Si_8$ Alloy, Metall. Mater. Trans, A 52 (2021) 34–45, https://doi.org/10.1007/s11661-020-06079-3.

[14] E. Yüce, L. Zarazúa-Villalobos, B. Ter-Ovanessian, E. Sharifikolouei, Z. Najmi, F. Spieckermann, J. Eckert, B. Sarac, New-generation biocompatible Ti-based metallic glass ribbons for flexible implants, Mater. Des. 223 (2022) 111139, https://doi.org/10.1016/j.matdes.2022.111139.

[15] M. Katsikogianni, Y.F. Missirlis, Concise review of mechanisms of bacterial adhesion to biomaterials and of techniques used in estimating bacteria-material interactions, Eur. Cell Mater. 8 (2004) 37–57, https://doi.org/10.22203/ecm.v008a05.

[16] E. Sharifikolouei, Z. Najmi, A. Cochis, A.C. Scalia, M. Aliabadi, S. Perero, L. Rimondini, Generation of cytocompatible superhydrophobic Zr–Cu–Ag metallic glass coatings with antifouling properties for medical textiles, Mater. Today Bio 12 (2021) 100148, https://doi.org/10.1016/j.mtbio.2021.100148.

[17] A. Rezvan, E. Sharifikolouei, A. Lassnig, V. Soprunyuk, C. Gammer, F. Spieckermann, W. Schranz, Z. Najmi, A. Cochis, A.C. Scalia, L. Rimondini, M.

Manfredi, J. Eckert, B. Sarac, Antibacterial activity, cytocompatibility, and thermomechanical stability of $Ti_{40}Zr_{10}Cu_{36}Pd_{14}$ bulk metallic glass, Mater. Today Bio 16 (2022) 100378, https://doi.org/10.1016/j.mtbio.2022.100378.

[18] S.L. Zhu, X.M. Wang, F.X. Qin, M. Yoshimura, A. Inoue, New TiZrCuPd Quaternary Bulk Glassy Alloys with Potential of Biomedical Applications, Mater Trans 48 (2007) 2445–2448, https://doi.org/10.2320/matertrans.MRA2007086.

[19] F.X. Qin, M. Yoshimura, X.M. Wang, S.L. Zhu, A. Kawashima, K. Asami, A. Inoue, Corrosion Behavior of a Ti-based bulk metallic glass and its crystalline alloys, Mater Trans 48 (2007) 1855–1858, https://doi.org/10.2320/matertrans.MJ200713.

[20] G. Lütjering, Property optimization through microstructural control in titanium and aluminum alloys, Mater. Sci. Eng., A 263 (1999) 117-126, https://doi.org/10.1016/S0921-5093(98)01169-1.

[21] P. Gong, L. Deng, J. Jin, S. Wang, X. Wang, K. Yao, Review on the Research and Development of Ti-Based Bulk Metallic Glasses, Metals-Basel 6 (2016) 264, https://doi.org/10.3390/met6110264.

[22] G. Ashiotis, A. Deschildre, Z. Nawaz, J.P. Wright, D. Karkoulis, F.E. Picca, J. Kieffer, The fast azimuthal integration Python library: pyFAI, J. Appl. Crystallogr. 48 (2015) 510-519, https://doi.org/10.1107/S1600576715004306.

[23] J.C. Qiao, Q. Wang, J.M. Pelletier, H. Kato, R. Casalini, D. Crespo, E. Pineda, Y. Yao, Y. Yang, Structural heterogeneities and mechanical behavior of amorphous alloys, Prog. Mater. Sci. 104 (2019) 250–329, https://doi.org/10.1016/j.pmatsci.2019.04.005.

[24] L. Gautier, S. Cazottes, M. Veron, D. Fabregue, J. Chevalier, Spherulitic growth process in Ti-based metallic glass: Microstructure, phase identification,

and growth mechanism, Mater. Charact. 192 (2022) 112170, https://doi.org/10.1016/j.matchar.2022.112170.

[25] A. Rezvan, B. Sarac, V. Soprunyuk, J.T. Kim, K.K. Song, C.J. Li, W. Schranz, J. Eckert, Influence of combinatorial annealing and plastic deformation treatments on the intrinsic properties of $Cu_{46}Zr_{46}Al_8$ bulk metallic glass, Intermetallics 127 (2020) 106986, https://doi.org/10.1016/j.intermet.2020.106986.

[26] A. Rezvan, B. Sarac, V. Soprunyuk, F. Spieckermann, C. Gammer, H. Sheng, N.A. Sifferlinger, J. Eckert, Deformation-Mode-Sensitive Behavior of CuZr-Based Bulk Metallic Glasses Under Dynamic Loading, Metall. Mater. Trans. A 52 (2021) 8–13, https://doi.org/10.1007/s11661-020-06048-w.

[27] J.M. Pelletier, J. Perez, L. Duffrene, Mechanical response of an oxide glass to mechanical loading—shear and volume relaxation effects: physical analysis, Acta Mater 48 (2000) 1397–1408, https://doi.org/10.1016/S1359-6454(99)00387-0.

[28] J.C. Qiao, J.M. Pelletier, Dynamic Mechanical Relaxation in Bulk Metallic Glasses: A Review, J Mater Sci Technol 30 (2014) 523-545, https://doi.org/10.1016/j.jmst.2014.04.018.

[29] Q. Wang, J.M. Pelletier, J.J. Blandin, Thermal stability of cerium-based bulk metallic glasses. Influence of iron addition, J Alloy Compd 504 (2010) 357–361,

[30] K. Schröter, G. Wilde, R. Willnecker, M. Weiss, K. Samwer, E. Donth, Shear modulus and compliance in the range of the dynamic glass transition for metallic glasses, Eur. Phys. J. B 5 (1998) 1–5, https://doi.org/10.1007/s100510050411.

[31] S. Etienne, J.Y. Cavaillé, J. Perez, R. Point, M. Salvia, Automatic System for Analysis of Micromechanical Properties Rev. Sci. Instrum. 53 (1982) 1261–1266, https://doi.org/10.1063/1.1137153.

[32] S. Puech, J.J. Blandin, J.L. Soubeyroux, Mg based bulk metallic glasses with high mechanical strength and large viscoplastic forming capacity, Adv Eng Mater 9 (2007) 764–768, https://doi.org/10.1002/adem.200700160.

[33] S. Maeda, T. Yamasaki, Y. Yokoyama, D. Okai, T. Fukami, H.M. Kimura, A. Inoue, Viscosity measurements of $Zr_{55}Cu_{30}Al_{10}Ni_5$ and $Zr_{50}Cu_{40-x}Al10Pd_x$ (x=0, 3 and 7 at.%) supercooled liquid alloys by using a penetration viscometer, Mater. Sci. Eng., A 449 (2007) 203–206, https://doi.org/10.1016/j.msea.2006.02.288.

[34] A. Inoue, Stabilization of metallic supercooled liquid and bulk amorphous alloys, Acta Mater 48 (2000) 279–306, https://doi.org/10.1016/S1359-6454(99)00300-6.

[35] F. Ropital, 15 - Environmental degradation in hydrocarbon fuel processing plant: issues and mitigation, in: M.R. Khan (Ed.), Advances in Clean Hydrocarbon Fuel Processing, Woodhead Publishing, Sawston, United Kingdom, 2011, pp. 437–462.

[36] A. Cochis, S. Ferraris, R. Sorrentino, B. Azzimonti, C. Novara, F. Geobaldo, F. Truffa Giachet, C. Vineis, A. Varesano, A. Sayed Abdelgeliel, S. Spriano, L. Rimondini, Silver-doped keratin nanofibers preserve a titanium surface from biofilm contamination and favor soft-tissue healing, J. Mater. Chem. B 5 (2017) 8366–8377, https://doi.org/10.1039/C7TB01965C.

[37] G. Wang, J. Li, K. Lv, W. Zhang, X. Ding, G. Yang, X. Liu, X. Jiang, Surface thermal oxidation on titanium implants to enhance osteogenic activity and in vivo osseointegration, Sci. Rep. 6 (2016) 31769, https://doi.org/10.1038/srep31769.

Overview of co-authored publications

F. Spieckermann, D. Şopu, V. Soprunyuk, M.B. Kerber, J. Bednarčík, A. Schökel, **A. Rezvan**, S. Ketov, B. Sarac, E. Schafler, J. Eckert

Structure-dynamics relationships in cryogenically deformed bulk metallic glass

Nature Communications, DOI: 10.1038/s41467-021-27661-2 **(2022)**

Remzi Gürbüz, Baran Sarac, Viktor Soprunyuk, **Amir Rezvan**, Eray Yüce, Wilfried Schranz, Jürgen Eckert, Ali Ozcan, A. Sezai Sarac

Carbon nanotube-polybutadiene-poly(ethylene oxide)-based composite fibers: Role of cryogenic treatment on intrinsic properties

Polymers for Advanced Technologies, DOI: 10.1002/pat.5828 **(2022)**

Keziban Huner, Baran Sarac, Eray Yüce, **Amir Rezvan**, Matej Micusik, Maria Omastova, Jürgen Eckert and A. Sezai Sarac

Iron Oxide – Poly(m-anthranilic acid)-Poly (ε-caprolactone) Electrospun Composite Nanofibers: Fabrication and Properties

Molecular Systems Design & Engineering, DOI: 10.1039/d2me00181k **(2023)**

Baran Sarac, Remzi Gurbuz, Matej Micusik, Mária Omastová, **Amir Rezvan**, Eray Yüce, Lixia Xi, Jürgen Eckert, Ali Ozcan, A. Sezai Sarac

Styrene-butadiene-styrene-based stretchable electrospun nanofibers by carbon nanotube inclusion

Molecular Systems Design & Engineering, DOI: 10.1039/D3ME00035D **(2023)**